MULTISCALE MODELING OF THE DEFORMATION OF SEMI-CRYSTALLINE POLYMERS

A Dissertation
Presented to
The Academic Faculty

by

James Ellison Shepherd

In Partial Fulfillment
of the Requirements for the Degree
Doctor of Philosophy in the
School of Mechanical Engineering

Georgia Institute of Technology

May 2006

MULTISCALE MODELING OF THE DEFORMATION OF SEMI-CRYSTALLINE POLYMERS

Approved by:

Dr. David L. McDowell, Co-Advisor
GWW School of Mechanical Engineering
Georgia Institute of Technology

Dr. Karl I. Jacob, Co-Advisor
School of Polymer, Textile, and Fiber Engineering
Georgia Institute of Technology

Dr. Min Zhou
GWW School of Mechanical Engineering
Georgia Institute of Technology

Dr. Jianmin Qu
GWW School of Mechanical Engineering
Georgia Institute of Technology

Dr. Rina Tannenbaum
School of Materials Science and Engineering
Georgia Institute of Technology

Date Approved: March 17, 2006

To my wife, Melinda, and my children, Leah and Scott.

ACKNOWLEDGEMENTS

I would like to thank my family, particularly my wife Melinda, for all of the sacrifices they made while I worked on this research. I would like to thank my advisors, Dr. David McDowell and Dr. Karl Jacob, for providing me the opportunity to pursue this research full-time. I appreciate the advice and direction they gave in regards to both my research and future career endeavors. I would like to thank the members of my reading committee, Dr. Min Zhou, Dr. Jianmin Qu, and Dr. Rina Tannenbaum, for their comments and suggestions. I would like to thank all of the graduate students in the mechanics of materials group who provided help and friendship during my time at Georgia Tech.

This research was aided financially by the ARCS Scholarship, the GAAN Award in Polymer Science and Engineering, the Nano-Science and Technology Fellowship, and by the ERC program of the National Science Foundation.

TABLE OF CONTENTS

LIST OF TABLES

LIST OF FIGURES

LIST OF SYMBOLS

A	energy barrier to inelastic flow
$\mathbf{B}$	left Cauchy Green tensor
b	crystal unit cell width
b_c	parameter that affect the shape of the potential blending curve
b_n	parameter that affect the shape of the potential blending curve
b_γ	parameter that affect the shape of the potential blending curve
$\mathbf{C}$	fourth rank elasticity tensor
C	normalizing constant
$C_a(\theta,\phi)$	amorphous chain orientation distribution (COD)
C_{inf}	characteristic length parameter
c	specific heat of the polymer
$\mathbf{D}_i^p$	inelastic rate of deformation in the current configuration
$\tilde{\mathbf{D}}_i^p$	inelastic rate of deformation in the intermediate configuration
d_i	distance between lattice site i and the destination
d_{ij}	distance between lattice sites i and j
d_{max}	distance between furthest neighbor and the destination
E_a	activation energy of a transition
E_i	total energy on a lattice site i
$\mathbf{F}$	continuum deformation gradient
$\mathbf{F}_n$	deformation gradient representing network resistances
$\mathbf{F}_i$	deformation gradient representing intermolecular resistances
$\mathbf{F}_i^e$	elastic component of the deformation gradient representing intermolecular resistances

$\mathbf{F}_i^p$	inelastic component of the deformation gradient representing intermolecular resistances
ΔF_e	thermal activation energy for entanglement slippage
$\Delta F_g^*(\theta,\phi)$	critical free energy of stable growth on the surface of an established rectangular parallelepiped-shaped crystallite
$\Delta F_n^*(\theta,\phi)$	free energy required to form a critically sized nucleus
ΔF_t	shear stress activation energy for entanglement slippage
f	weighting factor for lattice site selection probabilities
$f(\Delta V)$	blending function to ensure continuity
$\Delta f(\theta,\phi)$	bulk free energy in the deformed state
Δf_0	undeformed, randomly oriented bulk free energy
f_{boost}	corrective boost factor
$G(\theta,\phi)$	number of polymer segments required to form a stable nucleus of critical size
ΔH^*	heat of activation of the jump process at the nucleus interface
ΔH_f	heat of fusion of the polymer
Δh	equilibrium enthalpy of crystallisation
J	Jacobian determinant
$K(\mathbf{p})$	kinetic energy of atoms with momentum **p**
K_0	pre-exponential crystallisation growth rate factor
$k_{A\rightarrow}^{HTST}$	harmonic transition state theory constant
k_1, k_2, k_3, k_4	dihedral potential constants
k_a	angle potential constant
k_b	bond potential constant
k_B	Boltzmann's constant

$\mathbf{L}_i^p$	inelastic velocity gradient representing intermolecular resistances
$\mathcal{L}^{-1}$	inverse of the Langevin function
l	length of a Kuhn segment
m_i	components of the unit direction vector
m_j	mass of atom j
$\mathbf{N}$	normalized deviatoric stress due to intermolecular resistance
N	number of segments in an effective chain
N_a	number density of statistical segments in the amorphous phase
N_c	number density of statistical segments in the crystalline phase
$N_{cv}(\theta,\phi)$	total virtual number density of segments in the crystalline phase
N_d	number of dihedral groups in the system
$N_{gv}(\theta,\phi)$	virtual number density of segments that attach to previously formed nuclei
$N_{nv}(\theta,\phi)$	virtual number density of polymer segments forming nuclei
N_s	number of lattice sites
N_{tot}	total number of segments per unit volume, i.e. $N_{tot} = N_a+N_c$
n	number density of chains
$n_{c_{tot}}$	total number density of crystal nuclei
$n_c(\theta,\phi)$	number density of crystal nuclei
$n_{cv}(\theta,\phi)$	virtual number density of crystal nuclei
$\dot{n}_{c0}$	nucleation number density rate factor in the undeformed state
n_e	total number density of entanglements
$n_{e_{base}}$	number density of rate-independent entanglements
$n_{e_{init}}$	number density of the initial amount of entanglements in the undeformed material

$n_{e_{slip}}$	number density of rate-dependent entanglements
$\dot{n}_{e0}$	entanglement slippage pre-exponential constant
$\dot{n}_g(\theta,\phi)$	rate of segments being added to a crystallite during growth
n_x	number of cross-links in the simulation cell
P_2	Herman's orientation
P_{damp}	pressure dampening factor
$\mathbf{p}$	momentum of all of the atoms in the system
p	hydrostatic stress
p_i	probability of selecting neighbor *i*
$p_{chain}\left(\lambda(\theta',\phi'),N\right)$	probability that a chain with *N* segments has a stretch of $\lambda(\theta',\phi')$
$p_{seg}(\theta,\phi,\theta',\phi')$	probability of a segment having an orientation of (θ,ϕ) in a chain with an end-to-end orientation of (θ',ϕ')
q	stress related power law parameter
$\mathbf{R}_i^e$	rigid rotation of the deformation gradient representing intermolecular resistances
$\mathbf{r}$	positional degrees of freedom for all of the atoms
r	distance between two atoms or chain end-to-end length
r_b	bond length
r_o	equilibrium bond length
r_{SC}	equilibrium distance between two atoms for the soft core potential
S	scaling parameter representing the sensitivity of entanglement density to overall stretch
$S_a(\theta,\phi)$	amorphous segment orientation distribution (SOD)
$S_c(\theta,\phi)$	crystalline segment orientation distribution (SOD)
s	athermal shear stress

T	absolute temperature
T_{damp}	temperature dampening parameter
T_{high}	high temperature of the simulation
T_{low}	desired low temperature
T_m	melting temperature
t_{high}	high temperature simulation time
t_{low}	equivalent low temperature time
Δt_{MD}	molecular dynamics integration time step
$\mathbf{V}_i^e$	left Cauchy Green tensor of the elastic deformation gradient
V	scalar representation of the overall stretch
$\Delta V(\mathbf{r})$	difference between the potential and floor energies
V_a	bond angle potential energy
V_b	bond length potential energy
$\Delta V_b(\mathbf{r})$	boost potential
V_{cell}	volume of the simulation cell
V_d	dihedral angle potential energy
$V_d(\phi_d)$	normal dihedral potential energy at a dihedral angle of ϕ_d
V_{floor}	floor energy
V_{lj}	Lennard-Jones potential energy
$V_{max}(\mathbf{r})$	largest potential energy of all of the atoms in the system
V_{SC}	soft core potential energy
$V_{sc_{max}}$	soft core potential parameter
$v_{crystal}$	average volume of a crystallite
$\mathbf{W}_i^p$	inelastic spin tensor in the current configuration

$\tilde{\mathbf{W}}_i^p$	inelastic spin tensor in the intermediate configuration
X_{max}	maximum allowable level of crystallinity
$\beta(\theta,\phi,\theta',\phi')$	cosine of the angle between a segment having an orientation of (θ,ϕ) and a chain with an end-to-end orientation of (θ',ϕ')
$\dot{\gamma}^p$	inelastic shearing rate
$\dot{\gamma}_0^p$	inelastic shearing rate pre-exponential factor
ε_{lj}	Lennard-Jones potential parameter
$\Theta(\Delta V)$	stepping function which is 1 if ΔV is greater than zero and 0 otherwise
θ	polar coordinate of the global spherical coordinate system
θ_a	bond angle
θ_0	equilibrium bond angle
$\lambda(\theta,\phi)$	stretch of the continuum
λ_e	equivalent stretch
λ_i	principal components of the stretch tensor
ρ_i	effective density at the lattice site i
$\boldsymbol{\sigma}$	total Cauchy stress
$\boldsymbol{\sigma}'$	deviatoric total Cauchy stress tensor
$\boldsymbol{\sigma}_i$	Cauchy stress due to intermolecular resistance
$\boldsymbol{\sigma}_i'$	deviatoric stress due to intermolecular resistance
$\boldsymbol{\sigma}_n$	Cauchy stress due to network resistance
$\hat{\sigma}_i$	principal components of the stress due to the network resistance
σ_e	end surface free energy of a crystal
σ_{lj}	equilibrium atom separation

σ_s	side surface free energy of a crystal
v_0	ratio of the normal mode frequencies at the minimum energy points to the normal mode frequencies at the transition points
τ	equivalent shear stress
ϕ	azimuthal coordinate of the global spherical coordinate system
ϕ_d	dihedral angle
ω	volume rescaling frequency

LIST OF ABBREVIATIONS

COD	chain orientation distribution
FEM	finite element method
ISV	internal state variable
kMC	kinetic Monte Carlo
MC	Monte Carlo
MD	molecular dynamics
NPT	constant number, pressure, temperature ensemble
NVT	constant number, volume, temperature ensemble
PYS	Paul, Yoon, and Smith potential
RIS	rotational isomeric state
SIC	strain-induced crystallization
SOD	segment orientation distribution
TAD	temperature accelerated dynamics
TST	transition state theory

SUMMARY

The mechanical and physical properties of polymers are determined primarily by the underlying nano-scale structures and characteristics such as entanglements, crystallites, and molecular orientation. These structures evolve in complex manners during the processing of polymers into useful articles. Limitations of available and foreseeable computational capabilities prevent the direct determination of macroscopic properties directly from atomistic computations. As a result, computational tools and methods to bridge the length and time scale gaps between atomistic and continuum models are required. In this research, an internal state variable continuum model has been developed whose internal state variables (ISVs) and evolution equations are related to the nano-scale structures. Specifically, the ISVs represent entanglement number density, crystal number density, percent crystallinity, and crystalline and amorphous orientation distributions. Atomistic models and methods have been developed to investigate these structures, particularly the evolution of entanglements during thermo-mechanical deformations. A new method has been created to generate atomistic initial conformations of the polymer systems to be studied. The use of the hyperdynamics method to accelerate molecular dynamics simulations was found to not be able to investigate processes orders of magnitude slower that are typically measurable with traditional molecular dynamics simulations of polymer systems. Molecular dynamics simulations were performed on these polymer systems to determine the evolution of entanglements during uniaxial deformation at various strain rates, temperatures, and molecular weights. Two methods were evaluated. In the first method, the forces

between bonded atoms along the backbone are used to qualitatively determine entanglement density. The second method utilizes rubber elasticity theory to quantitatively determine entanglement evolution. The results of the second method are used to gain a clearer understanding of the mechanisms involved to enhance the physical basis of the evolution equations in the continuum model and to derive the model's material parameters. The end result is a continuum model that incorporates the atomistic structure and behavior of the polymer and accurately represents experimental evidence of mechanical behavior and the evolution of crystallinity and orientation.

CHAPTER 1

INTRODUCTION

Motivation

Use of polymers has been steadily increasing in the past two decades. Semi-crystalline polymers are converted to useful articles through thermo-forming processes in which polymers are subjected to large deformations. Temperature, strain rate, and total strain are some of the processing parameters that can be varied to affect the properties of the manufactured article. Some common processing techniques are blow molding for beverage containers, drawing of film and fibers, and vacuum forming of various parts. In addition to providing the appropriate shape for the final article, an objective in these shaping operations is to engineer the microscopic and nanoscale molecular characteristics in order to provide the necessary mechanical and physical properties of the material. The molecular characteristics of interest in most processes include crystallinity, orientation, and molecular entanglements. As the polymer is deformed, its macromolecules become elongated and more oriented in the directions of the deformation. This elongation and orientation can have a significant effect on the evolution rates of molecular entanglements and crystal structures. Typically, an increase in the amount of crystallization, entanglements, or orientation will result in a mechanically stronger material with greater resistance to small molecule diffusion. While increased crystallinity can improve mechanical and barrier properties, the size of the crystal structures can also affect the optical clarity of the material which may be a significant design parameter.

The evolution of these nanoscale molecular structures depends on complex dependencies on the processing characteristics and interactions between the structures. Unfortunately, these complex dependencies and interactions make optimization of the manufacturing process difficult and typically necessitate expensive and time-consuming experimental trials. For these reasons, it is desirable to create analytical and numerical models to simulate these processes and to predict the effects of process modifications on material morphology and behavior.

To understand the relationship between nanoscale structures and mechanical properties, the complex set of interactions governing polymer molecules must be elucidated. The integration of atomistic, monomeric, and configurational attributes of polymer molecules must be included in the development of models. An accurate model can have benefits beyond just predicting the mechanical response of the material. It can provide useful information regarding morphological evolution during the manufacturing process, and it can help identify the required polymer nanostructures to achieve specific properties. The latter, which contributes to design of the material itself, is potentially a useful tool in the development of new materials, reducing the amount of time-consuming physical testing of materials with various microstructures. The modeling of morphology evolution is also relevant to determining other material properties such as permeability, optical clarity, and environmental stability.

The evolution and interactions of the nanoscale morphology need to be related to the macroscopic mechanical responses. Due to the difficulty of experimentally observing the development of this morphology, computational modeling is a more feasible method currently available to better understand the transient evolution of these structures during

deformation. Using valid constitutive frameworks, models of the morphology evolution and interactions must be integrated together. Ideally, each morphological entity would be modeled utilizing atomistic methods, the results of which could then be implemented into a mesoscopic constitutive model.

A constitutive model that incorporates the evolution of the major morphological components of semi-crystalline polymers has been previously developed (Shepherd 2002). These morphological components include molecular chain orientation, size and number of crystallites, and molecular entanglements. The complex inter-dependencies of the morphology evolution and process history dependence are also considered. The model is based on an internal state variable (ISV) constitutive framework that employs statistical mechanics and encompasses the molecular level and nanoscale effects such as crystallization, relaxation, and orientation and includes strain, strain-rate, and temperature dependencies. In its completed form, the model can be effectively utilized in finite element method (FEM) software to investigate material response during processing. It is highly desirable for this model to be informed by molecular calculations to form a more predictive link. This is a principal motivation for the present dissertation.

Objectives and Goals

The overall goal of this research is to develop molecular modeling methods to support the characterization of the ISV model's parameters and evolution equations entirely from the chemical structure and morphology of the material. Molecular modeling techniques will be used to inform the ISV model by quantifying relationships between polymer morphology and the resulting mechanical behavior as well as to

determine the evolution of the morphology under various processing conditions. These derived relationships will effectively bridge the gap between molecular and continuum level models. Specifically, the following aspects will be investigated:

- the correlation between the statistical mechanics based models of rubber elasticity and the actual behavior of polymer networks in the rubbery, and in some cases, glassy state, including improved models for instantiating the initial geometric configuration of molecules in the polymer;
- the progression of molecular entanglements as a function of orientation, temperature, and time; and
- the enhancement of the ISV model to incorporate the results from the atomistic modeling investigation of rubber elasticity behavior and entanglement evolution.

The proposed tasks involve detailed investigations and model development to determine the behavior of various molecular organizations and nanostructured assemblies of molecules.

Benefits of this Research

The principal benefit of this research will be the development of methods and tools that can be used to extrapolate the properties of a polymer molecule to the bulk behavior of an assembly of these polymer molecules at the macroscopic scale. By utilizing molecular models, which are based on first principles, the methods and models should be applicable to a large range of polymer types. This research could then be used

not only to optimize the manufacturing processes for currently used polymers, but could also be used to develop new polymers and additives to meet particular needs.

Primary Challenges

The primary challenge regarding the use of molecular modeling tools to study polymer systems is the computational cost of simulating polymer systems at the desired length and time scales. Another significant challenge of this research is to create atomistic models that separate and characterize the evolution of key components such as entanglements, crystallites, and connectivity so that appropriate evolution relations can be established. The difficulty arises due to the inter-dependent nature of these components. The modeling methods proposed should reasonably account for the effects each of these components.

Methods

While there has been much discussion about bridging the atomistic and mesoscale models for polymer systems in general (Uhlherr and Theodorou 1998; Goddard III et al. 2001; Glotzer and Paul 2002; Theodorou 2004), none of these proposed methods have been applied to link atomistic simulations of structure development to continuum models. The actual applications of these ideas have only come in the form of specific relaxation modes in melts or of a solitary behavior in solids such as yield softening (Argon et al. 1995) and separately, cross-link development (Rottach et al. 2004). The combined use of molecular models and continuum models to capture the effect of nanoscale structure

development on the macroscopic behavior of polymers is not known to have been attempted. The methods proposed in this thesis serve as a framework to meet this goal.

On a macroscopic scale at large strains, semi-crystalline polymers typically exhibit a hardening response to deformation represented by increasing rates of work hardening at increasing strains. This hardening is primarily due to the reduction of configurational entropy associated with the straightening of chains resulting from elongation. For a given polymer, the magnitude of this hardening is affected by molecular entanglement evolution and crystallization, both of which are rate and temperature dependent processes.

Entanglements are physical interactions between molecules and, in some cases, within molecules that constrain inter-molecular motions. Entanglement slippage allows the chains to return to a higher level of entropy by reducing these physical constraints on the polymer chains, thereby reducing the hardening effect of the material. Because entanglement slippage is a nonequilibrium process of thermally-activated character, lower strain rates and higher temperatures increase the amount of entanglement slippage and therefore reduce the hardening effect. This reduction of the hardening rate is confirmed by the experimental work performed by Raha and Bowden (1978), who found that the number of "cohesion points" or entanglements decreases exponentially with strain at a fixed strain rate and temperature. In this research, molecular dynamics methods are developed to identify and track the evolution of entanglements. The results and 'lessons learned' from simulations using these methods will be used to develop evolution equations for the continuum model.

Strain-induced crystallization (SIC) reduces the entropy of the polymer chains by adding more constraints, thereby increasing the magnitude of hardening. The rate at which a semi-crystalline polymer is deformed has two competing effects on the rate of crystallization. Decreasing the strain rate allows more time for the polymer chains to relax towards a less oriented state, thereby reducing the degree of SIC. But decreasing the strain rate also allows more time for the chain segments to engage in an increased number of molecular interactions, on average, that are favorable to increasing the crystallization rate. Salem (Salem 1992b) demonstrated from experimental work that the relaxation effect is dominant, and the onset of SIC is delayed at lower strain rates. Higher strain rates reduce the degree of chain relaxation at a given strain level, resulting in more preferred orientation and increased likelihood for crystal nuclei to form (Le Bourvellec et al. 1986; Salem 1992b; Clauss and Salem 1995; Salem 1998), even at lower strains. Crystal growth depends on the temperature and the degree of noncrystalline polymer chain orientation in relation to the crystallite orientation. The exothermic nature of the crystallization process increases the temperature and possibly causes localized softening, followed by necking, in the material during stretching (Ziabicki 1988).

Rubber elasticity models have been used successfully to simulate the configurational entropy of bulk polymer systems which is the driving mechanism behind the resistance of polymer molecules to deformation. In this research, the relationship between rubber elasticity models and molecular dynamics simulations of actual polymers are investigated. The results of these simulations are used to verify the applicability of rubber elasticity models for use in the continuum model and give insight to the

relationship between the parameters of the rubber elasticity model and the properties of the polymer.

While the overall goal of this research is to develop methods that will be applicable to a wide range of polymers over all reasonable time and temperature ranges, the actual development will be performed on a more practical scope. Linear polyethylene is the material used in this research due to its simple structure and substantial experimental and computational characterization. The temperature range of this investigation will be limited from 25°C to 100°C, which corresponds to the rubbery state of polyethylene in which ample experimental and computational data exist. Despite these limitations in scope, the methods should be general enough to be valid for most polymer systems in the rubbery state and many polymer systems in the glassy state. Validation of this claim will be reserved for future research.

The ISV model (Shepherd 2002) has been enhanced to more correctly account for the effect of nanoscale structures on the thermo-mechanical behavior during deformation (Shepherd et al. 2006). In the previous model (Shepherd 2002), crystallization and molecular entanglement slippage were based on the orientation and degree of crystallinity of the entire assembly of molecules. The model was modified to account for the orientation distribution and degree of crystallinity of all of the monomers in the system in order to incorporate the local molecular architecture. Additionally, the entanglement, crystal nucleation, and crystal growth evolution equations were modified and the exothermic nature of crystallization was included. The resulting model is theoretically more faithful to various physical mechanisms and more accurately simulates experimental results. This model, bridging nanoscale attributes and macroscopic level

properties, is now ready for the incorporation of additional input from atomistic modeling. The governing equations and material model constants for rubber elasticity, entanglement evolution, and crystallization will be modified, if necessary, according to the results of the atomistic modeling. This next step is critical in order to reach the overall goal of this research.

Dissertation Structure

Chapter 2 provides details of the molecular dynamics methods used in this research, particularly those related to the deformation of the polymer system. Results of parametric studies performed to determine the most plausible MD parameters are provided.

In Chapter 3, a new method of generating polymer configurations is presented and evaluated. This method has the advantages of generating a low energy molecular assembly with specified structural properties. Detailed descriptions of the implementation of this method are included, as well as comparisons of this implementation with another widely used method.

Chapter 4 covers the results from several accelerated molecular dynamics methods explored in this thesis to increase the time scales available to the polymer deformation simulations. The theory and implementation of these methods are described as well as the benefits and limitations of these methods as related to this research.

Chapter 5 presents an investigation of entanglement evolution utilizing atomic modeling tools. A new method is presented to identify entanglements based on the bond forces along the polymer chains. The effects of strain rate, temperature, and molecular

weight are determined. The results of this method are qualitative in nature and seem to be counter-intuitive at high strains.

Chapter 6 presents a study of the relationship between atomistic simulations of actual polymer systems and the more idealistic statistical network models. Molecular dynamics simulations of a cross-linked polymer system are performed. The key network model parameters can be determined by disabling non-bonded potentials which has the effect of removing restrictions to molecular movement. These relationships permit the entanglement evolution of non-cross-linked systems to be quantitatively determined. Additionally, the network model was found to be capable of accurately representing polymer behavior.

Chapter 7 presents an improved version of the ISV-based constitutive model that includes the evolution results from the atomistic simulations performed in this research. The development of the ISV model is detailed and the model is compared to experimental results.

Chapter 8 summarizes the significant accomplishments of this research and proposes further research directions in this research field.

CHAPTER 2

ATOMISTIC MODELING OF POLYMER DEFORMATION

Molecular Dynamics Simulations of Polymers

As there is a substantial amount of literature detailing the history, theory, and implementation of atomistic modeling, e.g. (Leach 2001; Rapaport 2004), the focus of this chapter will be specific to issues related to modeling polymer systems.

The molecular dynamics (MD) software LAMMPS (Plimpton 1995) and the visualization and post-processing software VMD (Humphrey et al. 1996) are used to perform the atomistic simulations and review the results. These codes were selected due to their extensibility, the capabilities required in this research, the open software licenses that permit the modification and sharing of source code, and the ability to work with large sets of atoms.

Time and Length Scale Issues

One of the most significant issues faced when performing atomistic simulations of polymer systems is the immense amount of computational time required to model sufficiently large systems for durations long enough to capture all relevant mechanisms. Polymers used in engineering applications typically consist of tens of thousands to millions of atoms per molecule. Furthermore, since multiple molecules must be included in the system in order to account for intermolecular interactions, the number of atoms in the system is increased many-fold. To capture the atomic dynamics correctly, integration

time steps must be on the order of the period of atomic vibrations (10^{-14}s). Polymer mechanisms necessary for understanding of macroscopic deformation behavior occur over time periods many orders of magnitude larger. The primary mechanism for large deformations on the molecular level is bond rotation about the dihedral angles, which occurs at the time scale of 10^{-11}s. For larger ordered motions, the characteristic time (e.g. Rouse time) for a molecular chain to diffuse from its original location is on the order of 10^{-3}s to 10^{3}s.

The limits of MD simulations are constrained by the multiplicative combination of the number of atoms to be modeled and the amount of time that the simulation is to be run which can be measured in atom-s. With currently available computing, this limit is typically on the order of 10^{-3}atom-s. Therefore, effective means of reducing the degrees of freedom in line with available computational resources or techniques must be developed to simulate larger periods of time with fewer integration time steps. There are several techniques for reducing the degrees of freedom. Multiple neighboring atoms can be represented by a single "united atom". Atom positions can be constrained to points on a lattice to remove the number of positional states for an atom. Periodic boundary conditions can be used to mimic the effect of neighboring atoms and permit polymer molecules whose length exceeds that of the simulation cell. Inter-atomic potentials can be simplified or eliminated if the effect of these potentials is not significant in relation to the desired results. For example, bead-spring potentials which do not include bond angle or dihedral potentials are commonly used when the detailed chemical structure of the polymer is not of interest. Some of these techniques will be utilized in this research.

Additionally, time acceleration methods in molecular dynamics are investigated and discussed in detail in Chapter 4.

General Molecular Dynamics Components

As a result of numerical approximations required in MD simulations, especially the use of cut-off distances in potentials to reduce the computational requirements, the energy in the system can drift over time. Therefore, methods must be implemented to maintain thermodynamic constraints from the effect of cumulative errors. In this research, an isothermal and isobaric (NPT) ensemble is chosen for proper deformation. Constraining the volume (NVT) would not account for any change in density during deformation and could lead to inaccurate pressures on free surfaces of the simulation cell. Nose (Nose 1984) implements an external thermal bath and its associated momentum to permit the energy in the system to fluctuate while maintaining a NVT or NPT ensemble using time and distance scaling. A similar ensemble has been presented by Berendsen (1984). Hoover (1985) modified the Nose ensemble to remove time scaling. Hoover also demonstrated that Berendsen's ensemble is not time reversible and does not lead to the canonical distribution.

The non-equilibrium NPT ensemble proposed by Melchionna et al. (1993) is an extension to the Nose-Hoover ensemble to more precisely sample the NPT ensemble. This ensemble is available natively in LAMMPS and was used throughout this research.

A united atom approximation is utilized in which the methyl groups are represented by a single "atom" or unit. The effect of the hydrogen atoms on the polymer's configuration is accounted for in the potentials, while the mass is included in

the mass of the united atom. This technique has been shown to work well with melts, but the loss of anisotropy and the incorrect center of mass of the united atom may be a liability for the denser solid models being investigated in this research. The potentials of Paul et al. (1995) are chosen due to their accuracy in predicting correct behavior of polyethylene and in particular for ordered structures such as crystals (Lavine et al. 2003). The bond force potential is modified from a rigid link to a stiff spring (Bolton et al. 1999; Capaldi et al. 2004) using the harmonic bond potential in LAMMPS, i.e.,

$$V_b = k_b \left(r_b - r_o \right)^2 \tag{2.1}$$

where k_b = 350 kcal/mol, r_b is the bond length, and r_0 is the equilibrium bond length, 1.53Å. The bond angle potential is also defined as a harmonic potential,

$$V_a = k_a \left(\theta_a - \theta_0 \right)^2 \tag{2.2}$$

where k_a = 60 kcal/mol rad^2, θ_a is the bond angle, and θ_0 is the equilibrium bond angle, 109.5°. The dihedral or bond rotation potential is defined as a multi-harmonic potential,

$$V_d = \sum_{n=1}^{4} k_n \cos^{n-1} \phi_d \tag{2.3}$$

where k_1 = 1.73 kcal/mol, k_2 = -4.49 kcal/mol, k_3 = 0.776 kcal/mol, k_4 = 6.99 kcal/mol, and ϕ_d is the dihedral angle. The non-bonded interactions such as van der Waals forces were implemented by use of a Lennard-Jones potential,

$$V_{lj} = 4\varepsilon_{lj} \left[\left(\frac{\sigma_{lj}}{r_{lj}} \right)^{12} - \left(\frac{\sigma_{lj}}{r_{lj}} \right)^{6} \right] \tag{2.4}$$

where ε_{lj} = 0.112 kcal/mol, σ_{lj} = 4.01Å, and r_{lj} is the distance between the two atoms. The non-bonded interactions are disabled between any atoms that are within four bonds of

each other on the same chain, since those non-bonded interactions are already embedded in the other potentials.

Figure 2.1 shows the potential energies as a function of their relevant degrees of freedom for each of the potentials described above. From the plots, it is apparent that the bond length and bond angle potentials provide the greatest constraints on the system, while the dihedral potential provides the least constraints. As a result, the majority of deformation in a polymer system is a result of dihedral rotations.

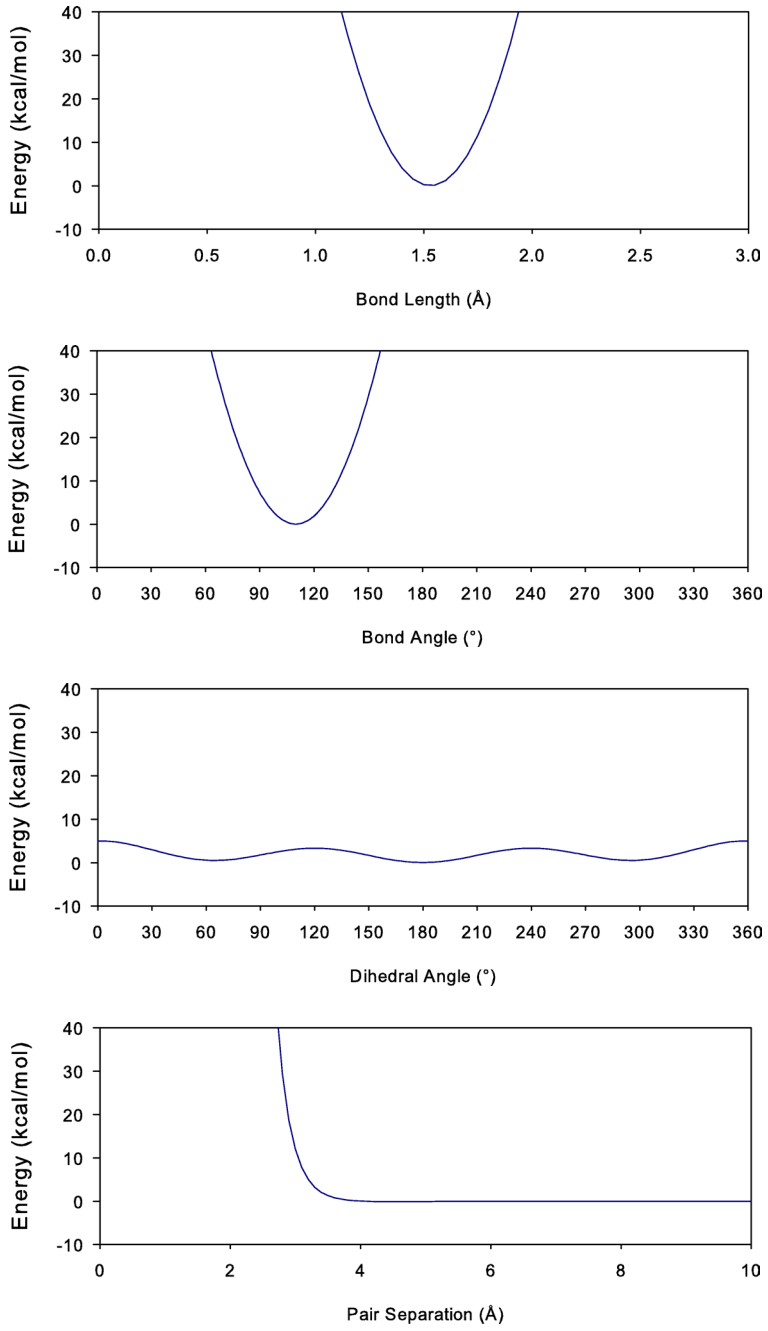

Figure 2.1 Plots of each potential showing the relative strengths of each.

Full periodic boundary conditions are implemented in order to permit the creation of long polymer chains without resorting to unlikely, crowded configurations to avoid

artifacts of simulation. The use of full periodic boundary conditions also reduces edge effects.

Deformation Procedure

Prior to any deformation simulation, the initial configuration is relaxed to ensure that the system is in relative equilibrium. An NPT ensemble is used to maintain a constant temperature, typically 300 K, and to allow the system volume to change so that the relaxed density is achieved at an external pressure of 1 atm. The relaxation is run for 500 ps with an integration time step of 1.0 fs. Post-processing scripts written in Perl were created to extract information regarding the energies and structure of the system during the relaxation process. The potential and kinetic energies as well as the temperature, volume, and pressure are extracted from LAMMP's normal output file. The scripts use the coordinates of each atom which LAMMPS writes out at periodic time steps to determine the evolution of end-to-end lengths, radii of gyration, and rotational isomeric states.

Most of the atomistic studies in this research require the polymer model to be deformed. For uniaxial deformation, this process is achieved by setting the two sets of opposing surfaces perpendicular to the applied deformation direction at a constant, ambient pressure of 1 atm for the duration of the deformation. The remaining set of surfaces is then displaced at a specified true strain rate. This deformation is achieved by combining a volume rescaling routine in the x-direction with an NPT ensemble where the pressures in the y- and z-directions were set to 1 atm and the pressure in the x-direction was not regulated. In LAMMPS each time step begins with the NPT calculations to

determine the pressure derived displacements to the faces normal to the y- and z-directions followed by the prescribed displacements to the faces normal to the x-direction. All of the atoms in the simulation box are moved proportional to their distances from the displaced faces, resulting in affine deformation. By default LAMMPS is only capable of deforming the simulation cell at a constant deformation rate. LAMMPS was modified so that the simulation cell could be deformed at a constant rate of true strain to better pair with the true stress that is recorded, to account for the significant dimensional changes at large deformations, and to mimic typical large deformation experiments. The true strain is measured in the logarithmic form based on the dimensions of the periodic unit cell, i.e.,

$$\varepsilon_x = \ln\left(\frac{x}{x_0}\right) \tag{2.5}$$

where x is the current length of the cell, x_0 is the initial length of the cell prior to the commencement of deformation.

The pressures on the faces of the simulation cell and the strains are monitored during the simulation and used to determine the stress- or strain-dependent relationships. The pressure on each face is given as the normal tensor component of the virial stress,

$$\boldsymbol{\sigma}_v = \frac{1}{V}\left(\sum_{i=1}^{N_{atoms}} m_i \mathbf{v}_i \mathbf{v}_i - \sum_{i=1, j<i}^{N_{atoms}} \mathbf{r}_{ij} \frac{\partial U_{ij}}{\partial \mathbf{r}_{ij}}\right) \tag{2.6}$$

where V is the current volume of the periodic unit cell, m_i is the mass of atom i, $\mathbf{v}_i$ is the velocity, N_{atoms} is the number of atoms in the system, $\mathbf{r}_{ij}$ is the vector between the atoms i and j, and U_{ij} is the potential energy between atoms i and j.

Throughout the remainder of this dissertation, in the context of molecular dynamics results, the term ‘stress’ refers to the virial stress and the term ‘strain’ refers to the true, or logarithmic, strain measure.

Since polymer chains are long and there are substantial differences between intermolecular and intramolecular forces, the size of the simulation cell could have an effect on the continuity of the results. The larger the size of the simulation cell with the appropriate density, the more likely that configuration will represent a continuum. However, larger simulation sizes take much more computational time. One of the initial goals was to find out the smallest size of a system that still maintains the deformation behavior of larger systems in the hope of minimizing computational requirements while reducing size effects. Three equal density assemblies consisting of 20, 50, and 100 linear molecules with 1000 monomers per molecule were created resulting in systems of 20,000, 50,000, and 100,000 atoms respectively. The initial configurations were generated using the methods and parameters described in Chapter 3. These systems were relaxed and then deformed at a true strain rate of 10^{10} s^{-1} and a temperature of 300 K. Figure 2.2 shows that for true strains under 1.5 there are not any substantial differences between the stress-strain behaviors of the different sized systems. At higher strains, there seems to be systematic differences between the stress responses for the differently sized systems, where the larger systems result in higher stresses.

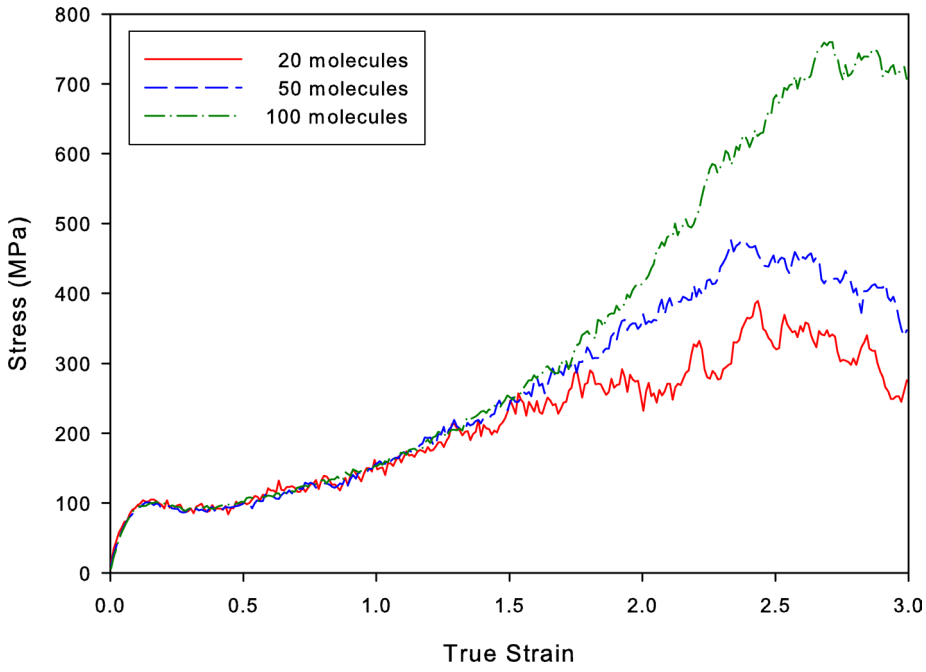

Figure 2.2 Comparisons between the stress-strain behaviors of polymer systems consisting of 20, 50, and 100 molecules each with 1000 unified atoms at a temperature of 300 K and a true strain rate of 10^{10} s^{-1}.

While these results indicate that the 100,000 atom system may be more accurate than the 20,000 atom system at true strains above 1.5 and the 50,000 atom system at true strains above 1.75, a smaller sized system is preferred due to the significantly higher computational expense of the 100,000 atom system. A system size of 50,000 atoms is used throughout the research rather than the smaller 20,000 atom system due to its closer representation of the larger system and the smoother response. Additionally, the 50,000 atom system gives the ability to investigate polymer molecules with higher molecular weights while keeping the system size constant over the 20,000 atom system. The discrepancies in the results for the differently sized systems are an artifact of the polymer systems forming voids at the higher strains (Figure 2.3). Due to the selection of 50,000 atom systems, further simulations are limited to a strain of 1.75.

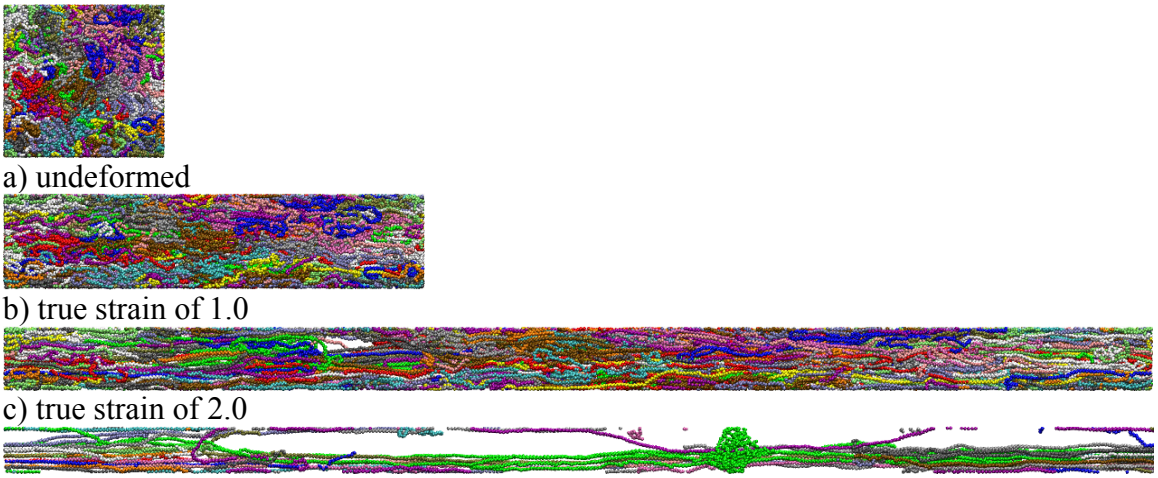

Figure 2.3 Deformation sequence of a polymer system consisting 50 molecules each with 1000 unified atoms at a temperature of 300 K and a true strain rate of 10^{10} s^{-1} showing void formation at a true strain of 2.0 (c) and void growth and chain coiling at a true strain of 3.0 (d).

Another concern is the consistency between simulations with different initial velocity distributions. At the start of a MD simulation, the atoms must be assigned velocities in a manner that ensures the kinetic energy of the system conforms to the desired temperature. In LAMMPS, the initial velocities are assigned randomly to each atom through the use of a Boltzmann distribution. The velocity distributions were modified by changing the random number generator seed. Figure 2.4 shows that the distribution of initial velocities does not have a significant effect on the deformation behavior at strains below 1.75. Therefore a single initial velocity profile should be sufficient for each of the simulations performed in this research.

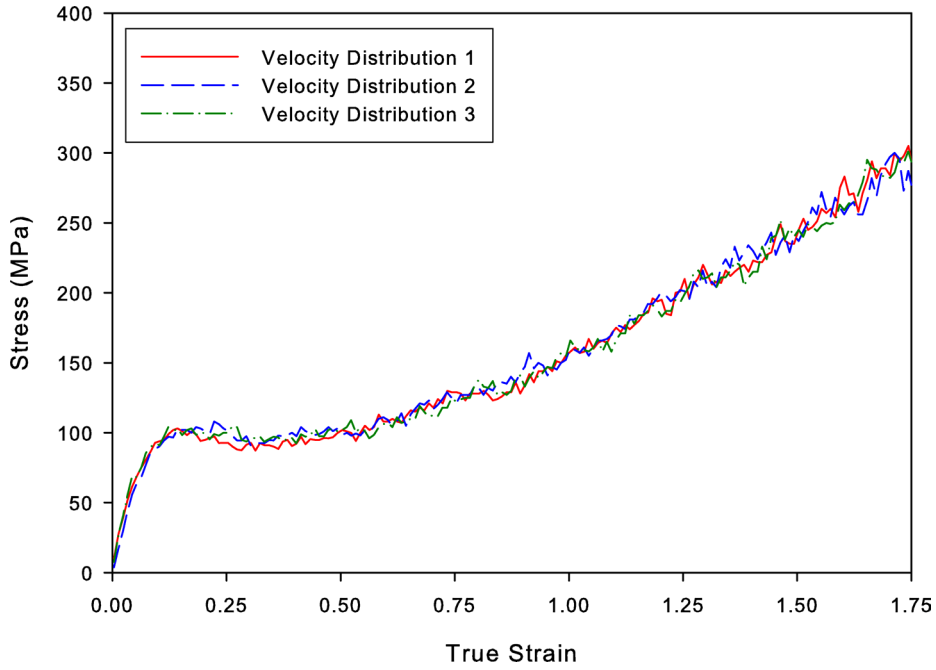

Figure 2.4 Comparisons between the stress-strain behaviors of polymer systems consisting of 50 molecules each with 1000 unified atoms with different initial velocity distributions at a temperature of 300 K and a true strain rate of 10^{10} s^{-1}.

A further concern is the consistency between simulations with different initial configurations having similar structures. Three initial configurations consisting of 50 molecules with 1000 unified atoms each were generated using the method described in Chapter 3. Figure 2.5 shows that initial configurations generated with the same parameters but different random number seeds do not have a significant effect on the consistency of the deformation behavior at true strains less than 1.75. Therefore a single initial configuration should be sufficient for the simulations performed in this research.

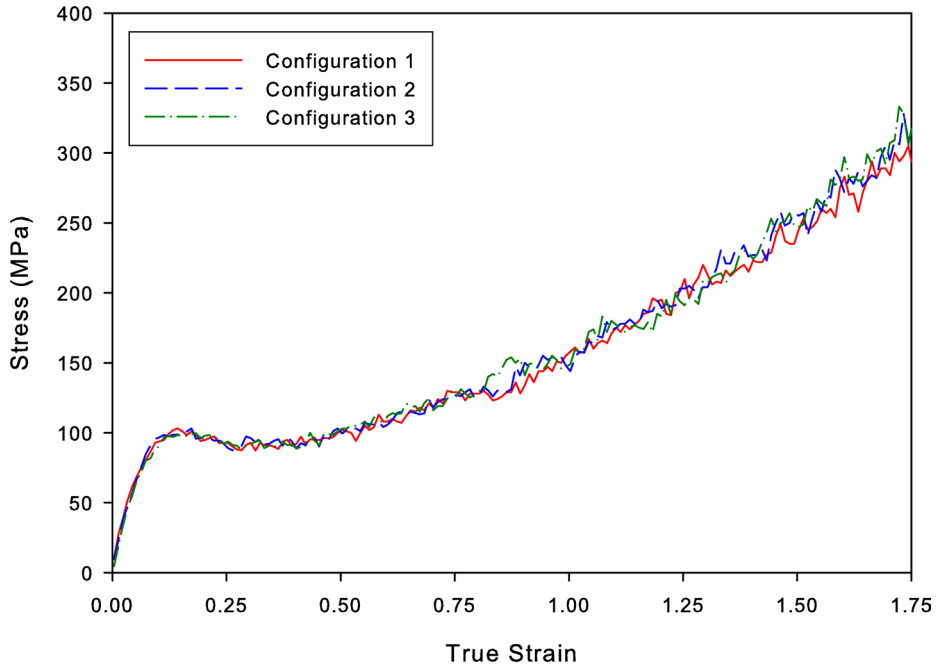

Figure 2.5 Comparisons between the stress-strain behaviors of polymer systems consisting of 50 molecules each with 1000 unified atoms with different initial configurations at a temperature of 300 K and a true strain rate of 10^{10} s^{-1}.

Other MD parameters that must be considered for their effects on the deformation behavior are the integration time step size, the frequency of scaling the simulation box to correspond with the desired deformation rate, and the values of the temperature and pressure dampening parameters. Small integration time steps result in more accurate dynamics, but at a computational cost. Increasing the integration time steps too much can result in numerical instabilities. For example, if two atoms are approaching one another at a high enough velocity, a large integration time step could permit the atoms to overlap during the next integration step resulting in a numerical singularity for typical pair potentials. The goal is to find the largest time step while maintaining the desired accuracy and stability. Integration time steps of 0.5, 1.0, and 2.0 fs were evaluated. An integration time step of 2.0 fs occasionally caused numerical instabilities which resulted

in crashes of LAMMPS. There were no significant differences between the 0.5 and 1.0 fs integration steps at true strains below true strains of 1.75 (Figure 2.6). Therefore, the integration time step of 1.0 fs is used throughout this research since it will require half as much computational resources for a given simulation than the 0.5 fs integration step and does not lead to the occasional crashes as with the 2.0 fs time step.

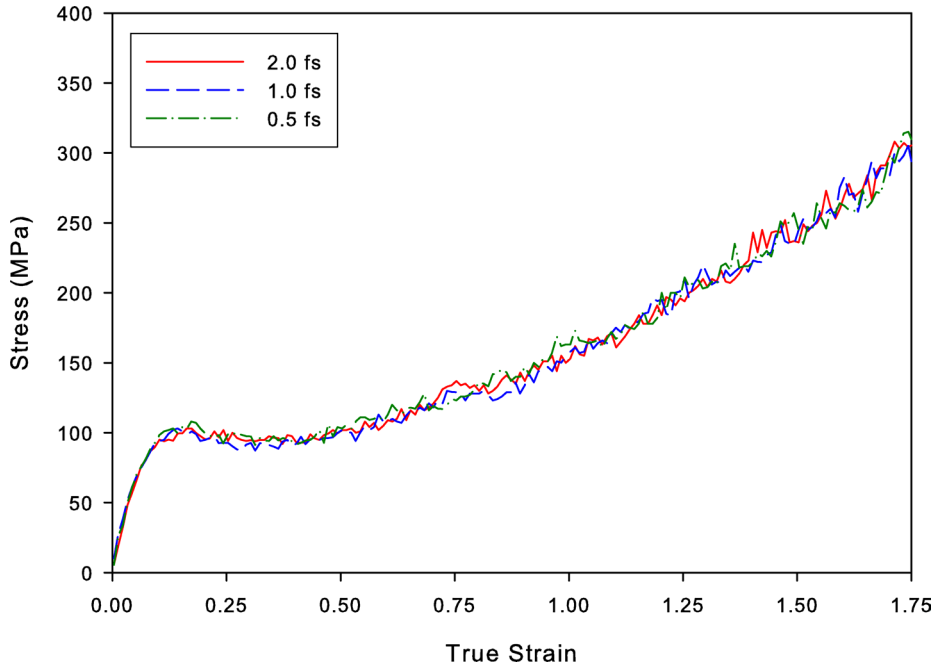

Figure 2.6 Comparisons between the stress-strain behaviors of polymer systems consisting of 50 molecules each with 1000 unified atoms using integration time steps of 0.5, 1.0, and 2.0 fs at a temperature of 300 K and a true strain rate of 10^{10} s^{-1}.

During the deformation process, the MD simulation box must be rescaled to represent the change in shape of the simulation box. Since this rescaling requires computational time to reposition all of the atoms, the rescaling should only be performed as frequently as necessary. The stress-strain behavior was evaluated with the simulation box being rescaled every 1, 10, and 20 time steps. Since there were not any significant

differences between the stress-strain behaviors due to the frequency of the rescaling (Figure 2.7), the simulation cell is rescaled every 20 time steps.

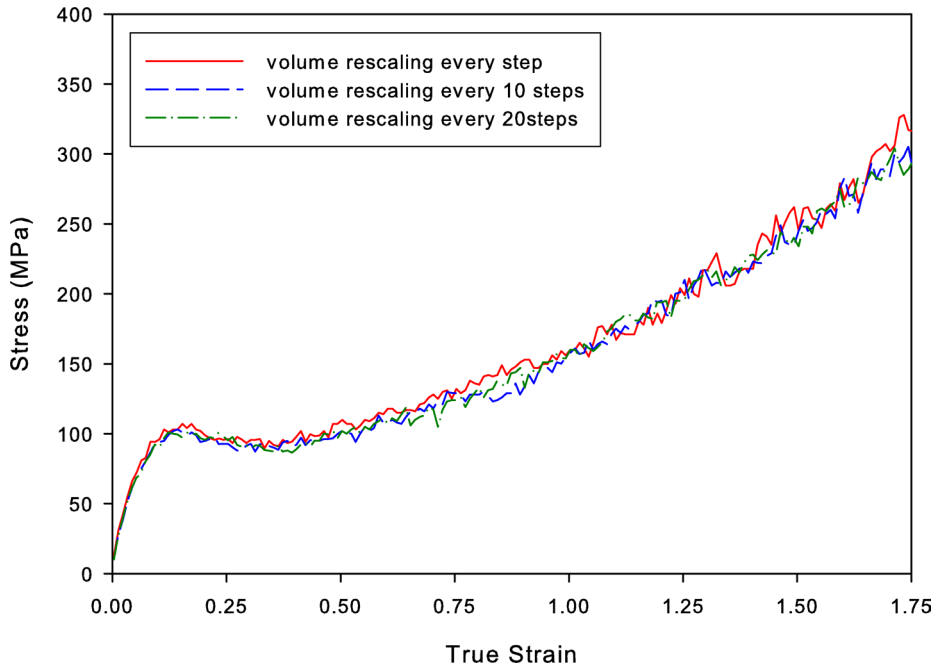

Figure 2.7 Comparisons between the stress-strain behaviors of polymer systems consisting of 50 molecules each with 1000 unified atoms, rescaling the simulation box every 1, 10, and 20 time steps at a temperature of 300 K and a true strain rate of 10^{10} s^{-1}.

By default, rescaling all of the atoms in the simulation cell in the draw direction will result in affine deformation. Another approach would entail just modifying the simulation cell dimensions and not directly repositioning the atoms. As a result, bonds traversing a cell boundary would suddenly have their lengths changed, affecting these bond forces. These bond forces would subsequently result in an eventual repositioning of the remaining atoms as lower energy states are sought. Arguably, this approach more realistically mimics actual material deformation. A simulation was run using this approach and compared to the default affine deformation method. The stress-strain plots

in Figure 2.8 indicate that non-affine deformation results in more compliant behavior at higher strains than affine deformation. At high true strains where the difference between affine and non-affine behaviors become prominent, the chains are mostly elongated in the direction of deformation. With affine deformation, the chains are stretched almost uniformly throughout their lengths; while with non-affine deformation, the chains are stretched from their ends. Pulling from the chains ends facilitates sliding of chains past one another, resulting in lower stresses than the affinely deformed system. To better represent actual polymer behavior, the non-affine behavior is used in the simulations in this research.

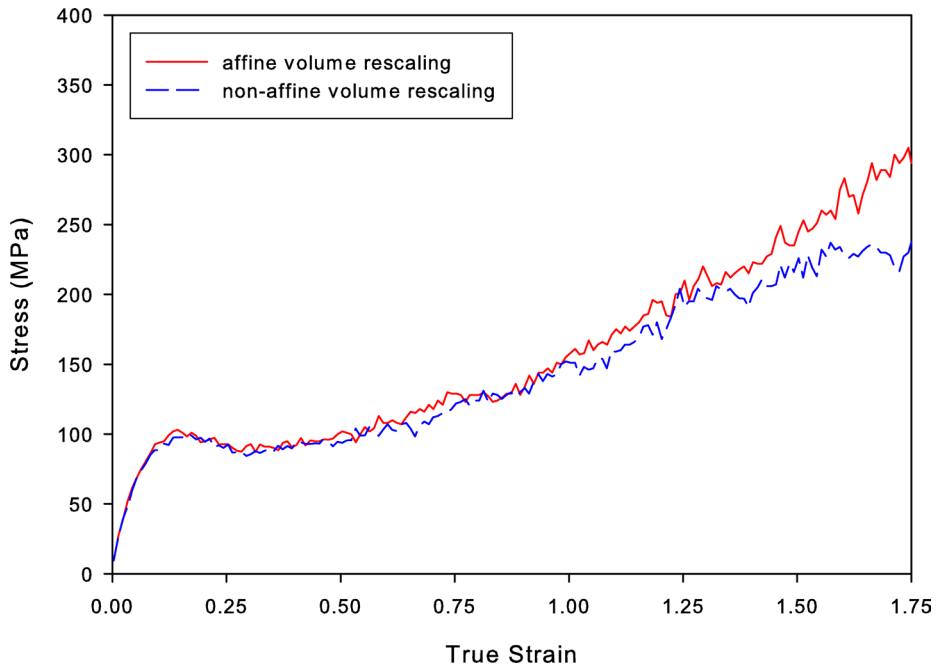

Figure 2.8 Comparisons between the stress-strain behaviors of polymer systems consisting of 50 molecules each with 1000 unified atoms, with affine and non-affine deformation during rescaling of the simulation box every time step at a temperature of 300 K and a true strain rate of 10^{10} s^{-1}.

The NPT ensemble regulates the system temperature and pressure with external temperature and pressure baths. Dampening parameters are used to adjust the flux between the simulation system and the baths. The parameters need to be set such that the system temperature and pressures are damped enough to prevent severe oscillations but not too much such that the system reaches its quasi-equilibrium point too slowly, especially for the high strain-rate deformation simulations. Three values for each of the temperature and pressure dampening parameters were evaluated. For the temperature dampening parameter, a value of 500 fs^{-1} resulted in too little dampening, causing severe temperature oscillations during the relaxation simulation (Figure 2.9) and poor representation of the yielding behavior during deformation (Figure 2.10). The values of 5 and 50 fs^{-1} resulted similar behaviors in the stress-strain results during deformation; however, the 5 fs^{-1} dampening resulted in severe oscillations during the initial picoseconds of the relaxation simulation.

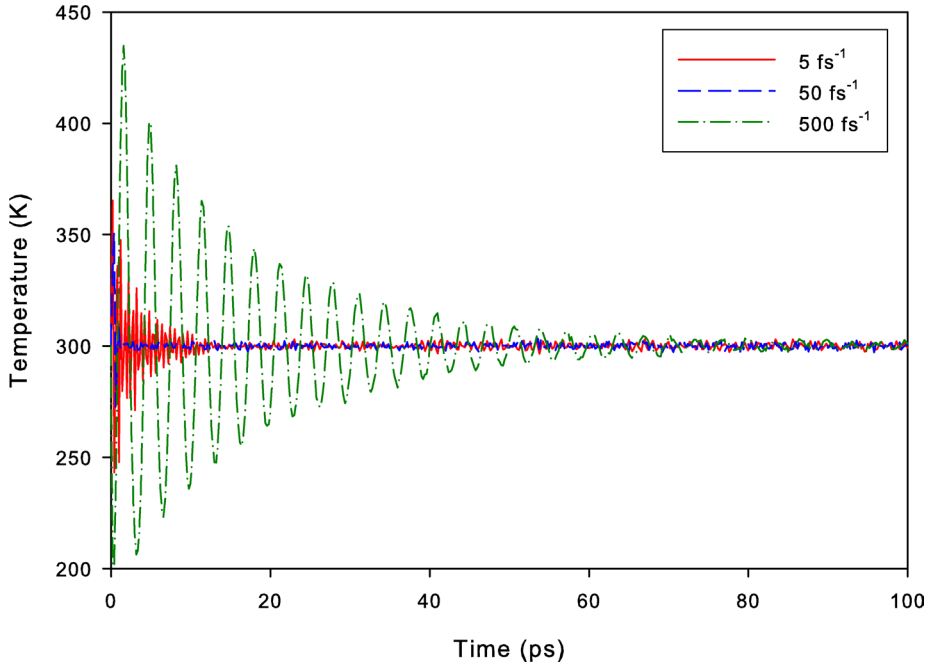

Figure 2.9 Comparisons between the temperatures of polymer systems consisting of 50 molecules each with 1000 unified atoms during relaxation with temperature dampening parameters of 5, 50, and 500 fs^{-1}.

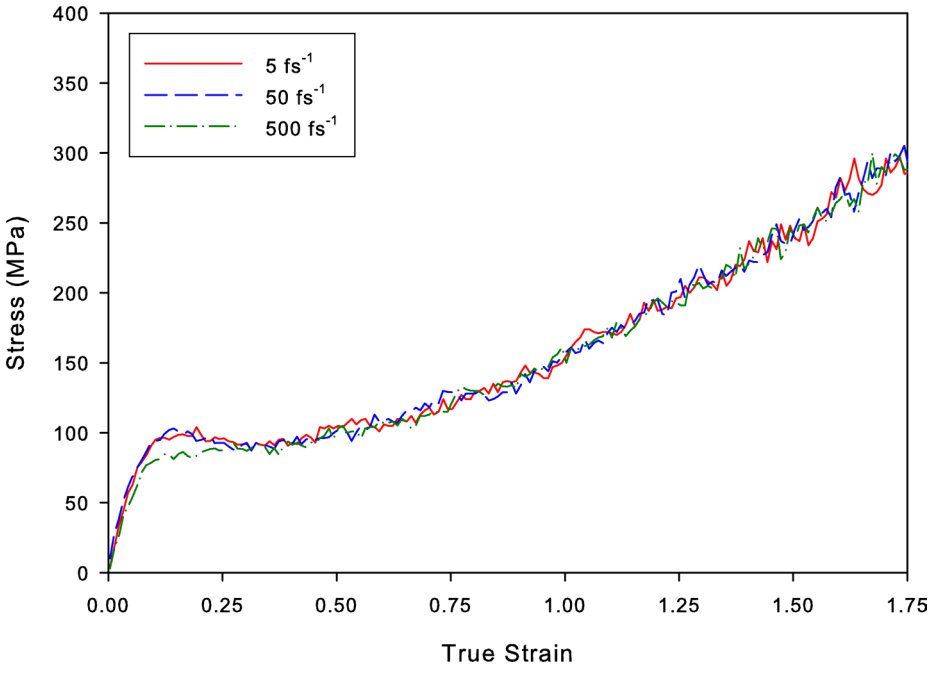

Figure 2.10 Comparisons between the stress-strain behaviors of polymer systems consisting of 50 molecules each with 1000 unified atoms with temperature dampening parameters of 5, 50, and 500 fs^{-1} at a temperature of 300 K and a true strain rate of 10^{10} s^{-1}.

A pressure dampening parameter of 10,000 fs^{-1} resulted in higher pressure oscillations that converged to the equilibrium pressure much more slowly during the relaxation simulation (Figure 2.11). The value of the pressure dampening parameter did not have a noticeable effect on the stress-strain results during deformation (Figure 2.12).

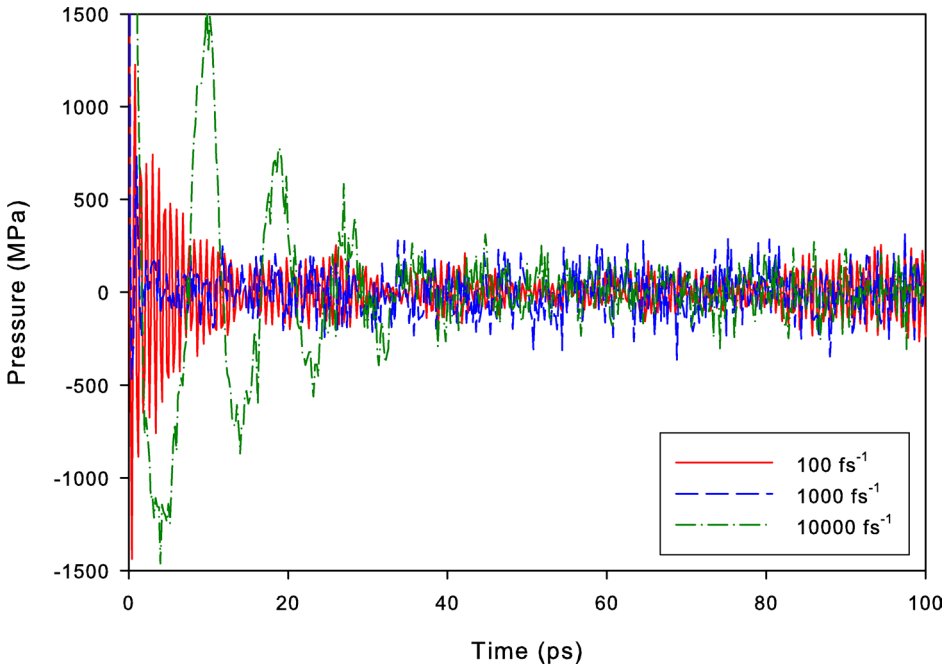

Figure 2.11 Comparisons between the pressures of polymer systems consisting of 50 molecules each with 1000 unified atoms during relaxation with pressure dampening parameters of 100, 1000, and 10000 fs^{-1} at a temperature of 300 K.

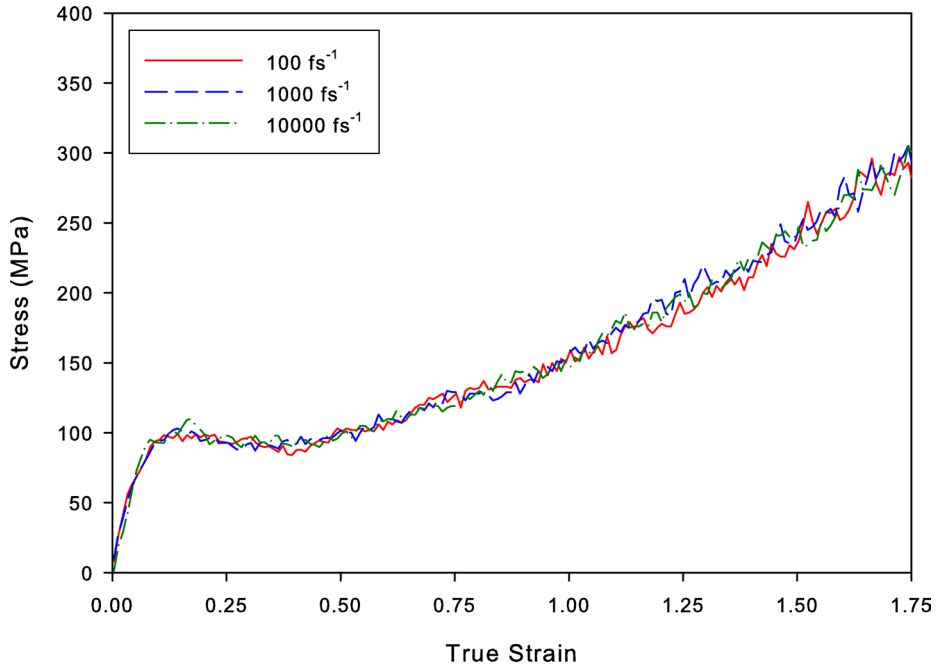

Figure 2.12 Comparisons between the stress-strain behaviors of polymer systems consisting of 50 molecules each with 1000 unified atoms with pressure dampening parameters of 100, 1000, and 10000 fs^{-1} at a temperature of 300 K and a true strain rate of 10^{10} s^{-1}.

Conclusions

This parametric study was useful for gaining a better understanding of the sensitivities of the various parameters used in the molecular dynamics performed in this research and gaining confidence in the accuracy of the simulations. Some compromises were made when selecting parameter values when significant reductions in computational expense could be achieved at the cost of high strain accuracy, specifically the overall number of atoms in the system. When accurate quantitative data is required at high strains, the simulations should be run with a larger system size. Also of interest is the significant effect that non-affine deformation has on the stress-strain results at high strains. The use of non-affine deformation of polymer systems with MD has not been

reported in the literature that was reviewed for this research. With this parametric study complete, the values of the parameters used throughout this research are given in Table 2.1.

Table 2.1 MD parameters used throughout this research.

Integration Time Step	Δt_{MD}	1 fs
Volume Rescaling Frequency	ω_{vol}	20 steps
Temperature Dampening	T_{damp}	50 fs^{-1}
Pressure Dampening	P_{damp}	1000 fs^{-1}

CHAPTER 3

GENERATION OF POLYMER INIITIAL CONFIGURATIONS

Introduction

The generation of the initial state of a polymer system is one of the most complex aspects of atomistic modeling of polymers. Typical polymer systems of interest are generally not ordered enough to generate simplistic crystalline-like configurations nor are they random enough to create completely arbitrary configurations. The "random order" of the polymer systems must be correctly captured in order for atomistic simulations to yield reasonable and relevant results. The initial structure needs to consist of likely configurations. Additionally, the topology of the polymer molecules may need to be specified, whether they be branched, ring, or linear. There may also be a desire to control other aspects of the order of the polymer system such as orientation or degree of crystallinity.

In general, the criteria for a good configuration are to minimize the potential energy of the system and to create molecules that have realistic structural attributes such as the end-to-end lengths, radius of gyrations, and distribution of rotational isomeric states. The system should also be well dispersed and have a realistic overall density at a given pressure.

Since large scale relaxation processes involving an entire polymer chain occur over time periods much longer than can be simulated using atomistic modeling methods, it is imperative that the initial structure be generated as close to the relaxed configuration as possible. Otherwise, the long relaxation times of polymers would require simulation

times too long to effectively establish relative equilibrium. In essence, the generation of the initial polymer structure is a partial solution to the time scale problem in that the relaxation processes which are much too slow to model with atomistic methods are already accounted for in the initial structure.

A multitude of initial configuration generation methods have been presented in the literature, but none of them create configurations close to equilibrium with realistic structures and permit sufficient control the resulting structure. The earliest methods attempted to mimic the polymerization process (Rigby and Roe 1987) with additional cross-linking (Duering et al. 1994). In these methods, the system is randomly populated with dispersed monomers. Special potentials are used to establish bonds between nearest neighbor monomers. Continuation of this process forms long chains. Because of the lack of control over the bonding process and general randomness of this method, many unbonded monomers remain. It can also be difficult to specify consistent chain lengths or control the distribution of chain lengths. There is also no control over the orientation or other statistical properties of the polymer system. The formation process also generates high dihedral energies that relax very slowly.

Instead of starting with all of the monomers already placed in the system, another class of polymer generation methods creates the polymer chains by adding monomers directly to growing chains in the system in a stepwise manner. The addition of these monomers can be performed by random walk algorithms or rotational isomeric state (RIS) algorithms (Flory 1974). The RIS algorithms use the probabilities of the different isomeric states for the particular polymer occurring in actual polymer chains. While the RIS algorithms generate more realistic configurations, they require previous knowledge

of the RIS probabilities and require more computational time. The algorithms for the stepwise creation of the chains can permit atoms to initially occupy the same space. While allowing atom overlaps reduces the complexity of generating the initial chain configurations, the overlaps need to be eliminated prior to use in a simulation; otherwise, numerical instabilities will typically occur due to the fact that most pair potentials are singular as the separation distance approaches zero. Typically, special potentials that sufficiently separate the atoms without numerical problems are used prior to simulation. These "soft core" potentials do not result in numerical singularities as the atom-to-atom distance approaches zero. However, the overlaps are resolved by local motions that result in an increase in energies associated with bond lengths, bonds angle, and dihedral angles for the remainder of the polymer chain. Non-uniform distributions of monomers may also occur, with high densities occurring in regions where overlaps occur. Accounting for long range interactions by modifying the RIS probabilities to include pair energies can better disperse the polymer chains (Theodorou and Suter 1985). High temperature annealing has also been used to reduce the chain energies by increasing the rate at which chain motions occur (McKechnie et al. 1992; McKechnie et al. 1993).

To avoid the issues caused by permitting initial atom overlaps, self avoiding random walk algorithms can be implemented. These algorithms are typically more complex and require more computational time than the methods that permit overlaps. Additionally, chains can grow into regions where there are no possible completion paths due to the growing end being surrounded by neighboring atoms, a problem that becomes significant at high densities. The added constraints of volume exclusion lead to an

unrealistic increase in the number of *gauche* RIS states, resulting in a reduced number of *trans* RIS states (McKechnie et al. 1992).

In order to circumvent the difficulties of generating an initial configuration at high densities, Sok et al. (1992) proposed the generation of random walk chains at very low densities. The simulation cell would then be compressed to the desired density using a soft core potential, i.e.,

$$V_{sc} = V_{sc_{max}} \left(1 - \left(\frac{r}{r_{sc}} \right)^2 \right)^2 \qquad r < r_{sc} \tag{3.1}$$
$$= 0 \qquad r \geq r_{sc}$$

Here, r_{sc} is the cutoff distance and $V_{sc_{max}}$ controls the magnitude of the potential. The attractive portion of the potential is excluded to prevent clustering during compression. This soft core potential will permit atoms to pass through one another which helps reduce the amount of localized high-energy areas. However, some high energy regions are still created and cannot be relaxed within a reasonable simulation time. Additionally, the compression method tends to create relatively isolated chains with few entanglements. Modifying this method to only include the repulsive portions of the Lennard-Jones pair potential was found to distribute the atoms more uniformly (van der Vegt et al. 1996). Control over the final structure is also difficult due to compression effects. When the chains are created at a very low density, there are few entanglements between the chains and the compression process does not create further entanglements as shown through an example described in detail later (Figure 3.1). Also, the final end-to-end distance, *trans* – *gauche* RIS distributions, radius of gyration and other relevant properties cannot be

reliably controlled with this method. Additionally, the MD compression step can require a significant amount of computational time, especially for large systems.

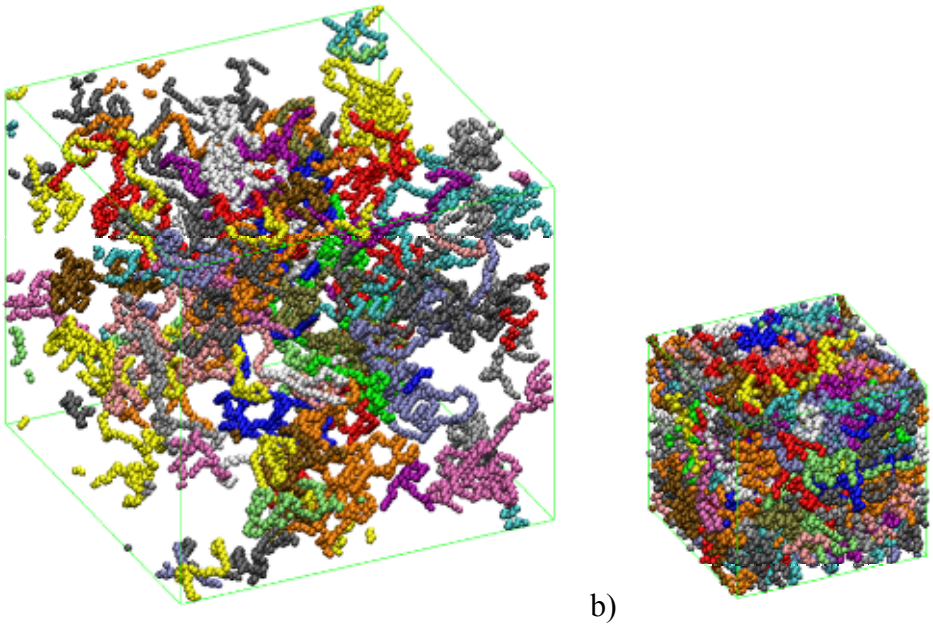

a) b)

Figure 3.1 An example of an initial configuration generated at a low density of 0.11 g/cm^3 (a) and the final compressed configuration at a density of 0.91 g/cm^3 (b) showing the relative lack of molecular entanglements.

Initial configurations generated at density with overlaps and subsequently relaxed were compared to configurations generated by the low density/compression methods using the repulsive portions of the soft core and Lennard-Jones potentials. Solubility of small molecules was simulated with MD for each of the configurations. Solubility was chosen because it is a good indicator of the density distribution and homogeneity of the initial structure (van der Vegt et al. 1996). They found that the low density/compression method gave the lowest initial energies and was closest to experimental results.

A novel method was introduced by Faulon et al. (1997) that permits the generation of polymer systems at the desired density without the problem of the growing

end being trapped, preventing further growth. The principle behind this method is to create straight, low molecular weight preliminary chains with the same end-to-end length as the desired final, higher molecular weight chains. Two end points are selected on a lattice which are separated by the predetermined length, usually the characteristic length ($<r^2> = N C_{inf} l^2$), of a polymer molecule consisting of N segments or bonds. This process permits the stepwise growth of the chains to be performed at relatively low densities since the straight chains will consist of much fewer atoms than the final, fully grown chains. The straight chains are grown to the final molecular weight by randomly removing a bond and inserting a specified number of new bonded polymer segments in its place (Figure 3.2). This insertion process also uses shortest distance algorithms and is repeated until the chain has the desired molecular weight.

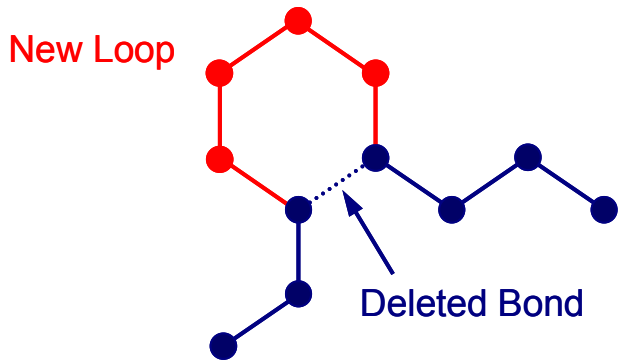

Figure 3.2 Diagram showing the insertion process of the Faulon et al. initial configuration generation method.

Since the chain can be grown from any interior bond, there is a higher likelihood of finding vacant neighboring sites to add more atoms. So instead of only having a single site from which to grow the chain, as in the stepwise method, there are N_s sites, where N_s becomes larger as the system becomes denser and fewer lattice sites are available.

Volume exclusion is taken into consideration by not allowing more than one atom at a single lattice point. X-ray scattering intensities, initial energies, and diffusion of small molecules determind by MD simulations using the resulting initial configurations indicates that this method performs as well as the low density/compression mthod but has the advantages of requiring less computational resources and allowing greater control over the topology of the generated polymer system. The process of generating the preliminary chain and inserting atoms entails shortest distance algorithms for computational simplicity at the cost of limiting the amount of control over the configuration of the new chains, especially when specific rotational isomeric states are desired. Another limitation is that only backbone atom exclusion is considered which results in the van der Waal forces being initially excessive due to the interactions between side atoms and chains, resulting in the chains being initially too compressed.

Method

For this research, a method is desired that permits a greater amount of control over the characteristics of a high density initial configuration and generates a low energy, near equilibrium configuration. The method presented here permits relaxed dense polymer systems to be created with reasonable computational expense and permits the control of the distribution of rotational isomeric states, end-to-end distances, radius of gyration, number of atoms per molecule, number of molecules in the system, and the system density.

Lattice

In order to efficiently track volume exclusion and limit the degrees of freedom in the system, a lattice is utilized to position the atoms. The lattice does have the disadvantage of constraining the configurations available to the molecules to be grown on the lattice. This limitation can become significant if the lattice topology does not closely resemble the topology of the polymer molecules to be modeled. For instance, cubic lattices are commonly used when generating initial configurations due to the relative ease at which they can be implemented into computer programs. A typical three dimensional array that is available in almost any computer language can be easily correlated to a cubic lattice since the positions of a cubic lattice map directly to the array while the adjacent elements in the array represent the connectivity of the lattice. However, the backbones of most polymers consist of carbon or other atoms that do not have bond angles that correspond to the 90 and 180 degree connectivity angles in a cubic lattice. While there are methods to extend the connectivity beyond the nearest neighbors to allow more flexibility with the bond angles and lengths, this added complexity negates the simplicity offered by the traditional use of the cubic lattice. The primary deficiencies of the cubic lattice can also be overcome by implementing a diamond or tetrahedron lattice. These lattices have an angle between neighboring lattice points that is very similar to the common carbon-carbon bond angle. However, the connectivity mapping between the coordinates and a memory array of a diamond lattice are much more complex. The method presented here is general to the application of practically any lattice. In the implementation section, the specifics of mapping cubic and diamond lattices to computer arrays are detailed.

Generation of molecules

Molecules are added to the lattice in a step-wise manner. For each molecule, the first atom is added to an available site on the lattice. Then the molecule is grown by successively adding atoms to available neighboring lattice sites. Here, "atoms" refers to any component of a molecule such as an actual single atom or collections of atoms such as unified atoms consisting of side atoms or chains, or even entire monomers. Atoms are added in this manner until the desired length of the molecule has been achieved. The effectiveness of this method to generate molecules with specific characteristics is determined by the manner in which neighboring lattice sites are selected for the placement of atoms. The initial configuration generation method presented here is based on a method to make the appropriate selection of neighboring lattice sites. This selection process will be detailed later, but first, an overview of process to generate molecules and assemblies of molecules is presented.

In a similar manner to the Faulon et al. (1997) method, the fundamental goal is to create a low molecular weight version of the final molecule so that the initial molecules are generated at a low density. By connecting two points separated by the desired end-to-end length with a relatively straight line of atoms, the preliminary molecule will contain significantly fewer atoms than the final form of the molecule. Since additional atoms can be inserted at any point in the molecule, the likelihood of completing the molecule at high densities is greatly increased. By systematically controlling the methods by which the atoms are inserted into the chain, the desired properties of the final molecule can be achieved. A schematic diagram of this process is provided in Figure 3.3.

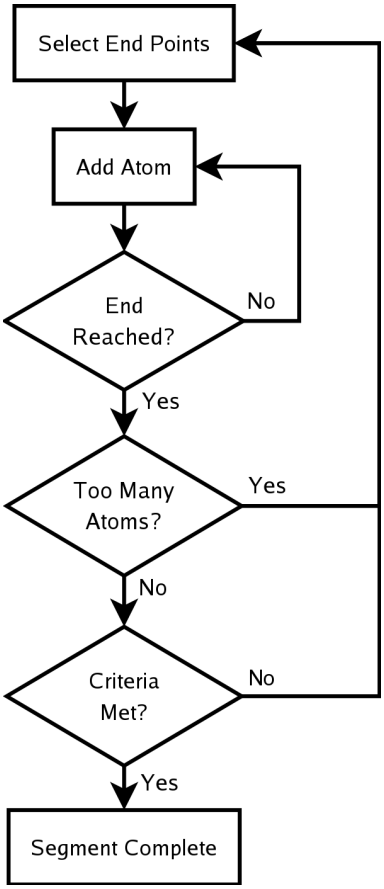

Figure 3.3 Schematic showing the preliminary segment generation algorithm.

The initial step of generating a molecule involves the selection of two lattice sites on which the end points of the molecule will be placed. The selection of lattice sites for the endpoints can either be at random or directed by finding sites in low density regions or at specific orientations or distances from one another. By defining the separation distance, the end-to-end length of the resulting molecule is then specified, though the discrete nature of the lattice spacing precludes exact specification of the separation distance. Instead of initially selecting both of the end points, an alternative method entails only the selection of the starting lattice site and determining the end site after

growth has commenced and specific criteria are met, such as end-to-end distance. An advantage of this alternative method is that the likelihood of successfully completing the preliminary chain is increased since a specific end point does not have to be reached. This advantage is particularly beneficial when a large number of short molecules are to be generated such that the last molecules are being generated at relatively high densities.

The preliminary chain is grown from the starting atom by selecting a neighboring lattice site. The number of neighbors for each lattice site and the geometric direction to each neighboring site is dependent upon the topology of the lattice. For example, each lattice site on a diamond lattice has four neighboring lattice sites (Figure 3.4). Each lattice site on a cubic lattice has six neighboring lattice sites.

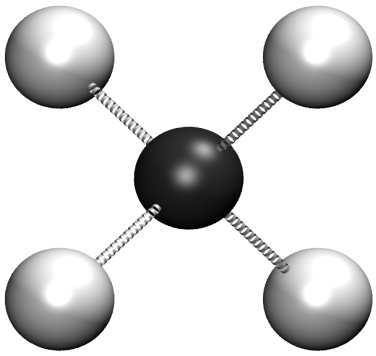

Figure 3.4 Diagram of an initial atom (black) on a diamond lattice and the possible neighboring sites (white).

If volume exclusion is incorporated into the procedure, sites containing previously located atoms of the growing preliminary chain or atoms from previously generated chains may reduce the number of available neighboring sites (Figure 3.5).

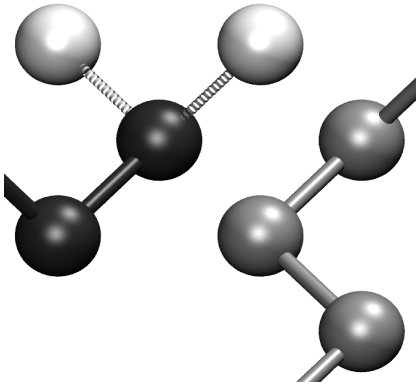

Figure 3.5 Diagram showing a reduced number of available neighboring sites (white) as a result of the previous atom in the chain (black) and an atom from another molecule (gray).

From the available neighboring sites, a single site needs to be selected for the placement of the next atom to continue the growth of the chain. The selection process is based on the combination of several criteria. Examples of criteria include random selection, selection of the neighboring site closest to the least dense area in the simulation cell, selection of the neighboring site that is closest to the pre-selected end point, selection of the neighboring site with the lowest energy, and selection of the neighboring site that results in a specific RIS. The specifics of these criteria will be described in detail in the next section. Each of these criteria assigns a selection probability to each neighboring lattice site. For each neighboring lattice site, these probabilities are weighted and then combined, creating a selection probability table that can be used to determine which of these sites should be selected. A sample probability table is shown in Table 3.1, with Figure 3.6 mapping these probabilities onto the available neighboring sites of an atom on the lattice.

Table 3.1 Example probability table.

	Weighting Factor	Neighbor		
		1	2	3
Closest-to-End	0.1	0.0	0.6	0.4
Least-Dense	0.1	0.3	0.7	0.0
Lowest-Energy	0.3	0.3	0.1	0.6
RIS	0.5	0.2	0.2	0.6
Total		**0.2**	**0.3**	**0.5**

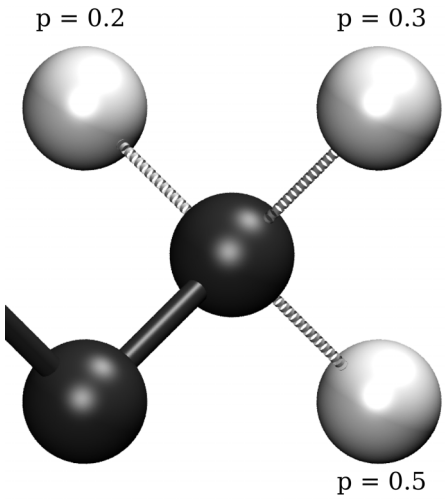

Figure 3.6 Diagram showing the available neighboring sites (white) of a molecule (black) on diamond lattice with associated selection probabilities.

For the random selection criterion, each neighbor is assigned an equal probability. The probability is simply defined as the inverse of the number of available neighboring sites. For example, if there are four available sites, each site would be assigned a probability of 0.25.

For the closest-to-end criterion, the distance from each available neighboring site to the end point is calculated. The distance of the furthest neighbor is used as the base distance (Figure 3.7). The differences between the base distance and the distance to each

neighbor from the end point is used to calculate the selection probability of each available site, i.e.,

$$p_i = \frac{fd_{\max} - d_i}{nfd_{\max} - \sum_{j=1}^{n} d_j}, \tag{3.2}$$

where n is the number of available sites, d_{max} is the longest distance, and f is a weighting factor that determines the dependence of the probabilities on the overall distance. When $f = 1$, the probabilities are independent of the overall distance with the lowest probability always being equal to zero. An example with $f = 1$ is given in Table 3.2.

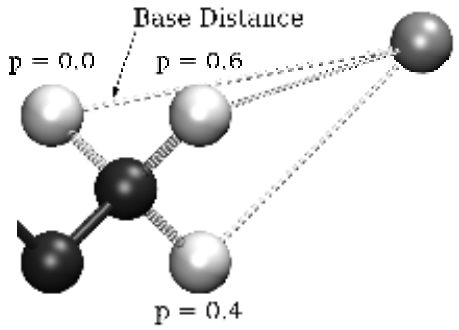

Figure 3.7 Diagram showing the available neighboring sites (white) of a molecule (black) on a diamond lattice with associated closest-to-endpoint criterion selection probabilities to the end point (gray).

Table 3.2 Closest-to-end point criterion probability calculations.

Neighbor	Distance (Å)	Difference (Å)	Probability
1	52.5	0.0	0.0
2	51.0	1.5	0.6
3	51.5	1.0	0.4

The probabilities for the least-dense criterion are determined in a similar fashion as the closest-to-endpoint criterion. The only difference being that the distance to the

least dense lattice site is used rather than the distance to the end point. The effective density for each lattice site, ρ_i, is determined by

$$\rho_i = \sum_{j=1}^{n} \frac{m_j}{d_{ij}} \tag{3.3}$$

where n is the total number of atoms in the lattice, m_j is the mass of atom j, and d_{ij} is the distance between lattice site i and atom j. The lattice site with the lowest value is considered to be the least dense lattice site. If multiple sites have the same minimum density, the least dense site is chosen at random from this pool of sites. Limiting the sites used in the calculation so that they are within a certain distance of the available neighboring sites permits local regions rather than the entire system to be targeted. This reduction of the sites analyzed decreases the amount of computational resources required, but may not even out the overall system density.

For the RIS criterion, the probability assigned to each neighbor is determined by the probability of a specific RIS configuration (eg. *trans*, *gauche*$^+$, *gauche*$^-$, as explained below) that would be formed if that neighbor were selected based on the locations of the current and previous atoms required to determine the RIS. These probabilities are typically available for most polymers in the literature or can be easily calculated (Mattice and Suter 1935). The number of possible RIS configurations is dependent upon both the lattice type used and the polymer being modeled. For example, polyethylene on a diamond lattice has three RIS configurations; *trans*, *gauche*$^+$, and *gauche*$^-$. The probability of each configuration occurring is dependent upon the previous RIS, thus the probabilities are conditional probabilities for more realistic solutions. Table 3.3 shows the probability table for polyethylene on a diamond lattice (Sharaf et al. 2001).

Table 3.3 RIS probabilities for polyethylene on a diamond lattice.

Current RIS	Previous RIS		
	Trans	***Gauche*$^+$**	***Gauche*$^-$**
Trans	0.5909	0.7382	0.7382
***Gauche*$^+$**	0.2045	0.2555	0.0064
***Gauche*$^-$**	0.2045	0.2555	0.0064

Figure 3.8 shows a sample polyethylene molecule ending in a *trans* state and the RIS probabilities for each available site corresponding to their state (*trans*, *gauche*$^+$, *gauche*$^-$).

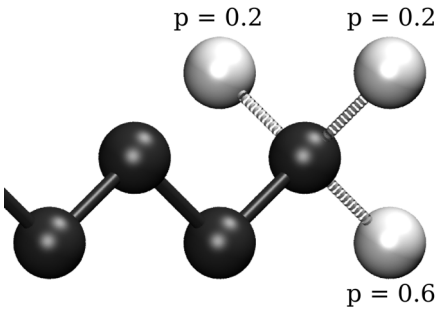

Figure 3.8 Diagram showing the available neighboring sites (white) of a molecule (black) on a diamond lattice ending in a *trans* state with associated RIS criterion selection probabilities.

For the lowest-energy criterion, the total energies after establishing a bond with each available neighbor are determined. The energies are typically functions of the bond length, bond angle, dihedral angle, and/or non-bonded pair interactions. For each available neighbor, the energies associated to connecting with this neighboring atom with all of the atoms within a cut-off distance would be summed. The selection probability for each available neighbor, p_i, is proportional to the inverse of the energy for that neighbor, i.e.,

$$p_i = \frac{\frac{1}{E_i}}{\sum_{j=1}^{n} \frac{1}{E_j}}, \tag{3.4}$$

where E_i is the energy for the neighbor and n is the total number of neighbors within the cut-off distance.

Once the probability table is completed, one of the neighbors can be selected. The selection process begins by calculating the cumulative probability of all available neighbor sites (by summing the weighted probabilities for all of the available neighbors for the current end atom) and then generating a random number between zero and this cumulative probability. The probabilities are then summed again, though only one probability at a time, with this intermediate sum being compared to the random number. The probability of the neighbor that increases the intermediate sum above the value of the random number is selected. For example, if three neighbors to the end atom have the probabilities of 0.2, 0.1, and 0.5, then a random number is generated between 0.0 and 0.8. If this number falls in the range of 0.0 to 0.2, the first neighbor will be selected. If the random number falls in the range of 0.2 to 0.3, the second neighbor will be selected. Any other random number would fall in the range of 0.3 to 0.8, which would result in the third neighbor being selected. The spans of these intervals are the same magnitudes as the probabilities for the corresponding neighbor.

The weight given to each criterion has a significant effect on the likelihood of a preliminary chain to be completely grown to the desired length and on the properties of a successfully generated preliminary chain, such as RIS configuration ratios or energies. If RIS or random criteria are weighted too heavily, the chain growth could meander in a way that generates too long of a chain or grows into a lattice site completely surrounded

by occupied sites, preventing further growth. The least dense criterion is useful to improve the distribution of atoms in the system to be more uniform, but can lead a growing chain away from the end point or generate a poor distribution of RIS configurations. Giving full weight to the closest to end point criterion will result in a near linear preliminary chain as is accomplished with the Faulon et al. (1997; 2001) method. The linear preliminary chain often results in unlikely configurations for the completed molecule as the chain tends to grow more in the center leaving the end points near the periphery of the chain, fewer entanglements are created, and *trans* configurations tend to overly dominate RIS distributions.

After a backbone atom is added, side atoms, such as hydrogen, or side chains can be added to neighboring lattice sites, reserving these sites from being occupied by other backbone atoms or side chains to those backbone atoms. In fact, in the process of growing the chain, the potential lattice site to which an atom can be added must be checked to ensure that the side chains can be accommodated.

Once a preliminary chain has been created (Figure 3.9a), it is grown to the desired number of atoms by removing a series of adjacent atoms (Figure 3.9b) and then inserting a larger segment of atoms (Figure 3.9c). This inserted segment is generated in a similar manner as the preliminary chain, except that different weights for the probability criteria are typically used. Different weights are used to improve the likelihood of completing the shorter segments and when additional criteria are desired. The sites exposed by the removal the segment are used as the end points for directing the growth of the segment for insertion. If a replacement segment cannot be generated due to the inability to connect the endpoints of the vacated segment, then the replacement segment is discarded

and the vacated segment is restored. To maintain a likely radius of gyration for the molecule, only segments that approach the desired radius of gyration for the chain would be accepted.

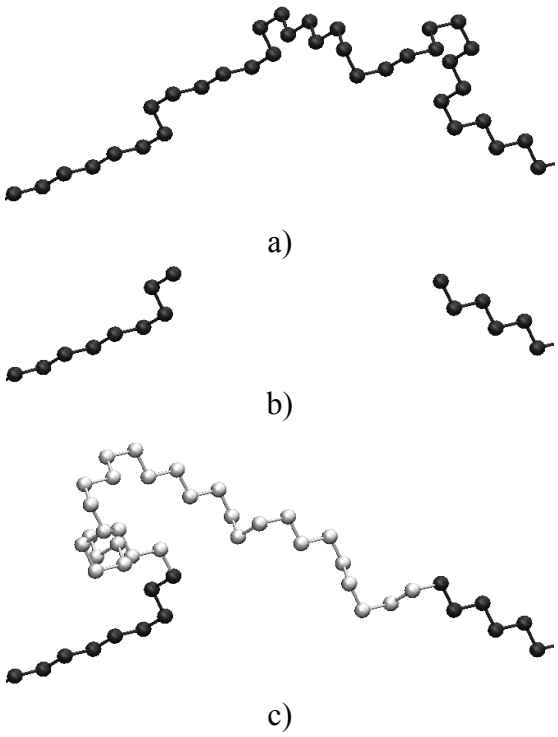

Figure 3.9 The process of growing a preliminary chain, a, by removing a section, b, and then inserting a segment of new atoms, c.

Generation of Polymer Molecular Assemblies

The method of generating relatively short preliminary chains and then filling them in with additional atoms works well for generating assembles of polymers, especially when dense systems are desired. This method reduces the difficulties due to volume exclusion associated with the construction of long molecules. In the traditional method of growing the entire molecule at once, as the system becomes dense, the likelihood is

high that the growing end will become trapped at a lattice site which is completely surrounded by occupied sites. The method presented here alleviates this problem because the preliminary chains are completed while the system is at a relatively low density, enhancing the likelihood of completing these preliminary chains. When growing the completed preliminary chains, instead allowing the growth at only a single location, this method permits almost every site on the chain to be available for growth, substantially increasing the success rate of finding additional sites for growth. A schematic of the polymer system generation algorithm is provided in Figure 3.10.

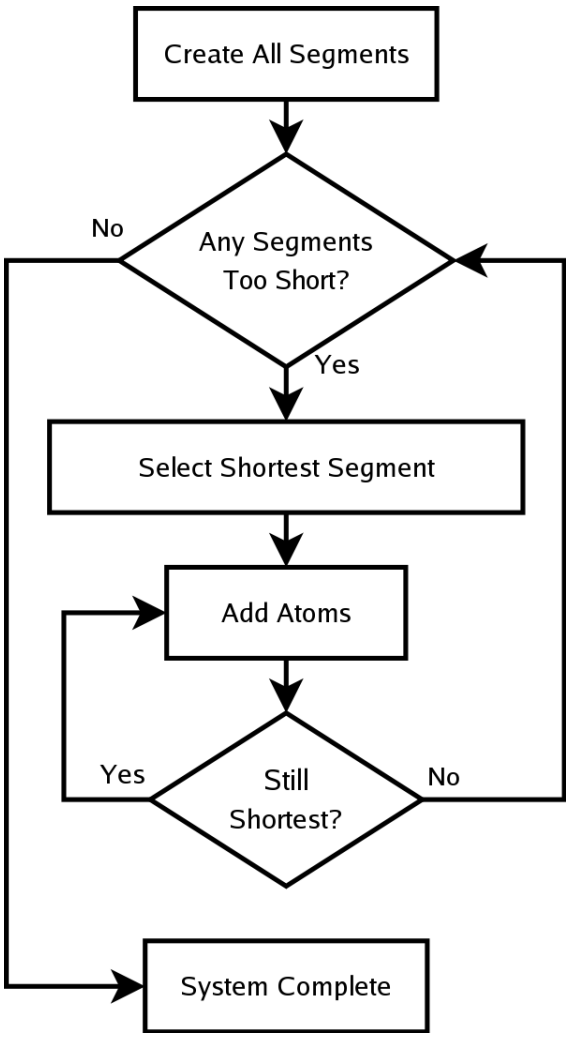

Figure 3.10 Schematic of polymer system generation.

All of the preliminary chains are created sequentially as the first step. It is important that these preliminary chains consist of fewer atoms than desired in the final molecules so that the density of the preliminary system does not become too high, reducing the effectiveness of this method. Limiting the size of the preliminary chains can be accomplished by discarding any preliminary chains that have more than a specified fraction of the total number of desired atoms. Once all of the preliminary chains have been created, they are all grown to their final lengths. An example of a system of

polyethylene atoms generated on a diamond lattice at a density of 0.91 g/cm^3 with full volume exclusion, including the hydrogen side atoms, is shown in Figure 3.11.

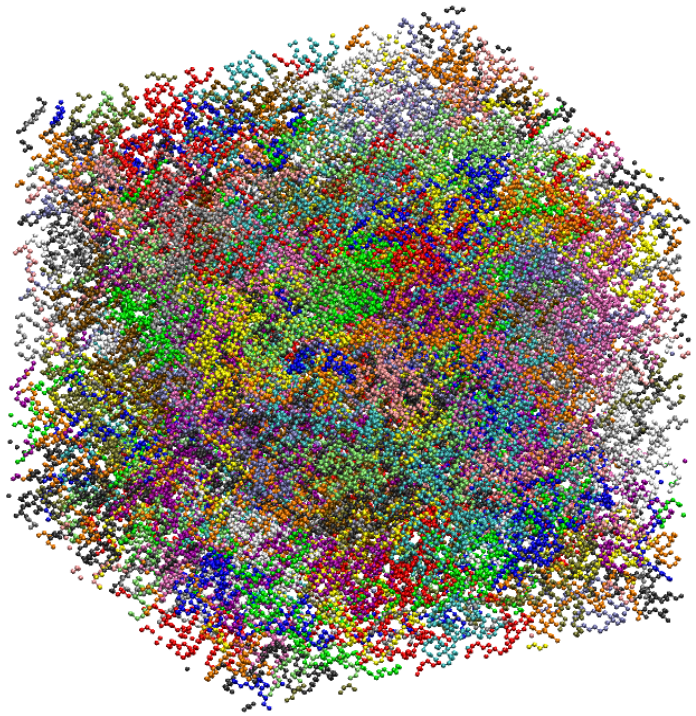

Figure 3.11 Example polymer system at a density of 0.91 g/cm^3.

If the global density of a system becomes so high that the desired configurational characteristics for the molecular assembly cannot be achieved due to the low number of available lattice sites and further generation of molecules becomes either computationally undesirable or infeasible, the volume exclusion condition can be relaxed to make more lattice sites available for growth. During the process of selecting a neighboring lattice site to grow a chain, instead of completely eliminating occupied sites from being selected, a very low probability of selection can be assigned to that neighbor for addition. For example, if a neighboring lattice site is occupied, instead of assigning that site an

effective probability of zero, a multiplier of 0.001 could be applied to the final probability. This small probability will still allow enough atom overlaps to facilitate reasonable computational time. While overlapping of backbone atoms may not be desirable, relaxing the volume exclusion for side atoms will typically increase the probability of incorporating segments with less of an impact on the final configuration. An example of this approach is illustrated with the probability table in Table 3.4.

Table 3.4 A probability table including volume overlap.

	Weighting Factor	Neighbor		
		1	2	3
Closest-to-End	0.1	0.0	0.6	0.4
Least-Dense	0.1	0.3	0.7	0.0
Lowest-Energy	0.3	0.3	0.1	0.6
RIS	0.5	0.2	0.2	0.6
Total		**0.2**	**0.3**	**0.5**
Occupied		0.001	1.0	1.0
Final		**0.0002**	**0.3**	**0.5**

Generation of Network Polymers

Cross-linked networks of polymer molecules can easily be created using the general method presented by Faulon et al. (Faulon et al. 1997; Faulon 2001) and by extension, the method presented here. A benefit of these methods is that the number and locations of cross-links and dangling ends can be specified. However, Faulon et al. did not specify the algorithms for selecting the locations of the end points or the methods for determining the connectivity of the chains in the system. The end points of the molecules are assigned to the locations of the cross-links and dangling ends. After this step, the

previously described methods of growing the chains can be followed with a few modifications.

For the creation of a cross-link or dangling end, a lattice site is selected either at random or using any rule-based selection process. The number of molecular ends that will be assigned to each cross-link site needs to be defined. For example, the functionality of the cross-linker used to generate an actual polymer network could be used. A single molecular end is assigned to each dangling end site. Once the end points of each molecule are assigned to particular cross-links or dangling ends, the molecules can be generated using the process described in the previous sections. The functionality of the cross-linker limits the maximum number of polymer chain ends that can be connected with a cross-link site. The ends of each molecule will be connected with a cross-link site or will be left dangling. Once the connectivity of molecules is completed, molecules can be generated using the process described in the previous sections.

In many cases, instead of randomly assigning the connectivity, the distance between cross-links needs to be taken into consideration. Generally, cross-links closest to one another should be connected to increase the likelihood of the formation of a preliminary chain between them. A more uniform network would result from implementing an algorithm to locate the cross-links to be connected at a distance equal to the characteristic end-to-end length. An advantage with this initial configuration method is that the number of dangling ends, loops, and any other property of the network, can be explicitly defined. An example of a network generated with this method is shown in Figure 3.12.

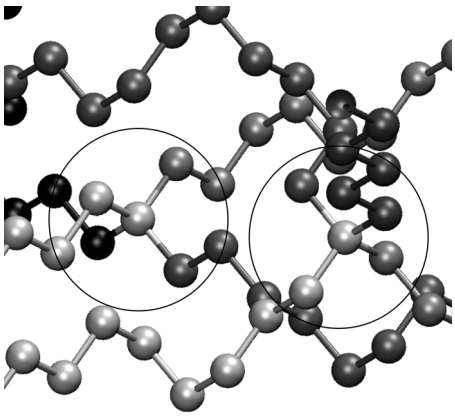

Figure 3.12 Example polymer network system showing two cross-links.

Generation of Ring Molecules

A benefit of the proposed method is that it can be used to easily create ring polymers or macrocyclic rings (Figure 3.13). By simply defining the two end points of the preliminary chain to have the same location, a ring polymer will be created. On a diamond lattice without any nearby occupancy, the initial chain will be a benzene ring. Atoms are then inserted in the same manner they are for a linear molecule.

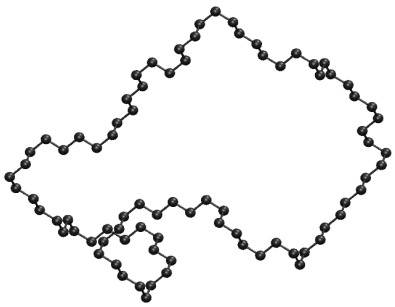

Figure 3.13 Example ring polymer.

Implementation

This method has been implemented in a C++ program taking advantage of the language's object oriented capabilities. The following objects and their contents were created.

Objects

The lattice site objects represent each discrete spatial location on the lattice within the simulation box. These objects contain the geometric coordinates of the lattice site, an array containing pointers (links) to each of the neighboring lattice site objects that bonds can be made to, an array containing pointers to all of the neighboring lattice site objects within a specified cut-off distance, the occupancy state of the site, and the effective density at the site's location. Pointers are used extensively in the program to reduce memory consumption and maintain consistency. By referring to the coordinates and neighbor lists for each lattice site, piecewise operations can be completed without knowledge of the underlying topology. The lattice site objects also contain methods (functions) that add or remove neighbors, determine availability of the site for placement of atoms and/or side atoms, and set the occupancy states of the site.

The base lattice object represents the entire lattice of the simulation box and contains an array holding pointers to all of the lattice site objects in the lattice, an array holding pointers to all of the molecules in the system, the dimensions of the simulation cell, the bond length between neighboring lattice sites, and the various parameters that control chain generation and growth algorithms. This object also contains all of the methods used for the generation of molecules, querying of lattice properties, and

outputting of the entire system to specific file formats used by other programs including LAMMPS and VMD. All of the methods and contents of the base object are valid for all lattice types. Child lattice objects that are specific to the type of lattice, e.g. cubic or diamond, are separate objects which inherit all of the base lattice object's contents and methods and add functionality specific to that type of lattice. This added functionality includes the replacement of base class methods as well as the addition of new methods. For example, RIS generation methods in the base object are just random generation methods since the base class has no knowledge of the lattice structure. The diamond lattice object replaces the base object's RIS generation methods with methods specific to the connectivity of the diamond lattice.

The atom objects represent the atoms that are added to the lattice and contain the actual geometric coordinates of the atom, a pointer to the lattice site object associated with the atom, an array of pointers to other atom objects that are bonded to this atom object, an array of pointers to neighboring lattice sites that contain virtual side atoms (e.g. the hydrogen atoms for a methyl "atom"), and the molecular weight of the atom. Since periodic boundary conditions are assumed for this method, it is possible for the atom's geometric coordinates to differ from the lattice site coordinates at which the atom is located within the simulation cell. The atom geometric coordinates are required to determine molecular properties which extend beyond the simulation cell such as end-to-end length. Methods contained within the atom object add and remove bonded atoms, reserve neighboring sites for side atoms, and suppress and restore atoms from the lattice.

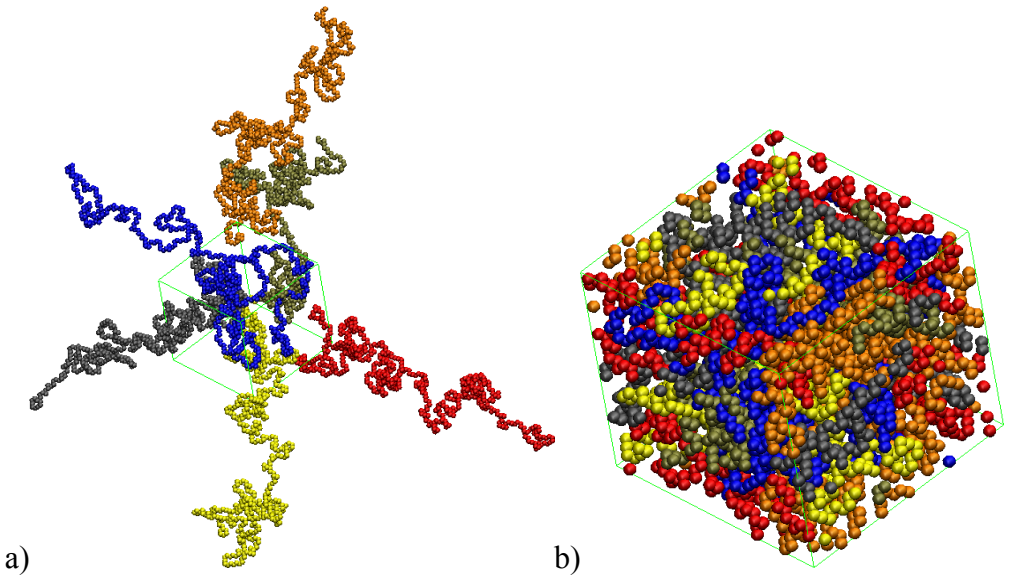

Figure 3.14 A single system configuration showing actual geometric coordinates of each atoms (a) and the lattice site coordinates of each atom (b).

The molecule objects represent all of the molecules and segments in the system and contain the properties of the molecule, an array containing pointers to the atom objects associated with the molecule, and information detailing the order at which different atom types are added to the molecule. The methods found in this object determine the properties of the molecule and add or remove atoms to the molecule

Diamond Lattice

Cubic and diamond lattices were implemented in the software. Representing the cubic lattice as a lattice object was trivial as the cubic lattice topology corresponds directly to a three dimensional array as implemented in C++. Unlike cubic lattices, diamond lattices do not map directly to programming arrays, so a method had to be implemented in the diamond lattice object to associate the diamond lattice topology to a

C++ array. Meyer (1999; 2000) has presented methods and mappings of various lattice geometries to computer memory. The use of object oriented programming methods in this implementation permits the incorporation of any of these lattice geometries including cubic, diamond, honeycomb, and quadrilateral lattices. For a lattice site stored in a memory array, the mappings specify which relative positions in the memory array contain lattice sites that are connected to the current lattice site. For the simple cubic lattice, the mappings for the six neighbors are

$$(1,0,0),(-1,0,0),(0,1,0),(0,-1,0),(0,0,1),(0,0,-1) \tag{3.5}$$

This mapping completes the connectivity of the lattice, but does not give the actual coordinates of each site. The transformation of lattice site indices to geometric coordinates is determined by

$$x=(i+0.5)l, \quad y=(j+0.5)l, \quad z=(k+0.5)l \tag{3.6}$$

where i, j, and k represent the indices in the three-dimensional memory array of the lattice site and l is the distance between neighboring atoms, typically the bond length. The addition of the 0.5 term facilitates the centering of the lattice within the simulation box with periodic boundary conditions. In the implementation of these mappings, the indices range from negative to positive values so that the center of the simulation box is at (0,0,0). This treatment requires the indices referencing an actual memory array to be shifted since only non-negative values are permitted by C++.

For some lattice geometries, including the diamond lattice, there are two sets of mappings, one for "even" lattice sites and the other for "odd" lattice sites. The "odd" and "even" attributes alternate when progressing between neighboring lattice sites. For the diamond lattice, the memory array mappings are

$$\begin{array}{ll} (1,0,0),\ (-1,0,0),\ (0,\ 1,0),\ (0,0,\ 1) & \text{even} \\ (1,0,0),\ (-1,0,0),\ (0,-1,0),\ (0,0,-1) & \text{odd} \end{array} \tag{3.7}$$

These mappings are just one valid set for diamond lattices. Using different mappings will change the orientation of the lattice to the simulation box. The lattice site to coordinate transformation was determined by correlating the diamond lattice memory array mappings to a set of geometric coordinate neighbor mappings,

$$\begin{array}{ll} <1,\ 1,\ 1>,\ <1,-1,-1>,\ <-1,\ 1,-1>,\ <-1,-1,\ 1> & \text{even} \\ <1,\ 1,-1>,\ <1,-1,\ 1>,\ <-1,\ 1,\ 1>,\ <-1,-1,-1> & \text{odd} \end{array} \tag{3.8}$$

and extracting the relationships manually, resulting in

$$\begin{aligned} x &= \begin{cases} (2(i+k)-0.5)\dfrac{l}{\sqrt{3}} & i+j+k=odd \\ (2(i+k)+0.5)\dfrac{l}{\sqrt{3}} & i+j+k=even \end{cases} \\ y &= ((-i+j+k)+0.5)\frac{l}{\sqrt{3}} \\ z &= ((-i-j+k)+0.5)\frac{l}{\sqrt{3}} \end{aligned} \tag{3.9}$$

This manual process entailed the creation of a simple program to find valid relationships. The program used a brute force method to find out which associations between the memory and geometric mappings correctly identified connectivity loops. Again, there are different valid geometric coordinate transformations for the diamond lattice, each resulting in different lattice orientations with regards to the simulation cell. With the lattice-to-memory and lattice-to-coordinate mappings, the complete lattice can be constructed.

These mappings permit the lattice sites to be defined, but the set of valid lattice sites that would comprise a system lattice with periodic boundary conditions must be determined. A lattice site on one edge of the simulation box must have a valid neighbor

on the opposing side of the simulation box. The lattice is complete when all the lattice sites are defined within the boundaries of the simulation box and all of the lattice sites' neighbors are valid and assigned.

Polymer Chain Generation

One of the most difficult implementation issues to resolve was the completion of a preliminary chain or segment where the end point is specified as an existing atom. An advantage of the method presented here is that it accounts for energies and side atoms in order to generate a realistic configuration. This aspect essentially drives the growth or chains and segments away from other atoms. However, completing a chain or segment at a specific end point where an atom already exists at the end point is in opposition to the normal generation algorithm. As such, algorithms are employed that monitor the distance between the growing segment and the end point. Once this distance falls below a specified threshold distance, the algorithm walks all of the possible paths containing fewer than a specified number of hops. If one of these paths leads to the end point, it is selected. While this method has proven successful in completing segments within a reasonable time frame, the selection of the path generally ignores the selection criteria other than lowest-energy for the atoms in the path. Any path that is found to create energies above a specified threshold is excluded. Additionally, while finding a path, if two neighboring lattice sites to the last lattice site on the path are equidistant from the endpoint, the algorithm will use the RIS criterion in the selection process. By not accounting for all of the criteria, some control over the final structure is lost. This problem can be mitigated by creating larger segments, which would have the effect of

reducing the overall percentage of atoms in a chain that were selected along the final completion path.

Polymer Assembly Generation

The theory behind generating an assembly of polymer chains is relatively straightforward. However, in practice the algorithms required to generate the entire assembly in an efficient manner are more complex. A robust algorithm entails the selection of the chain that requires the addition of the maximum number of atoms, which is typically the shortest chain. A segment is inserted into this selected chain. If this chain still requires a lager number of atoms compared to the other chains, then an additional segment will be inserted. Otherwise, another chain that now requires the most atoms will be selected. This process ensures a uniform growth of all of the chains so that they are all finished at nearly the same time. Other methods such as randomly selecting a chain from the pool of available chains or sequentially selecting chains tend to leave a few chains that require a substantial amount of additional atoms after all of the other molecules have been generated and the system has become dense. The probability of adding enough atoms to these remaining chains then becomes low, and the computational expense becomes high. Completing the addition of all of the atoms at a similar rate improves the speed at which the entire system is generated.

As the system becomes dense, there are times when randomly selecting a position and length of segment to be removed does not permit a longer segment to be inserted within a reasonable timeframe. After a certain number of attempts, the algorithm steps through each position on the existing chain and attempts to insert a new segment at this

position. This stepping algorithm can be repeated after removing segments with different lengths until an insertion is successful.

In some cases, even this stepping algorithm is not successful in finding a place to insert a segment. This condition is usually a result of the molecule being completely surrounded by occupied sites. For further improvement another routine can be used that steps through all of the molecules in the system with the objective that the replacement of existing segments of these chains with the newly inserted segments would move one of the neighboring molecules away from the molecule of interest, creating an area for growth. By limiting the length of the inserted segments to be identical to the length of the segments removed in a molecule, the neighboring molecules can have their configurations modified, but not the number of atoms in the molecule. This constraint prevents the neighboring chains from being completed while trying to make room for the addition of atoms into the shortest chain.

Network Generation

In this implementation with polyethylene on a diamond lattice, the number of cross-links and dangling ends are determined by the number of molecules to be generated in the network. The number of molecular ends assigned to each cross-link depends on the functionality of the cross-linker and is set equal to four in this case. Thus, the integer component of two times the number of molecules divided by four is the number of cross-links that needs to be created. The remainder of this division is the number of dangling ends. For example, a network consisting of nine molecules would have four cross-links and two dangling ends. For networks with a low number of molecules, a molecule could

begin and end at the same cross-link forming a loop or more than one molecule could connect the same pair of cross-links. Once the number of cross-links and dangling ends is determined, the locations of these entities are randomly chosen. The connectivity is assigned based on shortest distances between the cross-link and dangling end locations. A sample connectivity for the nine molecule example is given in Table 3.5.

Table 3.5 An example assignment of cross-link and dangling end sites for nine molecules.

End Point	Connecting Sites			
Cross-link 1	Cross-link 2	Cross-link 3	Cross-link 4	Dangling End 5
Cross-link 2	Cross-link 1	Cross-link 3	Cross-link 4	Cross-link 4
Cross-link 3	Cross-link 1	Cross-link 2	Cross-link 4	Dangling End 6
Cross-link 4	Cross-link 1	Cross-link 2	Cross-link 2	Cross-link 3
Dangling End 5	Cross-link 1			
Dangling End 6	Cross-link 3			

In order to create networks of chains with predefined end-to-end lengths, the distance between connected cross-links must be controlled. In this implementation, the initial positions of the cross-links and dangling ends are randomly positioned as described earlier. The distance between these points are modified using pair potentials. The Lennard-Jones potential is calculated for each pair of points connected by a chain. Forces on each point can then be determined from the gradient of the potential. Additionally, pair potentials with only the repulsion portion enabled between each non-chain linked pair can be implemented to disperse cross-links and prevent clustering that would increase the difficulty of successfully generating the chains as discussed later. The final forces can then be used to perturb the points on the lattice until the "lowest energy"

configuration is found. Due to the discrete nature of the lattice, a unique algorithm was devised to efficiently find the lowest energy state. Once all of the force components on each point have been determined from all of the chain pair and non-chain pair potentials, the position of every point is moved to the lattice site that is closest to the direction of the force vector on that point. Once all of the points have been moved, the new energy is determined. Since the overall lowest energy may be achieved by only moving a portion of the points, the perturbation is repeated, but the atom with the lowest magnitude of force is excluded from movement. The energy of this new state is then determined. The perturbation step is continued, removing the atom with the next lowest force until only one atom is actually moved. Then the perturbation that resulted in the lowest energy is selected. New forces are calculated on this new configuration. This process is repeated until a lower energy configuration can not be found. To prevent a local energy minimum to be selected where the end-to-end lengths are not at the desired values, the algorithm further perturbs the configuration to move it out of the local energy well. This method has been found to be very efficient in finding configurations with end-to-end lengths that are within one bond length of the desired distance, preventing clustering of the end points.

One issue that must be overcome when generating cross-linked networks is that the density around each cross-link becomes relatively high as more chains are connected to the cross-link, reducing the probability of another growing chain to actually reach the cross-link. This is particularly problematic when trying to grow the final preliminary chain to a particular cross-link. This issue has been overcome by using a combination of ends-to-middle preliminary chain generation and sequential atom-by-atom chain

assembly growth. Instead of growing a preliminary chain from one end point to another endpoint as described earlier, the ends-to-middle preliminary chain generation creates a chain by adding atoms from both ends sequentially until they meet in the middle. Generating preliminary chains in full prior to generating subsequent preliminary chains using this method can still result in a lack of available paths for subsequent preliminary chains being generated from the cross-links since previously generated preliminary chains could coil around a cross-link completely surrounding the cross-link with its atoms. Growing all of the preliminary chains simultaneously by adding a single atom to each of the chain's end points in a sequential manner permits all of the initial chains to find paths from the cross-links.

For large systems, the likelihood of the growth of chains to still be trapped near a cross-link increases. Two additional modifications were made to help alleviate this problem. First an additional criterion, the furthest-distance criterion, was added. This criterion is similar to the closest-distance criterion, except the furthest distance has a higher probability of being selected. Including this criterion at the beginning of the chain growth with the distance reference point set to the cross-link that the chain is originating from encourages the growth to be directed away from the cross-link, reducing the likelihood of it interfering with the growth of other chains emanating from the same cross-link. The second modification is that instead of discarding an entire chain if its growth can not continue; only the last half of the chain is discarded. This modification prevents the atoms nearest the originating cross-link to be discarded, decreasing the likelihood of the chain being trapped near the cross-link.

Effectiveness of the Method

A polymer system with 50 molecules consisting of 1,000 atom molecules was created as a test case. A diamond lattice, as described earlier, was used with neighboring lattice points separated by the equilibrium bond length, 1.53 Å. The simulation box dimensions were calculated to give a density of 0.91 g/cm^3, assuming each unified atom represents a CH_2 structure with an atomic weight of 14.027 g/mol. To apply periodic boundary conditions, the lattice requires discrete dimensions for symmetry, which makes it difficult to precisely define the number of molecules, number of atoms per molecule, and overall density. Due to these limitations, the actual final density was 0.90 g/cm^3. The end points of these preliminary configurations were determined by selecting a random point and then growing the initial chain until the characteristic length of the molecule ($\langle r^2 \rangle = N\, C_{inf}\, l^2$) was reached, where $C_{inf} = 6.7$. Again the accuracy of this distance is limited by the discrete nature of the lattice. The RIS probabilities for polyethylene are given by Sharaf et al. (2001) as previously listed in Table 3.3. Since the bond length and angle energies are already minimized by use of the diamond lattice and the RIS criterion should minimize the dihedral energies to some extent, only the van der Waals energies need to be considered for the lowest-energy criterion. The energies for the Lennard-Jones potential determined by Equation 2.4 were used. The weighting factors used for both the initial chain growth and the atom insertion phases are shown in Table 3.6.

Table 3.6 Weight factors employed in the initial configuration generation.

Criterion	Initial Growth Weight	Insertion Weight
Closest-to-End	0.0	0.2
Least-Dense	0.0	0.1
Lowest-Energy	0.2	0.1
RIS	0.8	0.6

Full volume exclusion was used, including volume exclusion of the neighboring side sites that would be occupied by hydrogen atoms. Placement of the 50,000 atom lattice takes less than a couple of hours on a single processor, 2.2GHz AMD Opteron based computer. Over 90% of the atoms are placed within 30 minutes. The calculation of the lattice densities and energies consumes a significant portion of this time.

For comparison purposes, another configuration was created using the method of generating a polymer system at a low density and then compressing it to the desired density (van der Vegt et al. 1996). A system of 50 molecules consisting of 1,000 atoms was generated on a diamond lattice at a density of one eighth of the desired density, 0.114 g/cm^3. The same weight factors were used. Due to the low density, the configuration was generated in a few minutes. The low density configuration was gradually compressed to the same dimensions as the initial configuration created with the new method by running an MD simulation with a non-equilibrium NPT ensemble (Melchionna et al. 1993) over a simulation time of 500 ps with an integration step size of 0.5 fs and at a temperature of 300 K. All of the potentials were enabled, except the cut-off distance for the van der Waals potential was reduced to 4.01 Å to eliminate the attractive portion of the potential (van der Vegt et al. 1996). The full cut-off distance of 10.0 Å was reinstated for the remaining MD simulation steps. The compression process

took three hours to complete when run on a computer cluster using 12 2.2GHz AMD Opteron processors.

After the initial configurations were generated, they were relaxed to determine how much they changed from their initial states. The MD simulation was run with a non-equilibrium NPT ensemble holding the pressures at 1 atm for 250 ps with an integration step size of 1.0 fs and at a temperature of 300 K. The less the change as a result of relaxation, the better the initial configuration can be considered.

The low density/compression method was previously found to generate configurations with low energies (van der Vegt et al. 1996). The results from the relaxation simulations confirm this observation and show that the new method generated configurations with the same energies, which are at near equilibrium within 40 ps (Figure 3.15). There are some initial changes to the energies in the first few picoseconds due to the diamond lattice constraints with the present method, and with the increase of the cut-off distance for the van der Waals potential with the low density/compression method. If the new method did not include the volume exclusion of the hydrogen side atoms or the lowest-energy criterion, the van der Waals energies would be many orders of magnitudes higher, requiring significantly longer relaxation times.

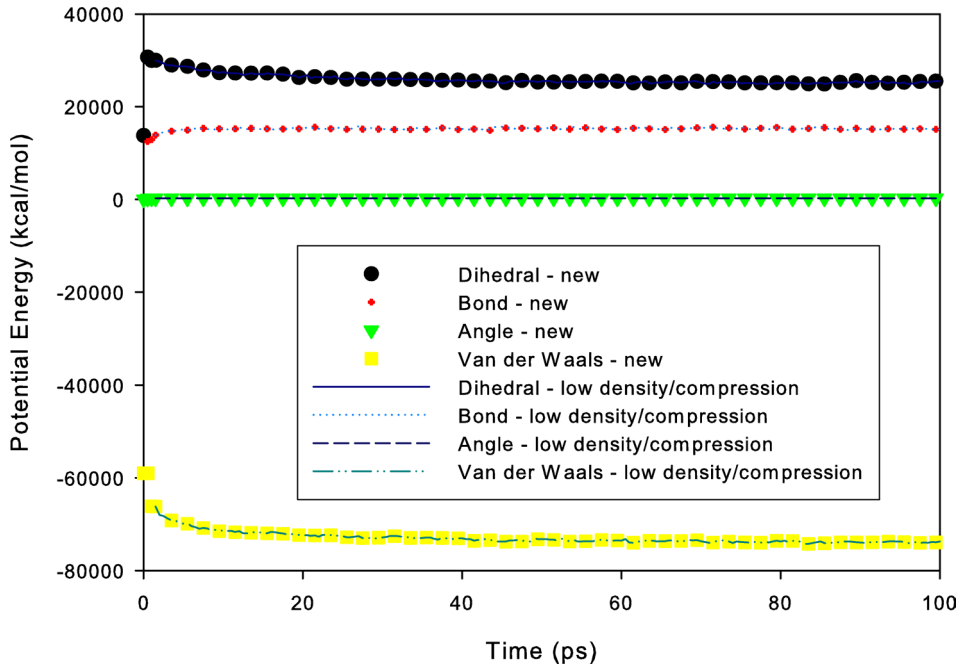

Figure 3.15 System energies during relaxation process.

The change of volume during the relaxation process gives an indication of how well dispersed the polymer molecules are and how well the potentials employed mimic actual behavior. As with the energy results, there is an initial jump in volume which is quickly relaxed to a volume very close to the initial volume of the simulation cell (Figure 3.16).

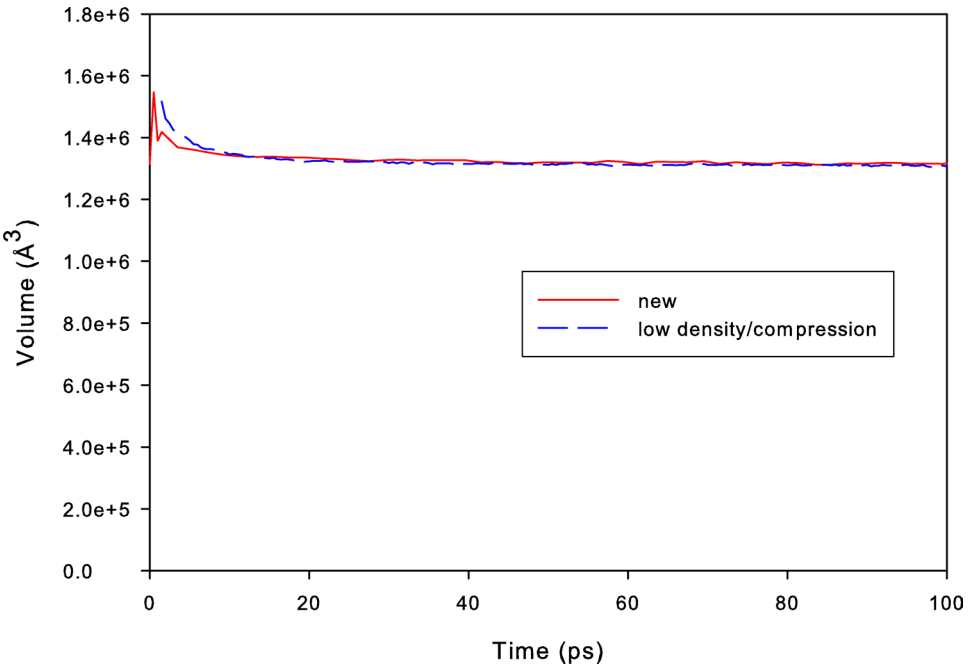

Figure 3.16 Change of volume during relaxation.

The minimal change of energy and volume indicate that both the new and the low density/compression methods generate very good initial configurations based on overall system properties. Tracking the changes in RIS percentages, average end-to-end length, and average radius of gyration during the relaxation process gives a good understanding of how much the individual molecules change as they relax into individual lower energy states. The evolution of the percentages of *trans*, *gauche*$^+$, and *gauche*$^-$ states indicates that the initial configuration does not create enough *trans* states (Figure 3.17). For both methods the initial percentage of *trans* states is lower than the target value of 65% (Sharaf et al. 2001) during generation. The lower percentage of *trans* states is likely due to a difference in the RIS probabilities used in this method and the probabilities of these states resulting from the PYS potentials. Additionally, the lower percentage of *trans* states with the new method is due to the closest-to-end, lowest-energy, and least-dense

criteria. These criteria weaken the strength of the RIS criterion. Increasing the *trans* probabilities in the RIS criterion could help compensate for the lower number of *trans* states. The configuration generated by the low density/compression method has a lower percentage of *trans* states as a result of the compression process reducing the number of "straight" *trans* states and increasing the number of "bent" *gauche* states. Increasing the compression time would likely reduce this effect of this problem, but would increase the computational time.

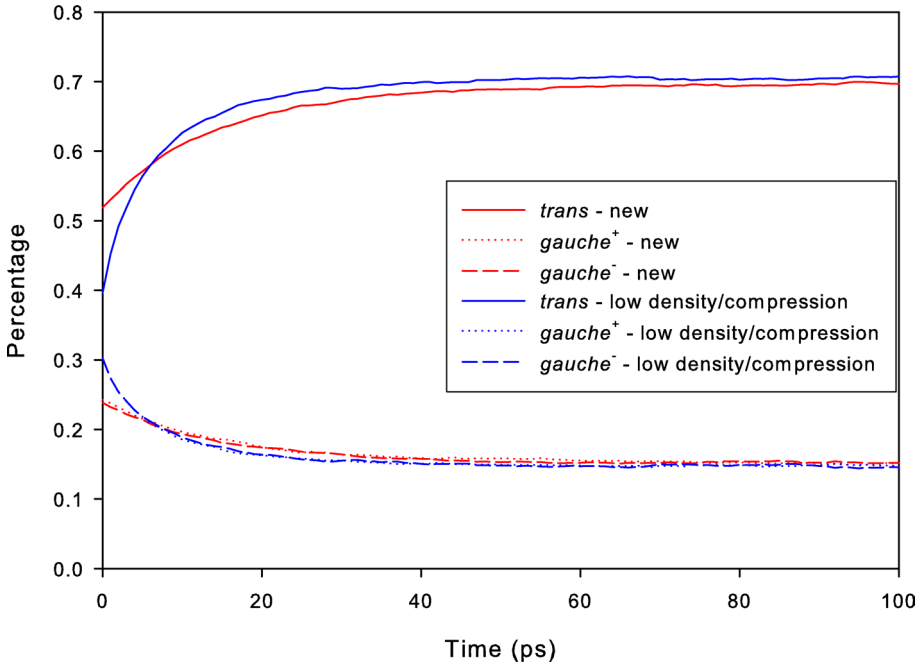

Figure 3.17 Change of trans and gauche percentages during relaxation.

The average end-to-end length (Figure 3.18) and average radius of gyration (Figure 3.19) graphs demonstrate the significant differences in the configurations generated by these two methods. Initially, the molecules generated by both methods have statistically correct end-to-length and radius of gyration. However, the compression step

in the low density/compression method reduces the values of these properties. The lack of apparent change over a time span of 250 ps indicates that the process of returning to the most probable end-to-end length and radius of gyration values is well outside of the timeframe permissible by typical MD simulations.

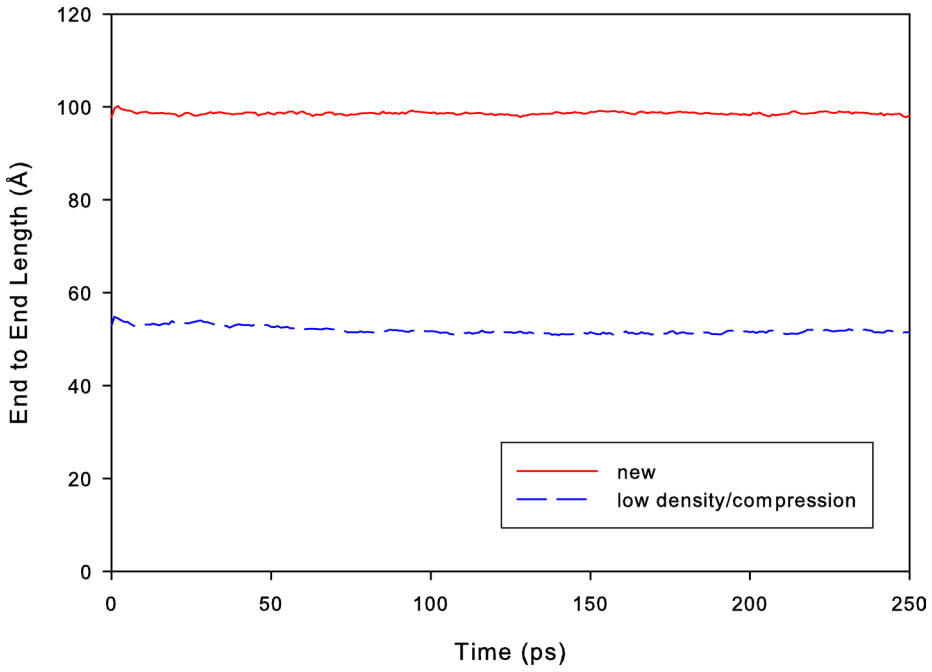

Figure 3.18 Change of average end-to-end length during relaxation.

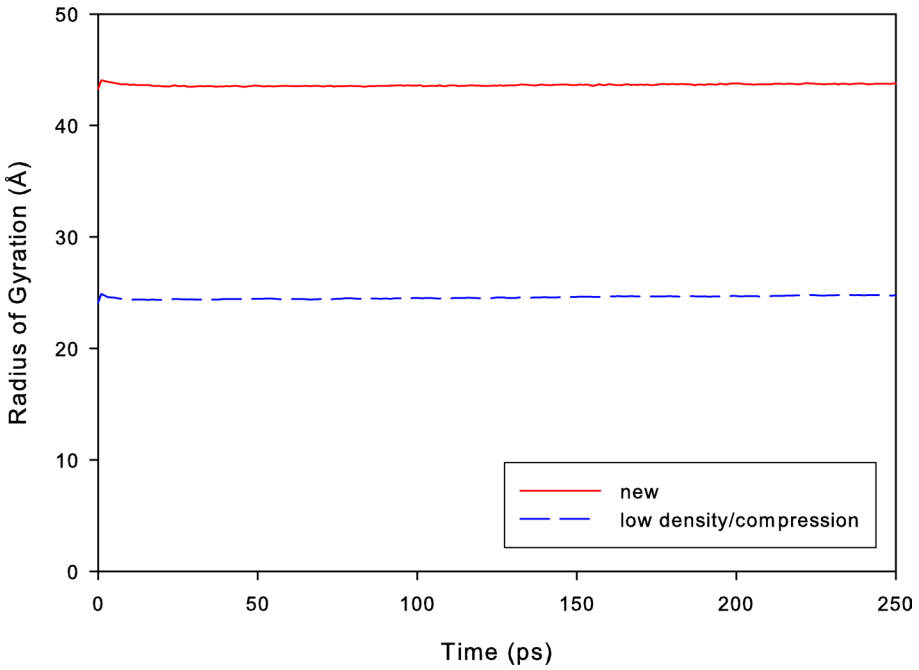

Figure 3.19 Change of average radius of gyration during relaxation.

The effect of the two methods can be further elucidated by examining the geometric changes of a molecule during the relaxation process. A molecule extracted from the initial configuration created with the new method is given in Figure 3.20 and a molecule extracted from the initial configuration created with the low density/compression method is given in Figure 3.21. These representative molecule structures demonstrate that the low density/compression method generates less realistic "balled up" configurations having little entanglement with neighboring molecules while the new method generates more realistic, spread out molecules that permit much more interaction with neighboring molecules.

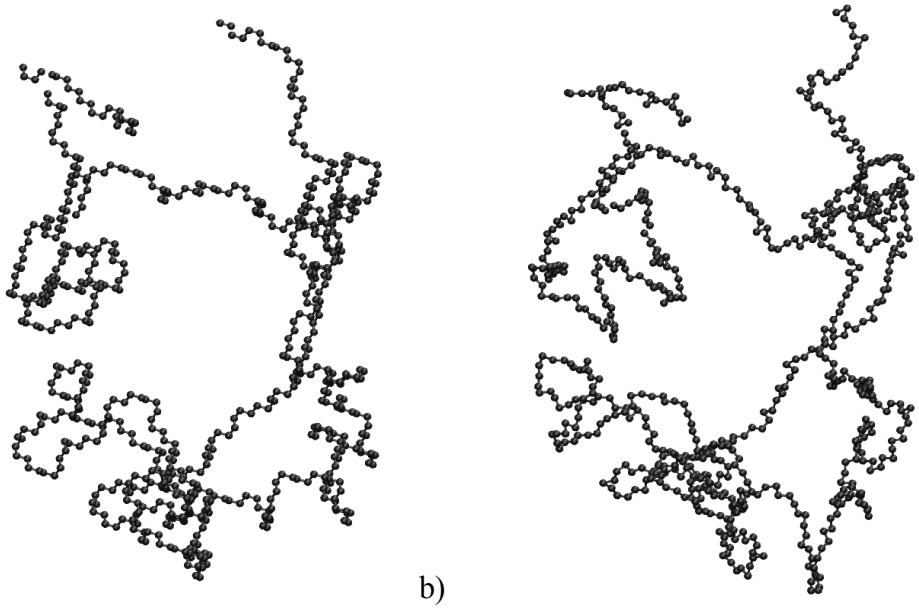

a) b)

Figure 3.20 Change in geometry of a sample molecule from the system created with the new method from the initial configuration, a, to the relaxed configuration, b.

a) b)

Figure 3.21 Change in geometry of a sample molecule from the system created with the least dense/compression method from the initial configuration, a, to the relaxed configuration, b.

Conclusions

The method presented here is a significant improvement to the Faulon et al. method (Faulon et al. 1997; Faulon 2001), permitting the creation of realistic polymer configurations at high densities with low energies while maintaining a significant degree of control over the final properties of the system. The control over the relaxed configuration and the relatively low amount of computational time required to reach the relaxed state are advantages over other methods. In addition to being able to control the statistical properties of the molecules, specifying the endpoints of every molecule permits the orientation distribution of the polymer system to be controlled. Complex molecular configurations such as cross-linked networks, ring polymers, and branched polymers can also be generated with specified properties.

While the low density/compression method was found to generate configurations that provide reasonable results in small molecule diffusion simulations (van der Vegt et al. 1996), these configurations would not likely do as well in mechanical simulations where molecular entanglement would be important. The new method presented here should provide initial structures with more realistic behavior during MD simulations of deformation processes. The molecular assembly generation methods presented here have advantages over the Faulon et al. method on which it was based. RIS characteristics can be specified and energies can be minimized as a result of the implementation of probability tables, particularly the RIS and lowest-energy criteria. This new method entails the removal of multiple bonds at the point where a longer segment is inserted, while the Faulon et al. method entails the removal of a single bond. Removing more than

a single bond during the insertion stage probably increases the amount of entanglement between molecules, though this has not been evaluated.

This new method takes much less computational time than the low density/compression method, but significantly more time than the Faulon et al. method. The increased computational time over the Faulon et al. method is a result of the more complex molecule growth algorithms. Eliminating some of the criteria such as the lowest-energy or least-dense criteria significantly decreases the computational time required. The implementation of the new method presented here was programmed for correctness and the algorithms have not been optimized for efficiency. Additionally, the program is currently single-threaded and does not take advantage of multi-processor environments. It is likely that the computational time can be reduced significantly after profiling and optimizing the code. The majority of computational time is spent placing the last few percent of the atoms. Therefore generating an initial configuration at around 90% of the desired density with the new method and then compressing it to the final density may give better performance and still result in good control of the relaxed structure.

Though a relatively simple polyethylene molecule was generated here, generating more complex molecules can easily be implemented by either adding specific atoms and side groups in the order found along the backbone, or having each atom on the lattice represent an entire monomer. After the initial configuration is generated, the atoms can be replaced with the appropriate monomer structure for MD simulations. The type of lattice chosen will have a direct bearing on the accuracy of more complex molecules to their relaxed state. If the bond lengths are different between backbone atoms, the

magnitudes of the bond length energies in the initial configuration will be higher than in the relaxed configuration. Likewise, the angles between lattice sites will directly affect the bond angle and dihedral energies. An advantage of the new method presented here is that different lattices can be compared with little effort.

Further evaluation needs to be performed to better understand the differences in mechanical and other relevant behaviors of the initial structures generated with this method. However, the evaluation presented here indicates that this method might be expected generate much more realistic configurations than any other method presented in the literature.

CHAPTER 4

TIME ACCELERATION OF MOLECULAR DYNAMICS

Background

Simulating polymer deformation processes with atomistic models can permit the prediction of mechanical behaviors based on first principles. However, the permissible time scales for atomistic simulations preclude accurate predictions of events that take place at slow rates and at long times typical of real world applications. This limitation is particularly problematic for this research since the mechanical behavior of many polymers has significant rate dependencies. Molecular dynamics (MD) allows reasonably large atomistic systems to be studied, on the order of tens to hundreds of thousands of atoms. Due to current and foreseeable computational limitations, MD simulations are limited by the length of time that can be modeled per number of atoms. Since traditional MD requires integration time steps on the order of the vibrational frequencies of the atoms in the simulation, e.g. 10^{-14}s, simulations of polymer systems are usually limited to the nanosecond range. Deformation in many forming processes such as bottle and film blowing, fiber spinning, and film drawing takes place in millisecond or longer timeframes, requiring many orders of magnitude longer MD simulations than can be currently performed. To increase the timescales of MD simulations many techniques have been employed to reduce the degrees of freedom in the system such as the use of united atoms, periodic boundary conditions, and cut-off distances. However, these methods do not permit enough of an increase of the timescale.

Another approach is to neglect the vibrational detail and focus on the more significant, less frequent events that affect the mechanical performance. The dihedral rotation of polymer chains about the bonds is the primary mechanism influencing deformation. Due to the presence of other atoms and side chains in close proximity to the group of atoms undergoing a dihedral rotation, the barriers to rotation are significant enough to reduce the rate of rotational transitions to several orders of magnitude lower than the vibrational rates. Therefore, methods that focus on the less frequent conformational changes instead of the vibrational changes might be able to increase the timescales accessible through MD by several orders of magnitude.

Several methods have been presented for time accelerating methods to capture the long term events while maintaining reasonable detail of short term events (Voter et al. 2002). Transition State Theory (TST) is the basis for most of the time accelerating methods. TST is based on the assumption that there are several energy minima or states that an entity (atom, segment, or system) can independently transition between (Figure 4.1).

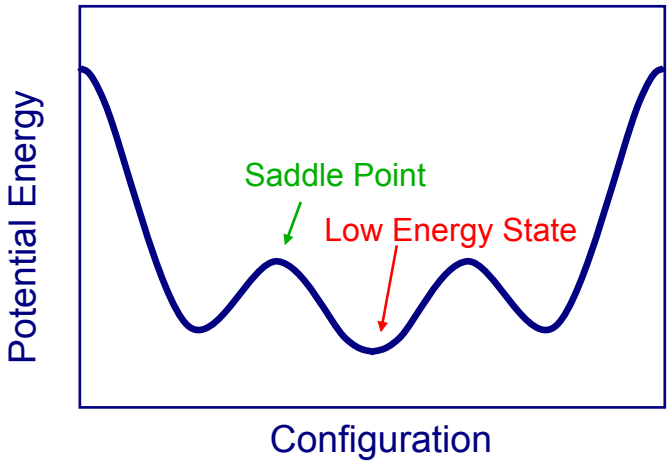

Figure 4.1 Diagram showing the primary features of a potential energy related to transition state theory.

The entity resides in a particular state, on average, for a specific time. This time is inversely related to the rate constant for the transition. Making the assumption that the vibrations are harmonic, the rate constant can be defined as

$$k_{A\rightarrow}^{HTST} = v_0 \exp\left[\frac{-E_a}{k_B T}\right], \tag{4.1}$$

where $k_{A\rightarrow}^{HTST}$ the harmonic transition state theory constant, v_0 is the ratio of the normal mode frequencies at the minimum energy points to the normal mode frequencies at the transition points, E_a is the activation energy of the transition, k_B is the Boltzmann's constant, and T is the absolute temperature. This rate constant can be used in kinetic Monte Carlo (kMC) simulations to direct the probability of a state change event occurring. One of the primary limitations of TST in MC simulations is that all relevant transitions must be known a priori, a limitation not inherent to classical MD. Additionally, only independent events are addressed, excluding cases for which a transition is quickly followed by a return transition or an even number of back-and-forth

transitions that do not result in a net change in state. Also, multiple changes in state may be required prior to achieving a stable state. To address the need for defining all relevant transition states before starting a MC simulation, the self learning or on-the-fly kMC method was developed (Henkelman and Jonsson 2001). This method attempts to determine all of the saddle points on the potential energy surface between states using the dimer method (Henkelman and Jonsson 1999). From the saddle point energies, the transition rates can be determined and are then implemented into the kMC method. While this permits significant acceleration, the dimer search must be performed after each transition. With the large number of bond rotations occurring in a large polymer system, this method would require too much computational overhead to be useful.

Somewhat similar to the on-the-fly kMC is the Temperature Accelerated Dynamics (TAD) method (Sorensen and Voter 2000). TAD relies on higher temperatures increasing the rate at which transitions occur. Increasing the temperature alone is not sufficient as transitions with different saddle point energies would have their transition rates increased by different amounts. TAD compensates for the difference in relative transition rates between the various types of transitions in the system. A MD simulation is run at a higher temperature than the desired simulation temperature until a transition occurs. The nudged elastic band method (Henkelman and Jonsson 2000) is used to determine the saddle point of that transition. The time to this initial transition is noted and the transition is reflected back to its previous state. The MD simulation is continued for a specific period of time based on the value of the saddle point energy of this first transition. This additional time is required to find other transitions that may occur in shorter time periods at lower temperatures. Subsequent transitions are recorded

and reflected back as was done with the initial transition. After the pre-determined period of time has been completed, the lowest energy transition is accepted. The time to the lowest energy transition is mapped back to the lower temperature and the simulation time is increased by the low temperature time, i.e.,

$$t_{low} = t_{high} \exp\left[E_a \left(\frac{1}{k_B T_{low}} - \frac{1}{k_B T_{high}} \right) \right]. \tag{4.2}$$

Here, t_{low} is the equivalent low temperature time, t_{high} is the high temperature simulation time, E_a is the activation energy of the transition, T_{low} is the desired low temperature, and T_{high} is the high temperature of the simulation. The greater the ratio of the higher temperature to the lower temperature, the greater the speedup. However, higher temperatures result in an increased number of transition events, including more correlated events. These additional transition events reduce the accuracy of the underlying assumptions in this method. Therefore, the high temperature should be chosen to be as low as possible and still meet the desired acceleration goals. This method makes more approximations than the previously discussed methods, but as long as too high of a temperature is not used, the results can be accurate with a time acceleration factor on the order of thousands for small molecular systems. The calculations required to find the saddle point scale between the number of atoms in the system, N_{atoms}, and N_{atoms}^2, so for large systems, these calculations can take away any gain from the time acceleration.

The parallel replica method for both MC (Swendsen and Wang 1986) and MD (Hukushima and Nemoto 1996; Voter 1998) simulations permits the temporal decomposition of a simulation so that the time can be parallelized over multiple processors in a similar manner as the more typically used spatial decomposition. In this

method, the system is replicated on multiple processors. The atomic velocities for each replica are randomized so that each replica has the same configuration but separate dynamics. All of the replicas are then run independently until a state change occurs in one of the replicas. At this point, all of the replica simulations are halted except for the one in which the state change occurred. This replica is then run for a little longer to ensure that the state does not revert back. If the state change is still valid, the overall simulated time is increased by the sum of the simulated times for each of the replicas. Then the replica in which the state change occurred replaces all of the other replicas, the dynamics are randomized, and the process is repeated. This method works well for small systems for which spatial decomposition is not highly parallelizable. Though this method has been applied to small polymer systems (Halley and Duan 2002), it has little appeal in this research since the polymer systems of interest are generally quite large and can be spatially parallelized more efficiently. Additionally, dihedral transitions occur at some point in the system at every time step which would make this method impractical. The parallel replica method can also be combined with other time acceleration methods.

Another approach to accelerate MD is to modify the system potential surface in order to increase the rate at which infrequent events occur (Grimmelmann et al. 1981). This approach entails increasing the potential energy in the wells between transition saddle points to reduce the amount of additional energy required to cross over these saddle points, thereby increasing the frequency at which transitions occur. The modifications to the potential energy surface must be made in a manner that ensures that the energies at the saddle points are unmodified; otherwise, the rates of each transition

will be affected differently, possibly leading to unrealistic behaviors. Since the potential energy "wells" are increased, vibrational detail is lost.

Grubmuller (1995) proposed a conformational flooding method to speed up simulation of macromolecules, particularly proteins. A short MD simulation is run to reduce the degrees of freedom in the conformational space by calculating a conformational space density model. This coarse grain conformational space model is then used to calculate a flooding potential which is then applied to the system Hamiltonian. The flooding potential essentially fills in the potential energy wells in the system potential. While this method yielded good accelerations for the very small protein that was evaluated, the computational cost of calculating the system Hamiltonian would overcome the acceleration gains for large systems of interest in this research.

Voter (1997b; 1997a) proposed the hyperdynamics method which adds a bias potential to the system potential energy surface. This bias potential approaches zero near saddle points to maintain the correct saddle point energies. The bias potential is based on the Hessian matrix of the second derivatives of the potential energy with respect to the atomic positions. This approach does not require knowledge of the system potentials prior to the simulation. Near the saddle point, the lowest eigenvalue of the Hessian will become negative. Therefore, the bias potential is defined such that it approaches zero as the lowest eigenvalue becomes negative. While this method provides a general solution, the calculations of the system Hessian result in large systems becomes too computationally expensive. Calculating the Hessian of only neighboring atoms to the atom of interest can help this method scale computationally for larger systems (Gong and Wilkins 1999; Duan and Gong 2003). However, larger systems are more likely to

produce a negative lowest eigenvalue value away from the transition, reducing the effectiveness of the method. This issue was noticed even on a system with only nine moving atoms (Voter 1997b) during an Ni adatom diffusion simulation.

Voter later proposed a modification that only requires the first derivative of the potential energy to be computed which is already required in normal MD operations (Voter 1997a). This method requires only tens of calls to the force routines of the MD software, though some knowledge of the potential is required in order to implement optimal parameters for the bias potential. As long as the increase in rate is more than around 30, a net gain will be realized. However, this method is applied to the entire system, where state transitions are separated by relatively large time spans.

Another bias potential has been described by Steiner et al. (1998) which sets a minimum or floor energy and has the benefits of being easier to code and computationally inexpensive. Basically, wherever the potential energy falls below the floor energy, it is simply assigned the floor energy (Figure 4.2). To maintain continuity in the modified potential, a blending function is implemented. The higher the floor is set, the better the time scaling. However, the floor must be set lower than the lowest saddle point or transitions that depend on the lowest saddle point will be lost. As a result, this method can become ineffective for systems with a large number of states as the probability for a state to lie below the floor energy becomes more likely (Voter 1997b).

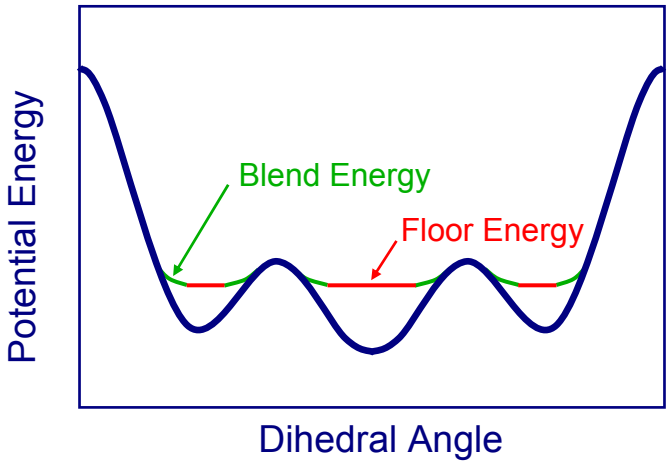

Figure 4.2 Diagram showing a boost potential with the floor energy in red and the blending energy in green.

A similar approach is followed by Pal and Fichthorn (1999) where the potential below a threshold value is increased but, instead of adding a bias potential, the base potential is multiplied by a boost function. The boost must be equal to unity in the saddle point regions so as not to affect the relative rates of transitions. Their boost function includes two parameters that permit the 'aggressiveness' of the boost to be adjusted. However, this boost function can produce modified potentials with small energy wells within the region to be boosted, though they are not believed to have a significant effect on the final impact of the boost function as was demonstrated with their Ag adatom diffusion simulations.

Both this approach by Pal and Ficthorn and the simple bias potential by Steiner et al. are less effective for large systems in which the transitions tend to get overpowered by the fluctuations in the potential energies within large systems. Wang et al. (2001) overcome this small system limitation by basing the boost potential on the potentials of each atom for simulations of the diffusion of Lennard-Jones atoms on a fcc surfaces.

Two forms of this local boost method are presented. The first is based on the maximum potential of all the atoms in the system, i.e.,

$$\Delta V_b(\mathbf{r}) = V_{\max}(\mathbf{r})\left(\frac{\Theta(\Delta V) f(\Delta V)}{1+\Theta(\Delta V) f(\Delta V)}\right) \tag{4.3}$$

where $\Delta V_b(\mathbf{r})$ is the boost potential, $\mathbf{r}$ represents the positional degrees of freedom for all of the atoms, $V_{max}(\mathbf{r})$ is the largest potential energy of all of the atoms in the system in the configuration defined by $\mathbf{r}$, $\Theta(\Delta V)$ is a stepping function which is 1 if ΔV is greater than zero and 0 otherwise, $f(\Delta V)$ is a blending function to ensure continuity, and ΔV is the difference between the floor energy, V_{floor}, and $V_{max}(\mathbf{r})$, given by

$$\Delta V = V_{floor} - V_{max}(\mathbf{r}) . \tag{4.4}$$

The blending function is given as

$$f(\Delta V) = \frac{b_c \exp\left(-b_\gamma / \Delta V\right)}{1+\exp\left(-b_\gamma / \Delta V\right)}, \tag{4.5}$$

where b_c and b_γ are parameters that affect the shape of the blending curve. The other form of the local boost method is based on the minimum difference in energy between each atom's potential and the floor energy, i.e.,

$$\Delta V_b(\mathbf{r}) = \Delta V \Theta(\Delta V)\left(\frac{b_c (\Delta V)^{b_n}}{1+b_c (\Delta V)^{b_n}}\right), \tag{4.6}$$

where b_c and b_n are blending parameters. This second form has the advantage of requiring less computational resources as the blending function is simpler, especially if b_n is set to unity, and a search through all of the atoms in the system for the maximum potential energy is not required.

Wang et al. (2001) also propose using multiple cut-off energies to facilitate boosts in heterogeneous systems. As with the other bias and boost potential methods, when

multiple transitions occur simultaneously, the boost will be reduced by a factor of the number of atoms making the transition. Additionally, this method is intended for systems in which a single transition occurs at a time and the acceleration is only significant when a large percentage of the atoms are being boosted.

Miron and Fichthorn (2003) developed a method similar to hyperdynamics and the local boost method to study the surface diffusion on Cu surfaces. Their boost potential is based on geometric changes to the system instead of directly on the system potential energy surface. In their implementation, the bond length between two atoms is monitored. When the bond length is at or near its equilibrium point, the bias potential is large. As the bond is stretched away from the equilibrium point, the bias potential goes to zero. This method takes advantage of calculations already performed in normal MD simulations and therefore requires little computational overhead for small systems. However, once the atoms separate enough for a new state to be achieved, a conjugant gradient type of algorithm must be used to determine the equilibrium point of the new state for future calculations. For large systems with many potential transitions, the number of equilibrium calculations necessary to achieve good acceleration would be prohibitively high.

Systems for which low energy barriers separate small regions of high frequency transitions that are not of interest are not well accelerated with the bias and boost potential based methods, since there is no time acceleration when transitions are reached. To overcome this limitation, Miron and Fichthorn (2004) presented a method to bridge these adjacent low energy regions together with a bridge potential.

The primary challenge with implementing accelerated dynamics for large polymer systems is the number of transitions that either occurs or are about to occur simultaneously throughout the entire system. One of the premises of the hyperdynamics method is to boost the potential surface based on the configuration of the entire system of atoms. At any time that the configuration of the entire system approaches a transition point, the boost potential must approach zero, effectively eliminating any time acceleration at that time. In applications of the hyperdynamics method presented in the literature, small systems typically only traverse a few transitions and the transitions occur very infrequently; as a result, the hyperdynamics method is capable of significant time acceleration. In the case of the large polymer systems employed in this research, however, RIS transitions occur at a rate of about five per 1 fs time step. Since the system cannot be accelerated during a transition, the hyperdynamics method, and all others except for the parallel replica method, would result in no time acceleration. An intriguing question is whether a large polymer system can be broken down into enough smaller subsystems to enable significant acceleration for each subsystem. The boost factor for each of these subsystems could then be averaged to determine an effective system boost factor. This approach may circumvent the underlying assumption of the hyperdynamics method that the potential energy surface is only to be boosted when the configuration is far from a transition. The averaging of all of the subsystems will reduce the amount of acceleration possible with each subsystem. However, if the following approach is able to accelerate the system time and maintain the correct dynamics, the approach would be useful in either studying slower processes or reducing the computational requirements.

Method

The most direct method to accelerate the dynamics of a polymer system, also requiring the least amount of computational expense, is applying a boost potential to the dihedral potential. In this method, only the dihedral potential is modified. An advantage to this method is that the shape of the potential energy for each dihedral group is known and can be manipulated directly. Since the specifics of this potential are known, the maximum boost energy and blending function parameters that do not affect the transition regions of the potential can be determined prior to performing the simulation. The modifications to LAMMPS are also relatively minor and have an insignificant effect on the computational requirements. Only a few functions need to be added to calculate the magnitude of the boost potential for each dihedral group, the approximate magnitude of time acceleration, and the derivative of the boost potential with respect to the cosine of the dihedral angle which is used to account for the effect of the boost potential on the forces.

While any of the bias potentials discussed here could be used, the boost function presented by Wang et al. (2001) was found to be the least computationally expensive. The difference between the normal dihedral potential energy, $V_d(\phi_d)$, and the floor energy, V_{floor}, is determined for each dihedral group, i.e.,

$$\Delta V(\phi_d) = V_{floor} - V_d(\phi_d). \tag{4.7}$$

The boost potential for the dihedral group is then determined by,

$$\Delta V_b(\phi_d) = \Delta V(\phi_d)\,\Theta\left(\Delta V(\phi_d)\right)\left(\frac{b_c\left(\Delta V(\phi_d)\right)^{b_n}}{1+b_c\left(\Delta V(\phi_d)\right)^{b_n}}\right) \tag{4.8}$$

where b_c and b_n are the blending parameters. This form requires significantly less computational resources when $b_n = 1$. The forces on each atom are determined from the derivative of the potential energy, which for the dihedral potential is given by,

$$\frac{dV(\phi_d)}{d\cos\phi_d} = \sum_{i=1}^{3} nk_{i+1}\cos^{i-1}\phi_d \tag{4.9}$$

where k_i are the parameters of the dihedral potential defined in Chapter 2. In addition to the forces resulting from the dihedral potential, the additional effect of the boost potential on the atomic forces must also be accounted for, i.e.,

$$\frac{d\Delta V_b(\phi_d)}{d\cos\phi_d} = -\frac{d\Delta V(\phi_d)}{d\cos\phi_d}\left(\frac{b_c\left(\Delta V(\phi_d)\right)^{b_n}\left(b_n+1+b_c\left(\Delta V(\phi_d)\right)^{b_n}\right)}{\left(1+b_c\left(\Delta V(\phi_d)\right)^{b_n}\right)^2}\right). \tag{4.10}$$

Modifying the potential energy by adding the boost energy will accelerate the dynamics of the system. The magnitude of this acceleration needs to be determined at each time step in order to determine the amount of accelerated time during the integration step to maintain correct overall system dynamics, e.g. RIS transition rates and the rate at which the system is to be deformed for the uniaxial extension experiments. This time acceleration magnitude can be referred to as the boost factor which is determined at each time step as

$$boost\ factor = \left\langle \exp\left(\frac{\Delta V_b(\phi_d)}{k_B T}\right)\right\rangle_{V(\phi_d)}, \tag{4.11}$$

where $\langle\ \rangle_{V(\phi_d)}$ is the canonical ensemble average over the non-boosted potential energy surface. For a given measurable quantity, P, the canonical ensemble average is given by (Voter 1997b),

$$\langle P \rangle_{V(\mathbf{r})} = \frac{\iint P(\mathbf{r},\mathbf{p}) \exp\left[\frac{-K(\mathbf{p})}{k_B T}\right] \exp\left[\frac{-V(\mathbf{r})}{k_B T}\right] d\mathbf{r} d\mathbf{p}}{\iint \exp\left[\frac{-K(\mathbf{p})}{k_B T}\right] \exp\left[\frac{-V(\mathbf{r})}{k_B T}\right] d\mathbf{r} d\mathbf{p}} \tag{4.12}$$

where **p** is the momentum and K is the kinetic energy. Since the boost potential energy is independent of the momentum and the integrals can be approximated by considering the potential energies at each dihedral group within the system, the expression for the average boost per time step reduces to

$$boost\ factor = \frac{\sum_{i=1}^{N_d} \exp\left[\frac{\Delta V_{b_i}(\phi_d)}{k_B T}\right] \exp\left[\frac{-V_{b_i}(\phi_d)}{k_B T}\right]}{\sum_{i=1}^{N_d} \exp\left[\frac{-V_{b_i}(\phi_d)}{k_B T}\right]}, \tag{4.13}$$

where N_d is the total number of dihedrals in the system. The contribution to the potential energy from the bond length, bond angle, and non-bonded pair potentials needs to be determined for each dihedral group. For each of these potentials, the potential energy is calculated for each atom pair or triplet and then divided equally among these atoms. Summing the contributions from all of the potentials acting on an atom gives the overall potential energy for that atom. The overall potential energies of each atom in a dihedral group are summed and then added to the dihedral potential energy for that dihedral group to determine the overall potential energy for the dihedral group.

Each dihedral group is considered a separate sub-system. Since consecutive dihedral groups along the backbone of a polymer molecule overlap, this approach actually evaluates a system of overlapping sub-systems. While there are concerns as to the validity of averaging overlapping sub-systems, it will give the best case scenario in regards to the maximum amount of acceleration that is achievable by boosting the

dihedral potentials since this approach will result in the largest possible increase to the potential energy of the entire system.

Once implemented into LAMMPS, the boost factor was determined for a system of 50,000 atoms consisting of 50 molecules, each with 1,000 atoms that had already been relaxed using the methods described in Chapter 2. An accelerated MD simulation was run using a NPT ensemble with 1 atm pressure maintained on each face at 300 K. As the floor energy is increased, so is the boost factor (Figure 4.3). The initial spikes in the boost factors are a result of the previously relaxed system adjusting to the new boosted potentials. Initially, a large percentage of the dihedral states are in the potential energy wells below the floor energy. When the boost potential is first applied, this relatively large difference between the floor energy and the initially low potential energy state of the dihedral results in large boost factors. Once the bond, angle, dihedral, and non-bonded potential energies within the system reach equilibrium with the boost potentials, the boost factors stabilize at a reasonable level.

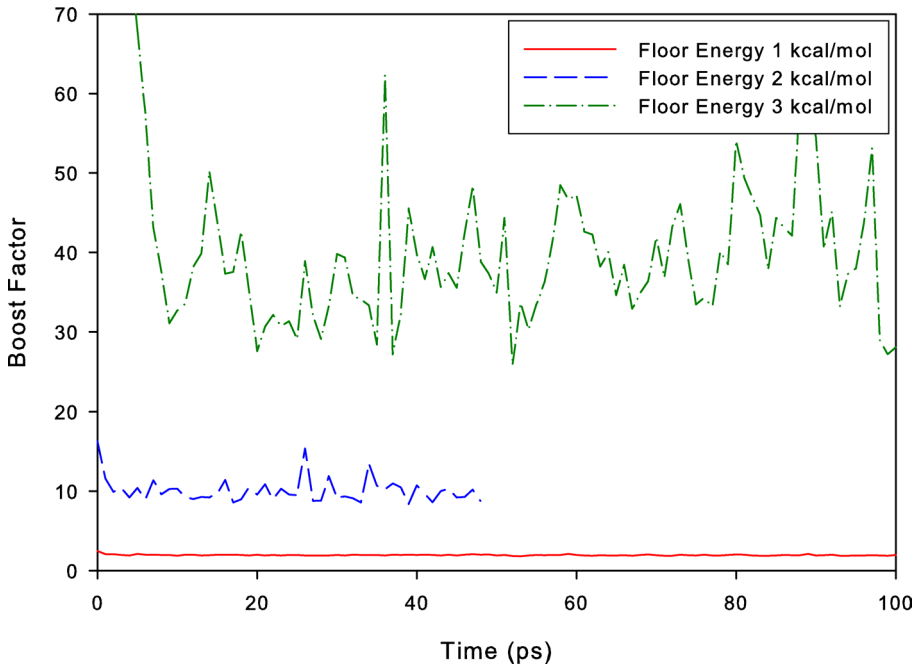

Figure 4.3 Boost factors during relaxation simulation of a polymer system consisting of 50 molecules each with 1000 unified atoms using dihedral boost potentials with different floor energies at a temperature of 300 K.

These boost factors, while not the several orders of magnitude achieved by other methods for systems having infrequent transition events as reported in the literature, could still quite useful for investigating a single order of magnitude slower processes and in reducing the computational expense of simulations if the method is valid over a wide range of simulations.

The behavior of the system during relaxation was then investigated to determine if this implementation of the hyperdynamics method has any adverse effects on the relaxed configuration. While the volume, average end-to-end length, and average radius of gyration were not affected, the ratio of *trans* to *gauche* RIS states changed significantly during the relaxation (Figure 4.4). This change occurred quickly and the magnitude of the overall change was related to the floor energy. These results indicate that the use of a

constant floor energy over all dihedral angles affects the forward and reverse transition rates differently. Since the potential energy well of the *trans* state has on average a lower energy, it is affected more than the higher energy *gauche* state potential energy wells. As a result, the transition rate from the *trans* state to the *gauche* states is increased more than the reverse transition rate leading to a statistically incorrect distribution of RIS states. In this case, the increased percentage of *gauche* states will result in the molecules becoming more coiled than they would be in an unaccelerated simulation.

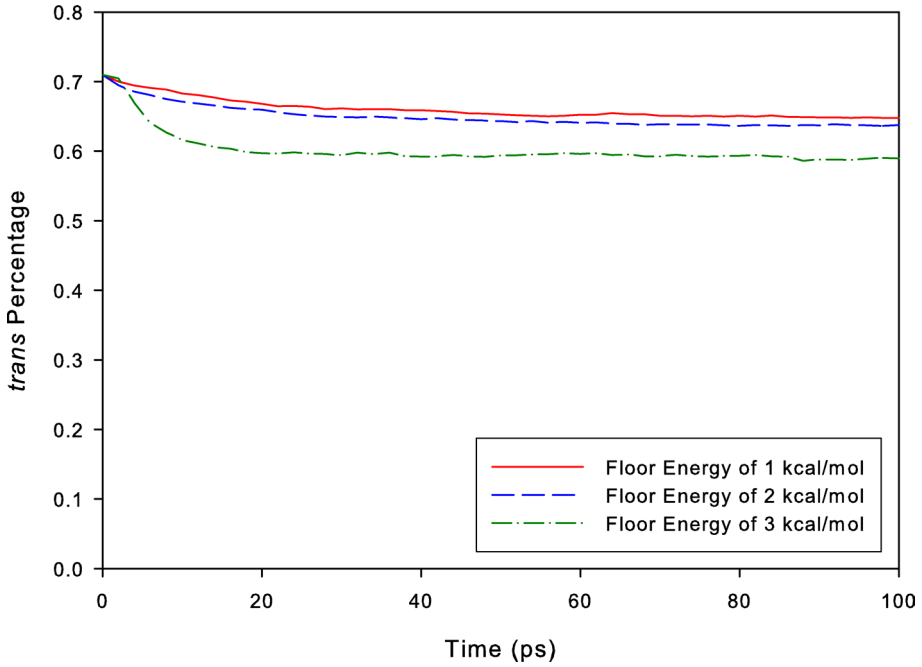

Figure 4.4 Evolution of the percentage of *trans* states during relaxation simulation of a polymer system consisting of 50 molecules each with 1000 unified atoms using dihedral boost potentials with different floor energies at a temperature of 300 K.

The applications of the floor energy methods described in the literature did not depend on the reverse rates of transitions, so they were not affected by this apparent limitation. To overcome this issue, either the parameters of the blending function could

be modified to better represent the shape of the original potential or different floor energies could be used for each energy well as suggested by Wang et al. (2001). Attempts at modification of the parameters did not result in a shape of the accelerated potential matching the original potential due to the inability of the blending function to match shape of the energy wells. The use of multiple floor energies was implemented, one for the *trans* well and one for the two *gauche* wells. The *gauche* floor energy was set to a near maximum level of 3.26 kcal/mol. The *trans* floor energy was then adjusted until the equilibrium percentage of *trans* states was the same as the unaccelerated percentage, resulting in a *trans* floor energy of 2.85 kcal/mol.

The accuracy of the derived boost factor was evaluated by comparing the rate of *trans-gauche* state transitions in both accelerated and unaccelerated relaxation simulations. LAMMPS was further modified to enumerate the number of dihedral transitions per time step by inserting the required code into the dihedral potential calculations to store the previous dihedral state and compare it to the current state. The rate of transitions for the accelerated simulation was found to be half of rate for the unaccelerated simulation, indicating that the boost factor is too high (Figure 4.5).

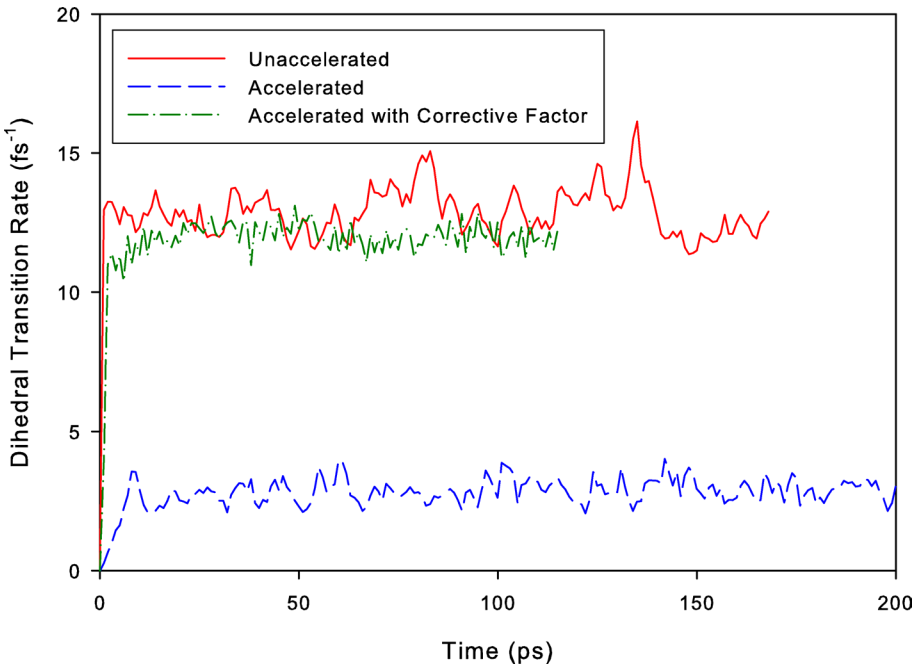

Figure 4.5 Rate of dihedral transitions during relaxation simulation of a polymer system consisting of 50 molecules each with 1000 unified atoms using the multiple floor energy boost potential with and without a corrective factor at a temperature of 300 K.

The high boost factor is likely a result of not accounting for the interaction between overlapping dihedral subsystems. Since boost potentials should not be applied to a system/subsystem when a near a transition configuration, when a dihedral group is near a transition configuration, the overlapping dihedral groups should also not have any boost potentials applied. While this approach may improve the correctness of the boost factor by reducing the transition rate discrepancies, it will also result in a lower boost factor for the entire system, as approximately 75% of the dihedral groups will no longer be boosted due to overlapping dihedral groups being near a transition state. The effectiveness of this approach will be discussed later.

Another approach is to artificially correct the boost factor to account for any violations to the underlying assumptions made in deriving the hyperdynamics method.

This approach will have the benefit of determining the maximum possible boost factor when applying boost potentials to the dihedral groups. A constant corrective factor was applied to the boost factor so that the number of dihedral transitions in the accelerated simulation matched the number of dihedral transitions in the unaccelerated simulation, i.e.,

$$boost_{corrected} = boost \cdot f_{boost}, \tag{4.14}$$

where f_{boost} ($f_{boost} < 1$)is the corrective factor. From the dihedral transition rate differences between the accelerated an unaccelerated systems (Figure 4.5), the corrective factor was found to be 0.26. The application of the constant corrective factor substantially reduces the boost factor (Figure 4.6).

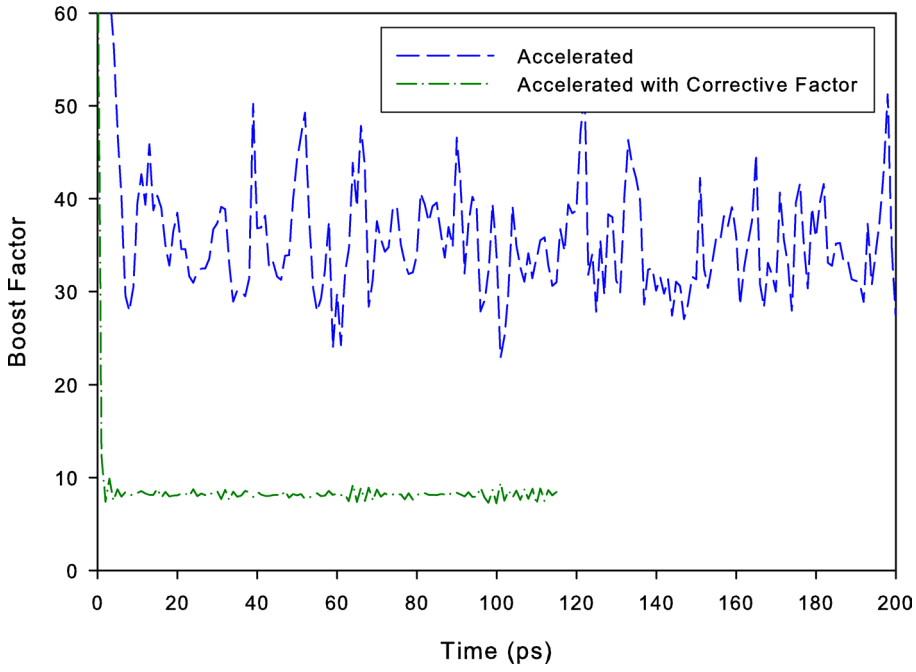

Figure 4.6 Boost factors during relaxation simulation of a polymer system consisting of 50 molecules each with 1000 unified atoms using the multiple floor energy dihedral boost potential with and without a corrective factor at a temperature of 300 K.

At this point, both the structure of the relaxed configuration and the rate of dihedral transitions are equivalent between the accelerated and unaccelerated cases. The effectiveness of this method when applied to deformation simulations was then investigated. It is apparent from the stress-strain results (Figure 4.7) that the constant scaling factor is insufficient to account for the approximations made in this method. As the system is deformed, the percentage of dihedral groups with configurations near a transition increases. As a result, the boost factor should be reduced as the number of dihedral groups near transition states increases. The constant scaling factor does not account for this behavior.

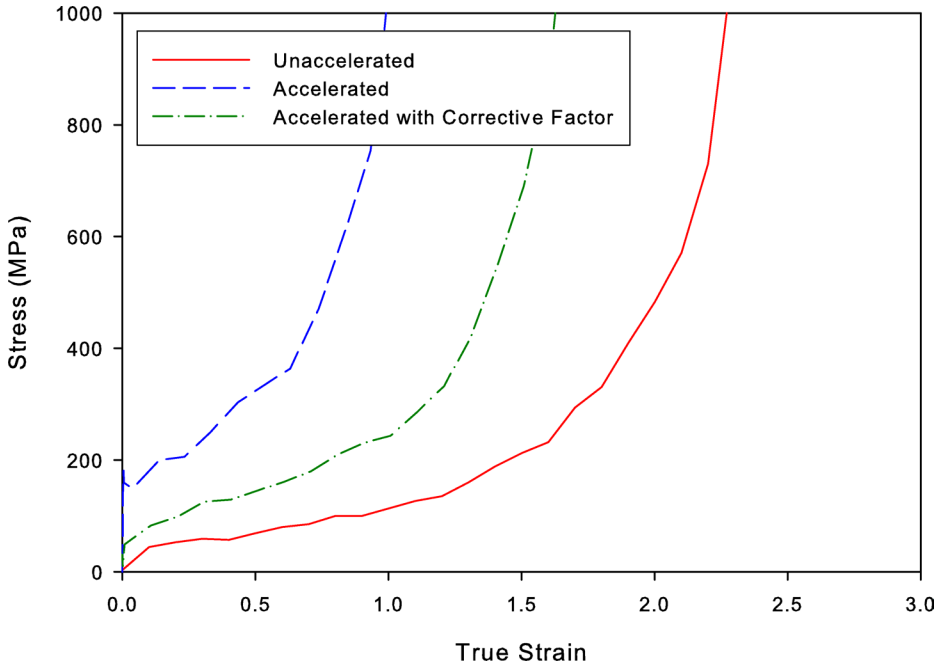

Figure 4.7 Stress-strain curves during uniaxial deformation simulations of a polymer system consisting of 50 molecules each with 1000 unified atoms using the multiple floor energy dihedral boost potential at a temperature of 300 K and a true strain rate of 10^{10} s^{-1} comparing the effect of a constant corrective factor.

More elaborate corrective factors could be employed in order to better fit the accelerated deformation behavior with the unaccelerated deformation behavior. For example, the corrective factor could be made a function of the deformation of the system, the virial stress in the system, or the change in entropy in a manner such that the acceleration of the system is reduced as the deformation is increased. However, these relationships would not be based on correcting the violation of the no boost potential near a transition state assumption of the hyperdynamics method. Additionally, these relationships would involve significant reductions of the boost factor as deformation progresses, making this approach too complicated and system-specific, reducing any benefit of employing this accelerated dynamics method.

To determine whether overlapping dihedral groups are the primary cause for the discrepancies between accelerated and unaccelerated transition rates, the multiple floor potential was only applied to dihedral groups that do not overlap one another. The overall system boost factor is very similar to the case where all of the dihedral groups were accelerated (Figure 4.8).

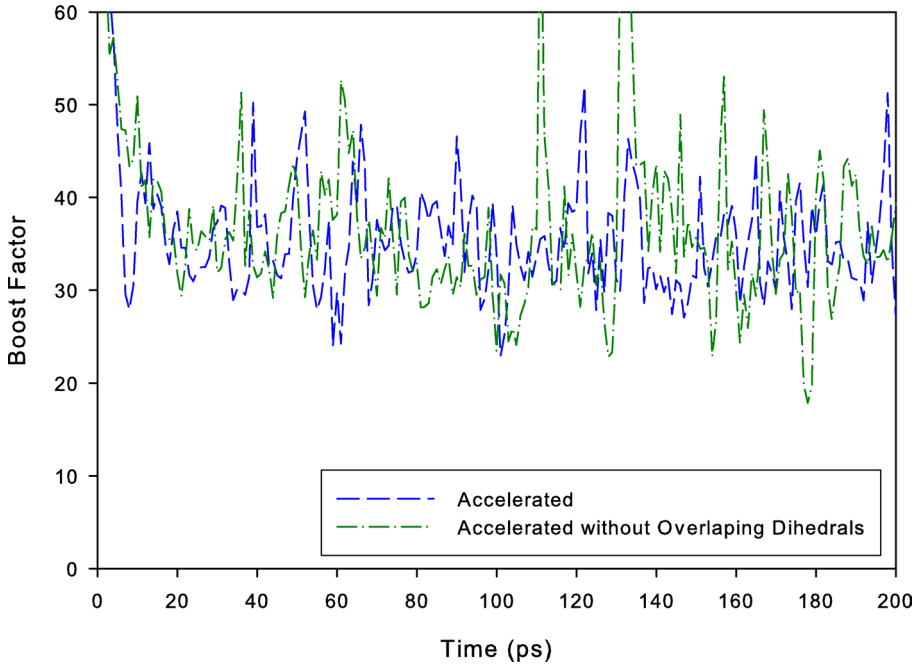

Figure 4.8 Boost factor during a relaxation simulation of a polymer system consisting of 50 molecules each with 1000 unified atoms at 300 K with the multiple floor energy dihedral boost potential not applied to overlapping dihedrals.

Since this approach eliminates 75% of the dihedral groups from being accelerated, the overall increase in the potential energy of the system is significantly reduced. Since the boost factor is similar to the case where all of the dihedral groups were accelerated, the rate of dihedral transition is lower (Figure 4.9).

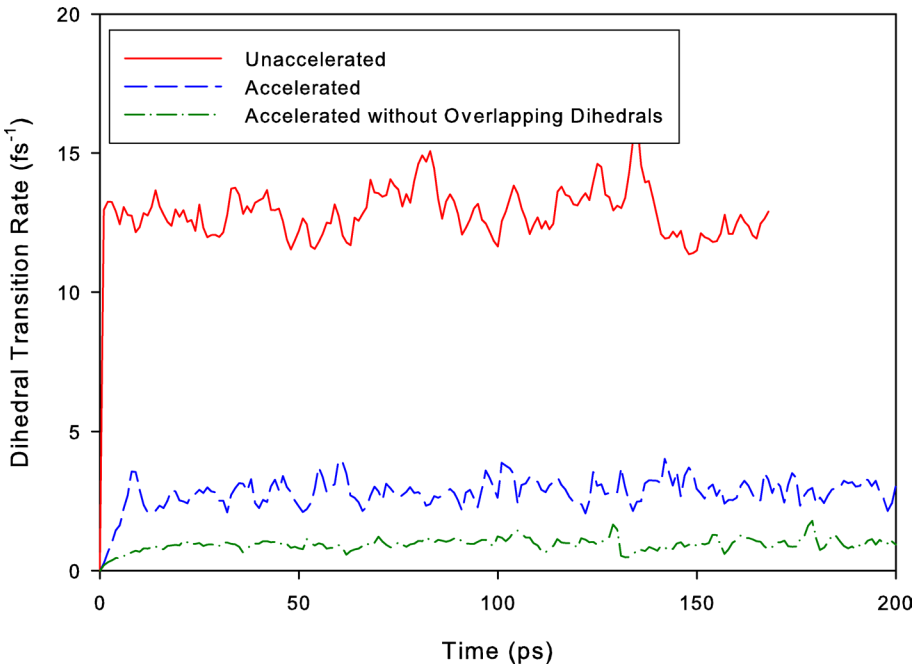

Figure 4.9 Rate of dihedral transitions during a relaxation simulation of a polymer system consisting of 50 molecules each with 1000 unified atoms at 300 K with the multiple floor energy dihedral boost potential not applied to overlapping dihedrals.

Similar to the previous approach of overlapping dihedral groups, the use of non-overlapping dihedral groups still requires a corrective factor. Even though the dihedral groups do not overlap along the backbone of the molecule, dihedral groups from other molecules or from further sections of the same molecule that are in close geometric proximity will still be affected by a boost potential. In effect, even the non-overlapping dihedral groups are still interacting. Additionally, the similar boost factors indicate that the canonical ensemble average may not be appropriate for determining the overall boost factor for the system. Number averaging was also applied, but the results were not improved.

Conclusions

One of the fundamental assumptions made in the derivation of the hyperdynamics method is that the system cannot be accelerated when the configuration of the system is near any transition state. In the case of large polymer systems of 50,000 atoms, several dihedral transitions are typically occurring at each time step somewhere in the system. The approach of subdividing the entire system into many sub-systems then averaging the boost factors of these sub-systems to determine the overall system boost factor still results in interactions between these sub groups, violating the basic hyperdynamics assumption. Implementation of hyperdynamics or any similar time acceleration method would require either a new method to subdivide the system into non-interacting sub-systems or a substantial investigation into statistical averaging methods that may account for the interactions between the subgroups.

One possible sub-dividing method would be to spatially decompose the simulation cell. Utilizing the parallel processing code within the molecular dynamics program which already performs spatial decomposition of the simulation cell would simplify the implementation of this method. However, the large number of sub-regions required to sufficiently limit the transition rate per sub-region could result in significant communication overhead between the processes, reducing the effectiveness of the method. Another approach to determine the boost factor is to consider the free energy of the system instead of just the potential energy. Due to the entropic nature of polymer systems, the effect of entropy on the boost factor could be significant, especially during deformation. The entropy of the system could be determined in a computationally efficient manner by use of rubber elasticity network models which are discussed in detail

in Chapter 6. The end-to-end length of the chains along with the structure of each chain can be implemented into a rubber elasticity model to determine the entropy at any point during the simulation.

Since the maximum boost factors possible for the polymer systems of interest in this research are less than an order of magnitude, even if the interaction problem is overcome, the time acceleration methods do not seem to be capable of meeting the original goals of implementing these methods for this research: to account for polymer mechanisms that occur at many orders of magnitude slower than can be simulated with molecular dynamics. However, if the boost factor can be accurately determined over a wide range of simulations, the acceleration methods could eventually be used to substantially reduce the computational cost of MD simulations of large polymer systems which would be a valuable contribution and one worth pursuing.

CHAPTER 5

ATOMISTIC MODELING OF ENTANGLEMENT EVOLUTION

Entanglements are generally defined as mechanical interlocks of polymer molecular chains. Since entanglements comprise a large portion of the total interconnects in a physical polymer network, and contribute substantially to network behavior and irreversibility, both the number and evolution of entanglements must be determined and their effect must be implemented into any physically-based continuum constitutive model.

Background

One of the primary issues in atomistic modeling of entanglements is the process of actually defining an entanglement in computations. Yashiro et al. (2003) determined entanglements geometrically by defining "flexion nodes" in the initial configuration and following these nodes during deformation. They found that the "flexion nodes" did not always correlate to entanglements during deformation as the "flexion nodes" would straighten out. Tanaka et al. (2000) identify "local knots" that are defined by comparing the geometry of neighboring chains. This method cannot account for all of the various forms of entanglements.

Very little research has been done to study the evolution of entanglements during deformation with molecular modeling tools. In one case, entanglements are created artificially by kinking two chains about one another (Theodorou 2004). These artificial

entanglements are tracked, but other entanglements that are formed randomly during creation of the initial structure or that develop during deformation are not accounted for.

In another study, cross-links are evolved during deformation by the introduction of a cross-linking potential (Rottach et al. 2004). The evolution of cross-links is then modeled in a modified rubber elasticity network model. Though the mechanisms of cross-link formation are different than entanglement evolution, the linking of the molecular and network models is similar to the directions of the present research.

Here, the use of bond forces to identify and track entanglements is proposed as a more effective method than geometry-based methods. Since geometric identification of entanglements is unlikely to be accurate due to the various means by which a chain can become constrained by other chains or even with itself, an alternate method is desired. The purpose behind studying entanglement evolution in this research is due to their role as mechanical interconnects. Instead of identifying entanglements as a function of their geometric properties, it is proposed to identify them as a function of their impact on deformation behavior. Since interconnects serve as restrictions to deformation, it is assumed that this restriction will generate tensile loads on the chains that are constrained by the interconnects. LAMMPS has been modified to enable the extraction and evaluation of bond information during deformation. This information is analyzed to find consecutive bonds under tension that would indicate a segment of a constrained polymer chain. Due to the dynamic behavior of MD simulations, bonds in a polymer chain under tension could sporadically have compressive forces. As a result, for each desired sampling of the system to find consecutive bonds under tension, many adjacent time steps are queried to determine the average bond data. With this line of reasoning, evaluating

the progression of these constrained chains gives the evolution of effective entanglements.

Method

LAMMPS was modified to output the bond lengths for each bond pair at specific intervals throughout the simulations. At the completion of the simulation, this output file is used to determine the location and evolution of entanglements. A post-processing application written in Perl is used to analyze the output file. Normally, LAMMPS outputs the bond data in a random order and provides no information regarding which bond belongs to which molecule and the order in which the bonds are connected within the molecule. The post-processing application must then use a reference file that contains this information. The data input file for LAMMPS includes the geometric coordinates of each atom and the connectivity, which provides the necessary information. The post-processing application reads the LAMMPS data input file to set up the internal memory structures to represent the molecular connectivity of the polymer system being modeled. As the bond information from the simulation is read at each time step, the atom numbers given for each bond pair are used to reference the corresponding bond in the memory structure. After reading the bond information for each time step, all of the bond data are then properly placed into memory arrays for each corresponding bond pair.

By default, LAMMPS does not store the bond forces for each bond pair; it simply aggregates the forces determined by each potential for each atom. Since LAMMPS uses and stores the difference between the actual bond length and the equilibrium bond length

for each bond pair, this signed distance from equilibrium is actually outputted and used for the bond calculations.

Outputting the bond information at each integration time step would generate an enormous amount of data and significantly increase the run time of the simulation. For example, a 50,000 atom polymer system will have on the order of 50,000 bond pairs and the simulations in this research are run from between 300,000 and 3,000,000 integration steps. If all of the bond lengths and corresponding bond pair atom IDs are written for each time step, the output file would contain over 1.5×10^{10} values. The resulting output files would consume substantial disk space and require significant computational resources to post-process. When running an MD simulation on a computational cluster, the inter-process communication becomes a limiting factor on the overall scalability of the simulation. Outputting the bond information for each time step would dramatically increase the communication requirements and the requirement of synchronizing the simulation at the end of each time step would further reduce computational efficiency. As a result, the bond length information was only written periodically.

However, due to the dynamic nature of MD simulations, the bond lengths can fluctuate significantly about their average lengths over periods of only tens of time increments. To determine this average, the bond lengths were outputted for enough subsequent time steps to capture at least two vibrational periods starting at each output interval. The maximum and minimum distances from equilibrium were determined for each of these sequences of time steps. These values were then averaged and used to represent the effective distance from equilibrium for each interval.

Once the averaged bond lengths have been determined, each molecule is traversed along its backbone investigating the bond length for each consecutive bond pair. When the first bond length is reached that is greater than the pre-defined threshold length, a new constrained segment is assumed to have begun. The bond pair ID is recorded as the starting point for this segment. The number of consecutive bond lengths that are greater than the threshold is considered to be the length of the segment, i.e., once a bond length is reached that is less than the threshold length, the segment is considered to have ended. The last bond pair of the constrained segment is recorded as the end point of the segment. The search is then continued along the molecule until the next length greater than the threshold is reached, at which point the above process is repeated.

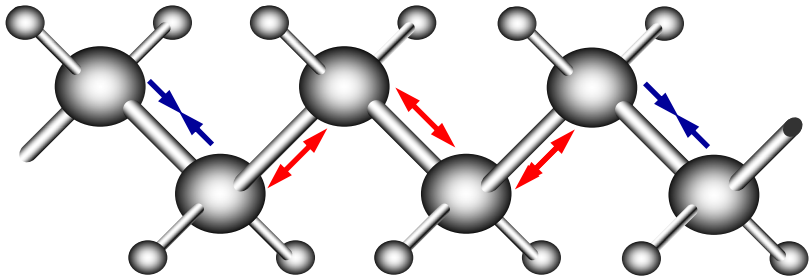

Figure 5.1 Diagram showing a constrained segment consisting of stretched bond lengths (red) flanked by compressed bond lengths (blue).

After analyzing every bond of every molecule in the system, the post-processing application has now stored the total number of constrained segments found and, for each segment, the length of the segment as well as the starting and ending points. This information can then be used to track the evolution of the constrained segments.

After the attributes for each constrained segment are determined for each time interval recorded, the post-processing application then compares the locations of the

segments between consecutive time intervals. If the location of a segment in the earlier time interval overlaps the location of a segment in the latter time interval, the segment is considered to be stable. If there are no segments in the latter time step that occupy the same location as a segment in the earlier time interval, the earlier segment is considered to have been removed. Likewise, if multiple segments in the latter time interval have locations that overlap the location of an earlier segment or if a segment in the latter time interval occupies a location that is not occupied by a segment in an earlier time interval, the extra segments in the latter interval are considered to be added. With this information, the evolution of the number of stable, removed, and added segments can be tracked as well as the overall number of segments.

There are two parameters used in this method that have an effect on the results; the minimum number of consecutive bonds with lengths above the threshold distance and the value of the threshold distance. A parametric study was performed to investigate the dependencies of these parameters on the results. As expected, the actual number density of entanglements changes as these parameters are changed; however the shape of the curves remains the same (Figures 5.2 and 5.3).

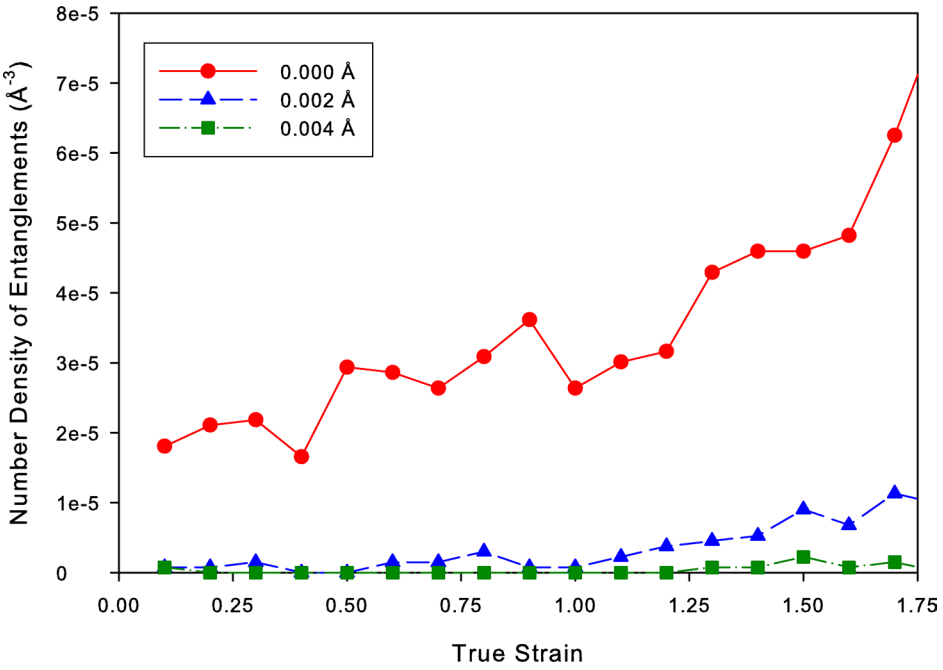

Figure 5.2 Evolution of the overall number density of entanglements during deformation of a 50,000 unified atom system at a true strain rate of 10^{10} s^{-1}, a temperature of 300 K, and different threshold distances.

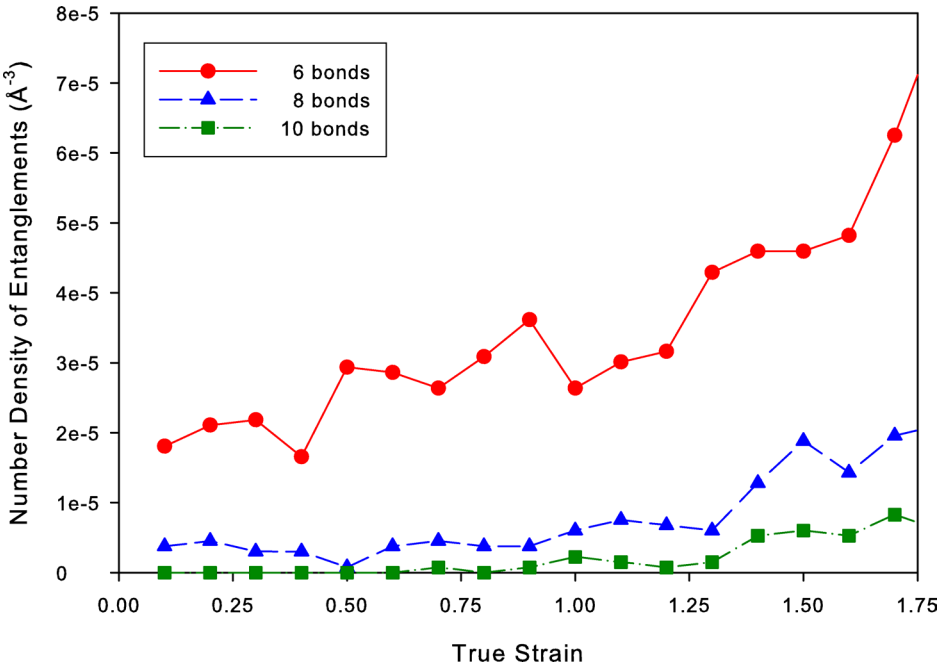

Figure 5.3 Evolution of the overall number density of entanglements during deformation of a 50,000 unified atom system at a true strain rate of 10^{10} s^{-1}, a temperature of 300 K, and different minimum number of consecutive bonds in tension.

These relationships show that the number densities of entanglements determined by this method are not quantitative, but that the evolution of entanglements is independent of the parameter values within the ranges evaluated. In other words, the evolution of entanglements using this method is qualitative and insensitive to the parameters.

In the remaining simulations, the threshold was set equal to zero and the minimum number of consecutive bonds set equal to six. These values were chosen since they produce results with a significant number density of entanglements relative to the fluctuations or noise in the number density of entanglements.

Results

Simulations were performed to develop a comprehensive description of the evolution of entanglements under various rates of deformation, temperatures, molecular chain lengths, numbers of atoms in the model, and initial chain conformations. As found in Chapter 2 when investigating the dependency of initial chain configurations and the total number of atoms in the simulation cell on the stress-strain behavior, the evolution of entanglements was also found to be relatively insensitive to differences in the initial configuration (Figure 5.4) and the number of atoms in the system (Figure 5.5) at true strains below 1.75.

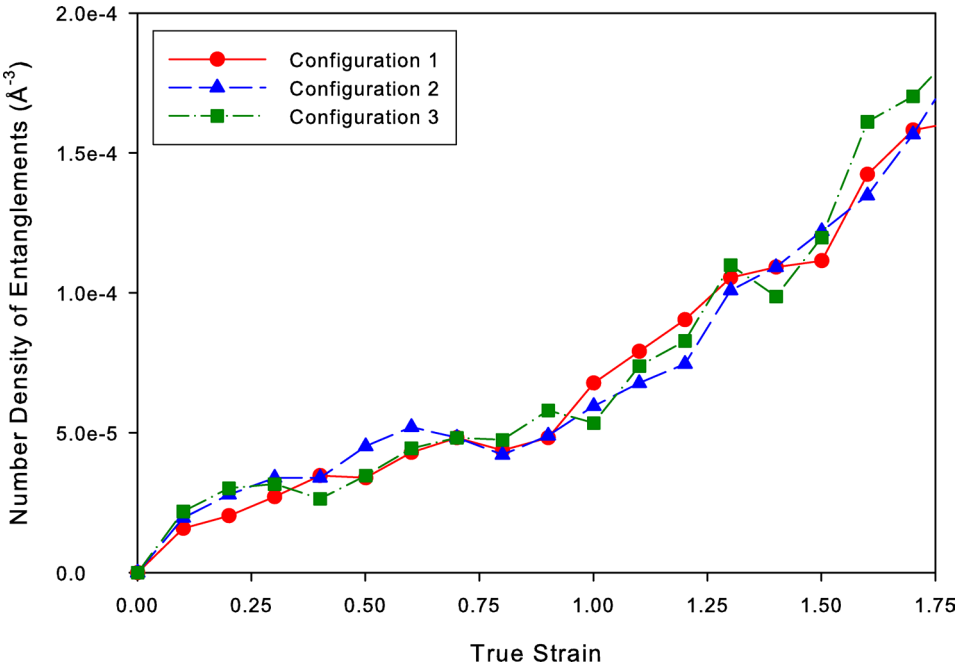

Figure 5.4 Evolution of the overall number density of entanglements during deformation of a 50,000 unified atom system at true strain rate of 10^{10} s^{-1}, a temperature of 300 K, and different initial configurations.

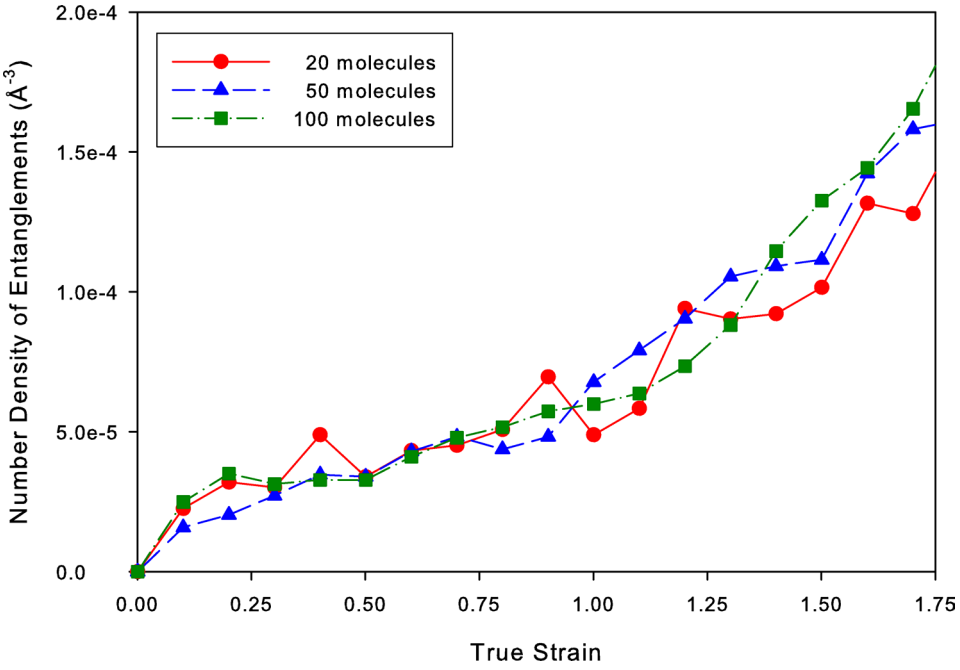

Figure 5.5 Evolution of the overall number density of entanglements during deformation at a true strain rate of 10^{10} s^{-1}, a temperature of 300 K, and different numbers of 1,000 unified atom molecules in the system.

The bond force method was applied to systems deformed at various strain rates, temperatures, and molecular weights. As expected, the results show a decrease in the number density of entanglements at lower strain rates relative to higher rates (Figure 5.6). The slower strain rates permit more time for relaxation events to occur that may reduce the number density of entanglements compared to higher strain rates.

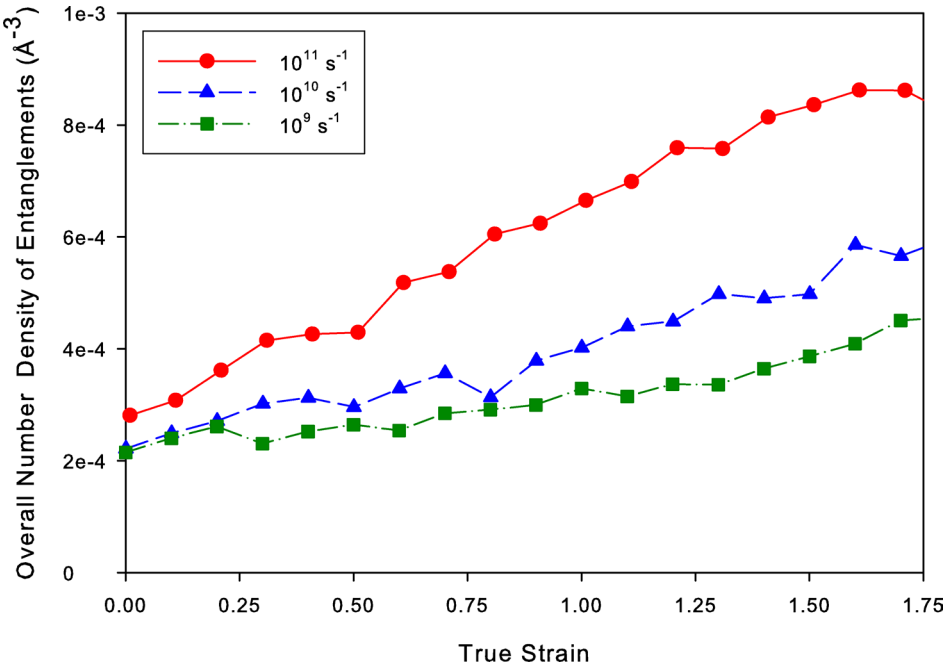

Figure 5.6 Evolution of the overall number density of entanglements during deformation of a 50,000 unified atom system at true strain rates of 10^{11}, 10^{10}, and 10^{9} s^{-1} and a temperature of 300 K.

The evolution of the number density of stable entanglements (Figure 5.7) shows the same trends as the overall number density of entanglements (Figure 5.6). The overall number density of entanglements is higher than the number density of stable entanglements at equivalent strains because the stable quantity does not include entanglements that were removed or added during that time interval. The similarity

between the overall and stable graphs indicates that the evolutions of the removed and added entanglements should also be similar to one another.

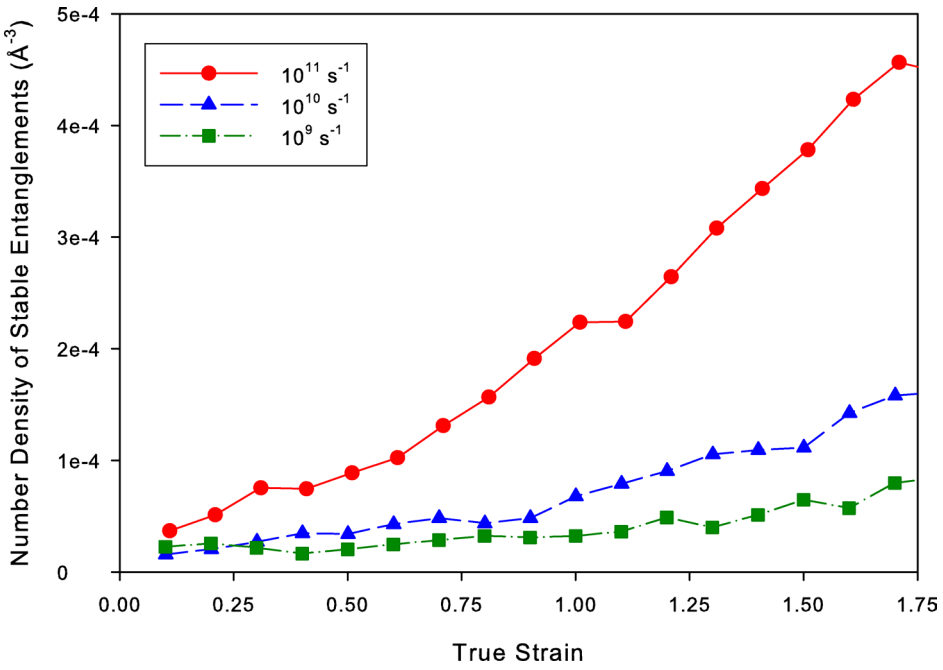

Figure 5.7 Evolution of the number density of stable entanglements during deformation of a 50,000 unified atom system at true strain rates of 10^{11}, 10^{10}, and 10^{9} s^{-1} and a temperature of 300 K.

The strain rate results seem to indicate that there are two competing processes. First is a possibly rate-independent increase in the number density of entanglements as deformation progresses. The second is a rate-dependent process that reduces the number density of entanglements. At the higher strain rates, the rate-independent increase in entanglements dominates, while at the slower rates there is sufficient time for rate-dependent processes to significantly reduce the number density of entanglements. The rate-independent process could be a result of entanglements that are initially too loosely coupled but become active as deformation tightens their interactions. The rate-dependent

process could be a result of chains sliding past one another or sufficient energy being added to the system that physical interactions are overcome, eliminating the effect of the physical interactions. The similarity between the evolution of the addition (Figure 5.8) and removal of entanglements (Figure 5.9) predicted earlier does not give further insight into this assumption of the mechanisms.

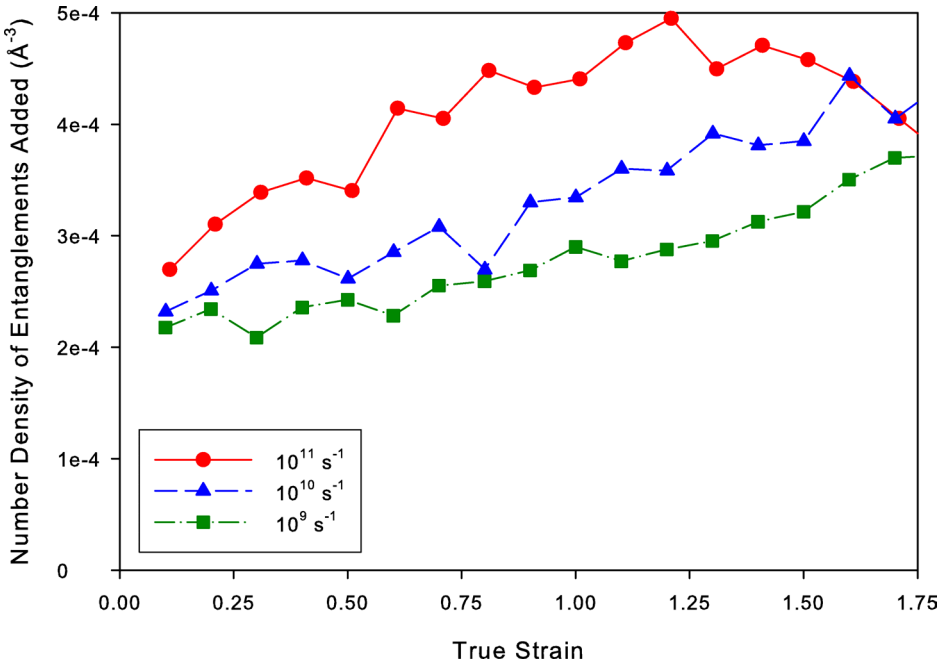

Figure 5.8 Evolution of the number density of added entanglements during deformation of a 50,000 unified atom system at true strain rates of 10^{11}, 10^{10}, and 10^{9} s^{-1} and a temperature of 300 K.

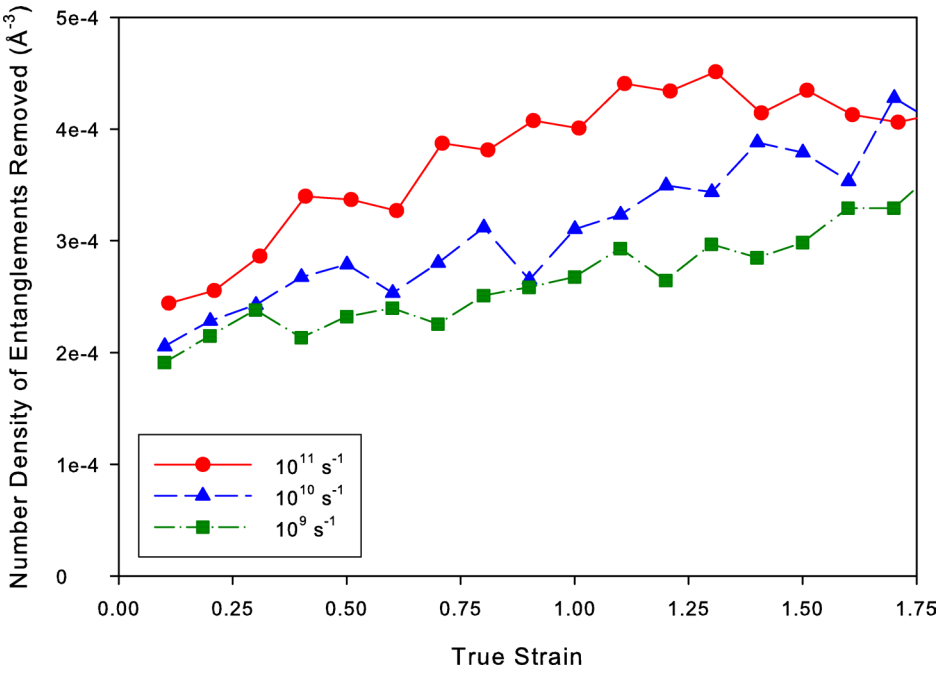

Figure 5.9 Evolution of the number density of removed entanglements during deformation of a 50,000 unified atom system at true strain rates of 10^{11}, 10^{10}, and 10^{9} s^{-1} and a temperature of 300 K.

These results may not be representative of actual entanglement evolution. It is difficult to justify the number density of entanglements increasing by an order of magnitude as the high strain rate results suggest. It is also curious that the number density of entanglements is directly proportional to the post-yield stress, as shown in Figure 5.10. The behavior of a network of polymers does not demand an increase in the number density of entanglements to support increased stress at higher strains, as the stress will normally increase significantly at higher strains with a constant number density of entanglements.

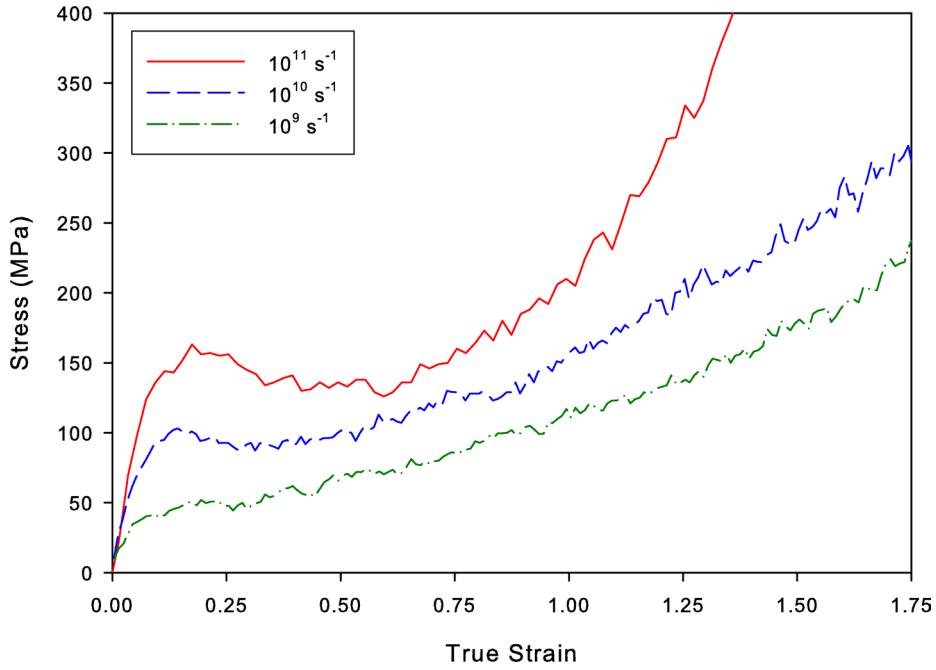

Figure 5.10 Evolution of stress in the draw direction during deformation of a 50,000 unified atom system at true strain rates of 10^{11}, 10^{10}, and 10^{9} s^{-1} and a temperature of 300 K.

The average length of each segment constrained by entanglements (Figure 5.11) and the percentage of bonds that are found in these constrained segments (Figure 5.12) indicate that constrained segments are small in size and number at low strains and increase in size and number proportional to the rate of increase in stress (Figure 5.10).

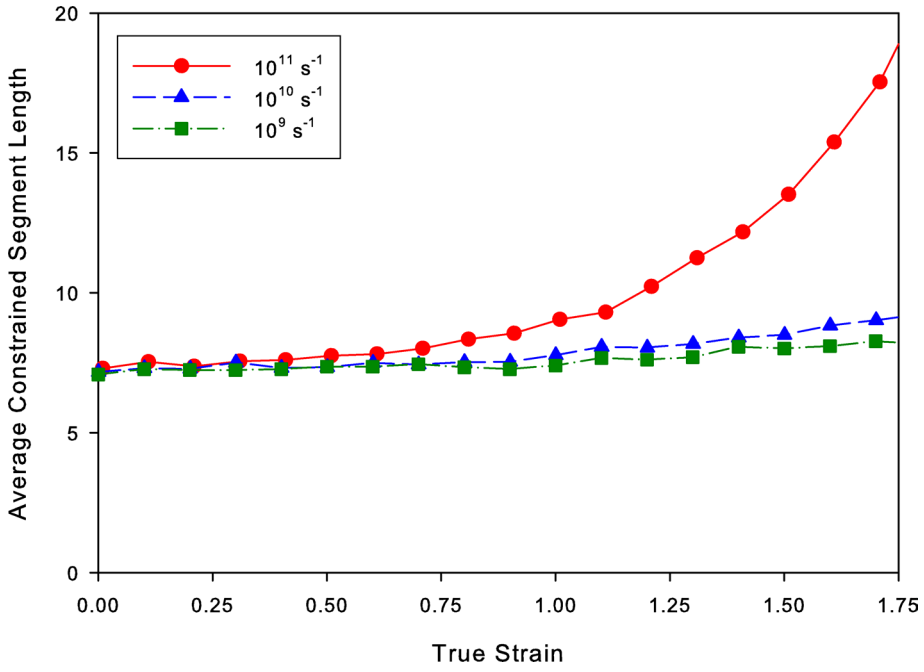

Figure 5.11 Average constrained segment size between entanglements during deformation of a 50,000 unified atom system at true strain rates of 10^{11}, 10^{10}, and 10^{9} s^{-1} and a temperature of 300 K.

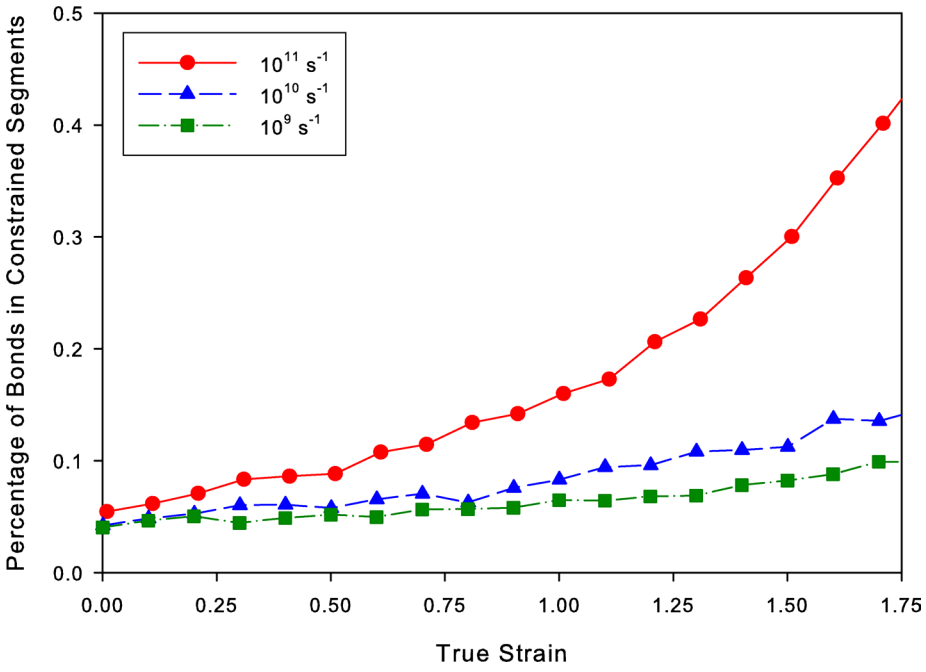

Figure 5.12 Percentage of bonds that are found in constrained segments between entanglements during deformation of a 50,000 unified atom system at true strain rates of 10^{11}, 10^{10}, and 10^{9} s^{-1} and a temperature of 300 K.

The temperature results are counter-intuitive. The number density of entanglements at low strains should be relatively equivalent for the different temperatures (Figure 5.13). The number density of entanglements should then decrease at a higher rate for the higher temperature simulation. While the number density of entanglements decreases at a higher rate for higher temperatures, the number density of entanglements at low strains is higher for higher temperatures. This discrepancy is likely a result of the increased kinetic energy at the higher temperature increasing the average bond lengths. If this is the case, the bond lengths need to have a correction factor applied to them to compensate for the temperature effects.

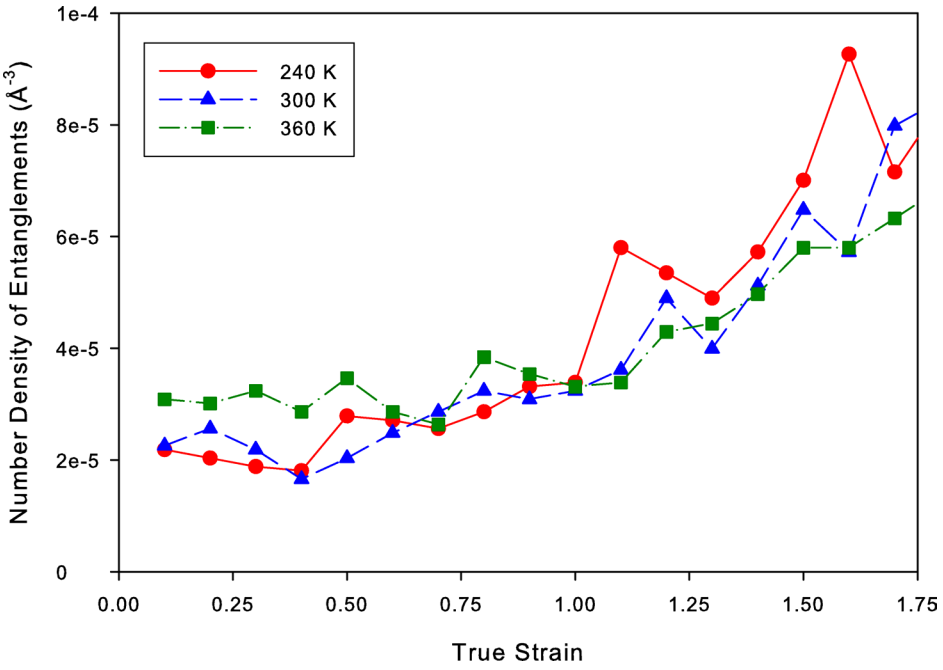

Figure 5.13 Evolution of the number density entanglements during deformation of a 50,000 unified atom system at a true strain rate of 10^9 s^{-1} and temperatures of 240, 300, and 360 K.

For the relatively small differences in molecular weights that could be evaluated, there is not a significant dependence on the length of the molecule (Figure 5.14). There seems to be consistently fewer entanglements for the higher molecular weight chains at high strains, which is not expected. Longer chains should maintain entanglements more than shorter chains due to the increased motions required to slide past one another.

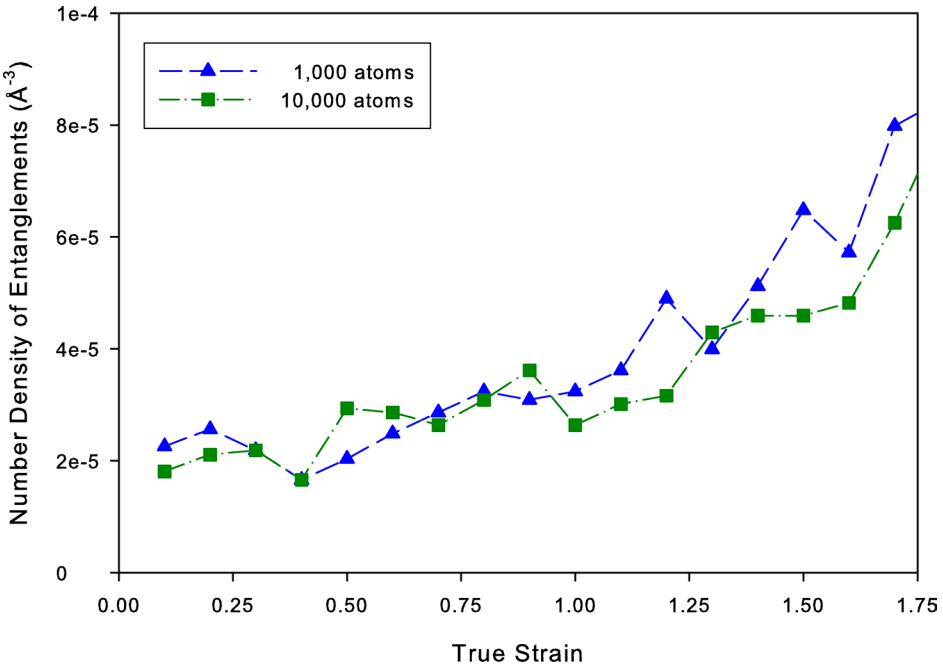

Figure 5.14 Evolution of the number density of entanglements during deformation of a 50,000 unified atom system at a true strain rate of 10^9 s^{-1}, a temperature of 300 K, and molecule lengths of 1,000 and 10,000 atoms.

Conclusions

While this method provides data that indicates a possible evolution of entanglements in a consistent and qualitative manner, taking all of the results into consideration sheds significant concern over the accuracy of this method to track the actual evolution of entanglements. Since there is not any known experimental evidence

to compare these results with, it is difficult to validate this method of determining entanglement evolution. As a result, a method that can determine the evolution of entanglements that is quantitative in nature and can be shown to represent actual entanglement evolution through additional evidence would be more desirable for multiscale modeling. Such a method is proposed and evaluated in Chapter 6.

CHAPTER 6

ATOMISTIC INVESTIGATION OF NETWORK MODELS

Rubber elasticity models based on statistical mechanics represent the mechanical behavior of polymers by determining the change in entropy of a network of chains composed of freely rotating rigid segments with the chain ends joined together at interconnects. Typically these interconnects represent chemical cross-links, but they could be associated with any morphological entity that would constrain a polymer molecule at a particular point, such as crystallites and entanglements (Figure 6.1).

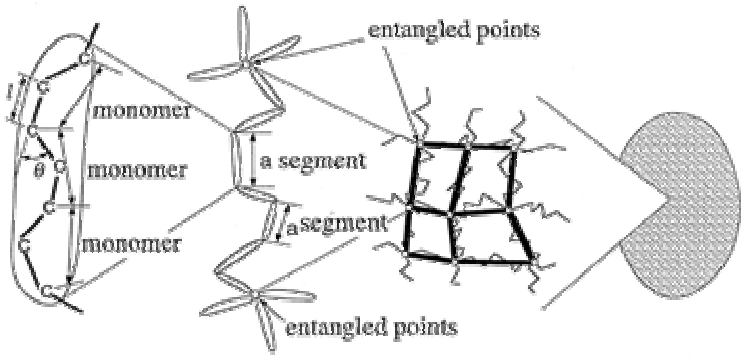

Figure 6.1 Rubber elasticity representation of a polymer (Tomita 2000).

Statistical mechanics based models of rubber elasticity make several assumptions that can limit their effectiveness in modeling actual polymer networks: volume exclusions for overlapping segments are not accounted for, the segments are freely rotating and rigid, intermolecular interactions such as van der Waals forces are neglected, and all of the chains between interconnections are considered to have an equal number of segments. In addition, the effects of morphological features such as crystal size and

orientation on the behavior of the polymer are not included. Network models are also strain history and strain rate independent. These models are traditionally good at modeling behavior of highly cross-linked polymers, but poor at modeling the behavior of semi-crystalline polymers. The primary cause for this discrepancy is that the low density of interconnects makes the effect of volume exclusion and chain interactions more significant. Additionally, the effective number of interconnects in a semi-crystalline polymer evolves during deformation due to crystallization and entanglement slippage.

Though volume exclusion is not inherently included in rubber elasticity models, these models are typically extended to require constant volume deformation. The effect of maintaining constant volume can be considered to mimic the effect of the combination of volume exclusion and non-bonded interactions.

There has been little use of molecular modeling techniques to bridge the predictions of rubber elasticity network models to real polymer behavior. Typically, the network model parameters are simply fit to macroscopic experimental data, but no connection is made between the values of these parameters and the structure of the polymer being modeled.

Everaers (1999) performed a comprehensive study comparing classical and tube models to simplified molecular models of polymer melts. He found that classical models under-predicted the stress at a given strain and the tube models predicted the stress well. A similar study (Grest et al. 2000) agrees with these results. Bergstrom and Boyce (2001) studied the evolution of bond angles, bond forces, chain angles, and chain end-to-end lengths using both molecular dynamics simulations and an eight-chain network model. They found good agreement of these attributes between the two methods. None

of these comparisons between network models and atomistic simulations investigated the relation of actual polymer systems to network models. Angle and dihedral potentials were neglected to more closely mimic the freely rotating rigid segment assumption in rubber elasticity.

It is desirable to find a link between actual polymer properties and network model parameters. Ideally, the network model's parameters would be set equal to the actual values of the polymer, e.g. the number of monomers and interconnects (cross-links, entanglements, crystallites). These parameters would then be scaled with a material parameter specific to a particular polymer in a manner similar to the characteristic length factor, C_{inf}, which is used to correlate a polymer molecule's structure with its equilibrium end-to-end length ($r^2 = N\, C_{inf}\, l^2$).

MD Simulations of Ideal Network

As previously mentioned, rubber elasticity models do not directly represent the behavior of actual polymers primarily due to the lack of inclusion of segment interactions and deviation of monomer structures from freely rotating rigid segments. To demonstrate the magnitude of the differences in these simulation approaches, a MD simulation was compared to a rubber elasticity model. A system of 100 molecules consisting of 500 atoms each and fully interconnected with 50 cross-links was generated using the initial configuration method discussed in Chapter 3. The system was deformed using the methods described in Chapter 2. The rubber elasticity model by Wu and van der Giessen (1993) considers the principal stress components, $\tilde{\sigma}_i$, to be determined by the deformation of a network of chains with an orientation distribution, $C_a(\theta,\phi)$, i.e.,

$$\hat{\sigma}_i = \frac{nk_BT}{4\pi}\sqrt{N}\int_{\theta=0}^{\pi}\int_{\phi=0}^{2\pi} C_a(\theta,\phi)\mathcal{L}^{-1}\left(\frac{\lambda_e}{\sqrt{N}}\right)\lambda_e m_i^2 \sin\theta\, d\theta\, d\phi - p\,, \tag{6.1}$$

where n is the number density of chains, k_B is the Boltzmann's constant, T is the absolute temperature, N is the number of freely rotating rigid segments per chain, p is a hydrostatic stress that is determined from the boundary conditions, $\mathcal{L}^{-1}$ is the inverse of the Langevin function,

$$\mathcal{L}(x) = \coth(x) - \frac{1}{x}, \tag{6.2}$$

and λ_e is defined as

$$\lambda_e^2 = \sum_{i=1}^{3} m_i^2 \lambda_i^2\,, \tag{6.3}$$

in which λ_i are the principal stretches and the direction components are defined as

$$\begin{aligned} m_1 &= \sin(\theta)\cos(\phi) \\ m_2 &= \sin(\theta)\sin(\phi)\ . \\ m_3 &= \cos(\theta) \end{aligned} \tag{6.4}$$

The two network model parameters n and N were assigned the number density of molecules and the number of bonds per molecule in the MD model respectively. The deformation of a polymer using MD simulations as detailed in Chapter 2 reaffirms the expected stiffer behavior of actual polymers compared to the network model (Figure 6.2). The amount of deviation of the MD results from the network model results are rate dependent; therefore, the rate of deformation must be considered when correlating network models with MD.

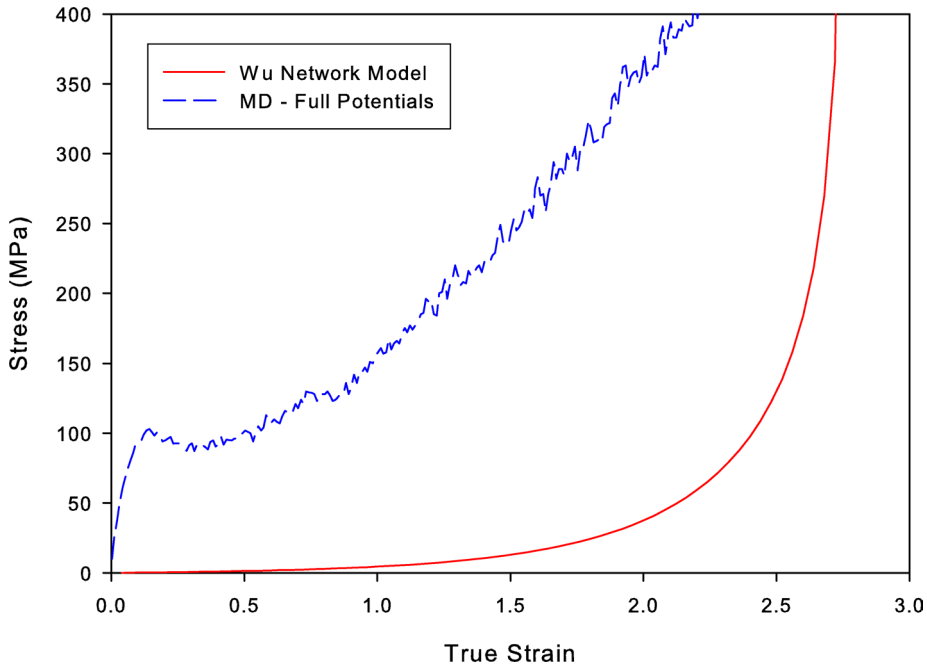

Figure 6.2 Comparison of the stress-strain behavior for an ideal network model and a molecular dynamics simulation of 100 cross-linked molecules with 499 bonds each at a true strain rate of 10^{10} s^{-1} and a temperature of 300 K.

To determine a link between the network model parameters and the actual structure of the polymer, the effects of these two parameters must be separated and investigated independently. One approach is to assume that the difference between the monomer structure and a freely rotating segment is captured by the number of segments per chain, *N*, and that the segmental interactions are captured by the number density of chains, *n*. In a typical MD simulation, separating the effect of deformation of the polymer on these two parameters is not possible. Here, the MD simulation is initially modified to eliminate segmental interactions so that the relationship between *N* and the actual monomer structure can be determined. Segmental interactions can be eliminated by simply disabling the non-bonded pair potential.

Since the non-bonded pair potential is required to maintain proper pressure-density relationships, the deformation procedure described in Chapter 2 that was used to generate the results shown in Figure 6.2 must be modified. Instead of using an NPT ensemble, the density-pressure relationship must be explicitly defined. Here, an assumption is made that the volume does not change significantly during deformation so an NVT ensemble can be used which fixes the system volume and temperature during deformation. This assumption is the same for the network model as well. In addition to using the NVT ensemble, the simulation cell had to be stretched in the uniaxial draw direction and compressed in the directions perpendicular to the uniaxial draw direction as prescribed in Chapter 2 in order to maintain constant deformation at each time step. If a pair of opposing faces on the periodic unit cell is displaced from one another, the NVT ensemble considers the new shape to be the constant volume in its calculations. As a result, all dimensions of the simulation cell must be prescribed prior to the NVT calculations for each time step as the NVT algorithm will not modify the periodic unit cell's dimensions, only the positions of the atoms within the prescribed boundaries. A system of 200 molecules was used, consisting of 250 atoms each and fully interconnected with 100 cross-links. With the absence of the non-bonded pair potential, these 100 cross-links are the only relevant segmental interactions in the network model. Additionally, these cross-links remain constant in number throughout deformation, making correlation with the network model much simpler. As a result, the number density of chains, n, is now defined, i.e,

$$n = \frac{2n_x}{V_{cell}} \tag{6.5}$$

where n_x is the number of cross-links in the simulation cell and V_{cell} is the volume of the simulation cell. The network model was run with the same deformation evolution, number density of chains, and the number of segments per chain as the MD simulation. Figure 6.3 shows the MD simulation still having a stiffer response than the ideal network model, but it is much more similar than the results from the full MD simulation. The difference between the full MD simulation (Figure 6.2) and the MD simulation without non-bonded potentials (Figure 6.3) indicates the effect of volume exclusion and other segment interactions. The difference between the MD simulation and ideal network shown in Figure 6.3 represents the effect of the deviation of the monomer structure from a freely rotating rigid segment. These results indicate that the effect of segment interactions is much greater than the effect of monomer structure for this polymer system, which is not surprising considering the simplicity of the polymer structure investigated. More complex polymers may reduce the difference between these effects or may even reverse the dominance of the effect of segment interactions over the effect of the structure. Another fundamental difference between the MD and network models is that the network model does not include the dynamic effects that are inherent in MD. To minimize the effects of the dynamics, either a sufficiently slow strain rate MD simulation or a Monte Carlo or similar statistical method should be performed on the polymer system. However, an argument can be made that the dynamics are dependent upon the structure of the molecule and the effects of the dynamics should be included within the network model parameter *N*.

The network model was then fit to the MD results by modifying the parameter *N* (Figure 6.3) The fit value for *N* of 23 indicates that that 10.8 polyethylene bonds are

equivalent to a freely rotating rigid segment which correlates reasonably well with 8.0 polyethylene bonds determined experimentally (Aharoni 1983).

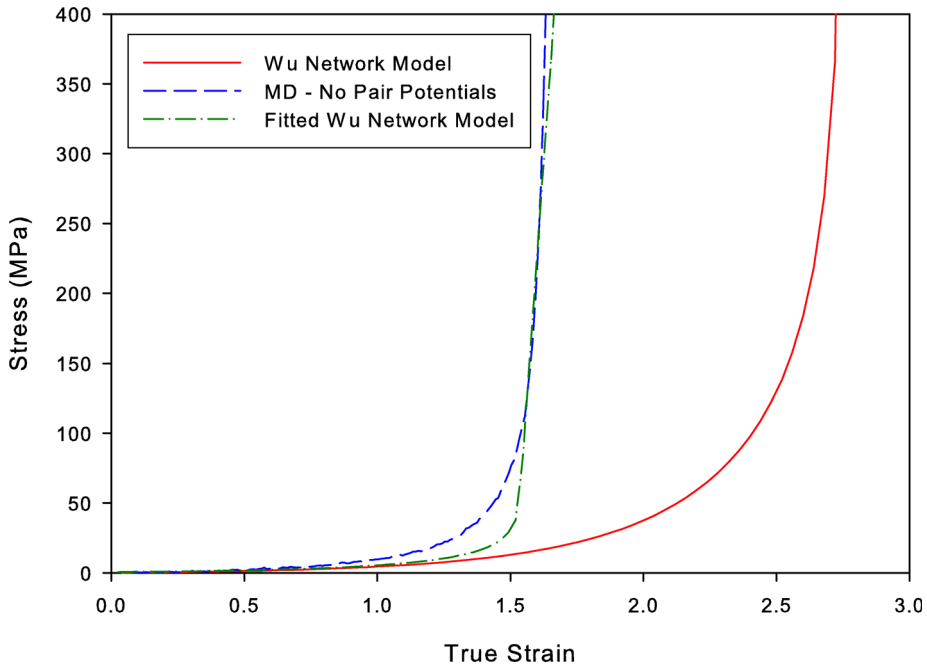

Figure 6.3 The stress-strain curve for an ideal network model is fit to the stress-strain curve from a molecular dynamics simulation of 100 cross-linked molecules with 499 bonds each at a true strain rate of $10^9 s^{-1}$ and a temperature of 300 K with the pair potentials disabled.

The stress-strain results for the simulation without non-bonded potentials was found to only be rate sensitive for true strain rates above 10^9 s^{-1} (Figure 6.4).

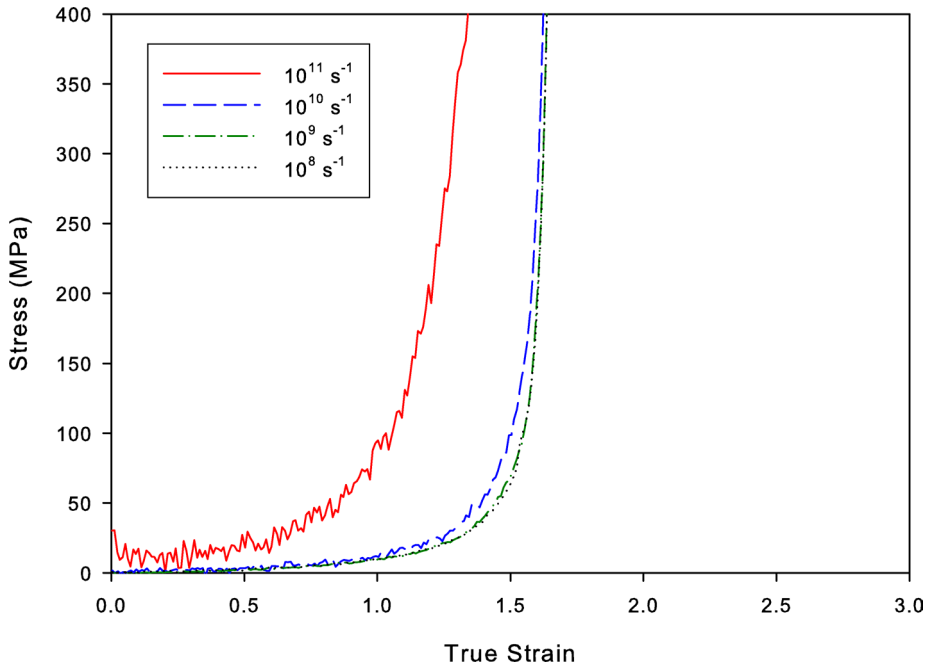

Figure 6.4 Rate dependency of the stress-strain behavior for molecular dynamics simulations of 100 cross-linked molecules with 499 bonds each at a temperature of 300 K with the pair potentials disabled.

With the two parameters of the network model now known, the overall number density, N_a, of freely rotating rigid segments can be determined, i.e.,

$$N_a = nN\,. \tag{6.6}$$

An interesting and useful aspect of this parameter is that it should be constant for a particular polymer regardless of the deformation characteristics such as rate, temperature, or deformation mode. As a result, N_a becomes a property of the polymer. With N_a a constant, n and N are now dependent on one another in a definable manner throughout deformation, leading to a single independent parameter for the network model.

If the assumption is made that entanglements have the same effect as cross-links on an assembly of polymer chains, the network model can be used to evaluate the number

and effect of entanglements. Assuming a similar connectivity as cross-links, the number density of entanglements, n_e, is directly related to the number density of chains in the system, $n_e = n / 2$. Here, entanglements represent the effect of any non-bonded physical interactions on the parameters of the network model. This definition of entanglements includes both traditional representation of looping mechanical interlocks and non-traditional, non-specific resistances to deformation due to neighboring segments. As a result, entanglements are not considered to be specific structures in this method, but rather a measure of the effective constraints in the system. Since the parameters N and n_e are dependent, the number density of these effective entanglements can be determined by fitting the network model to the stress at a specific strain for an MD simulation or even experimental stress-strain data, i.e.,

$$n_e = \frac{N_a}{2N} \tag{6.7}$$

Since network models are strain history independent, any point on the stress-strain plot can be used to determine the number density of effective entanglements at that point (Figure 6.5). The network model can then be fit to the stress and stretch at any point to determine the number density of entanglements at that point.

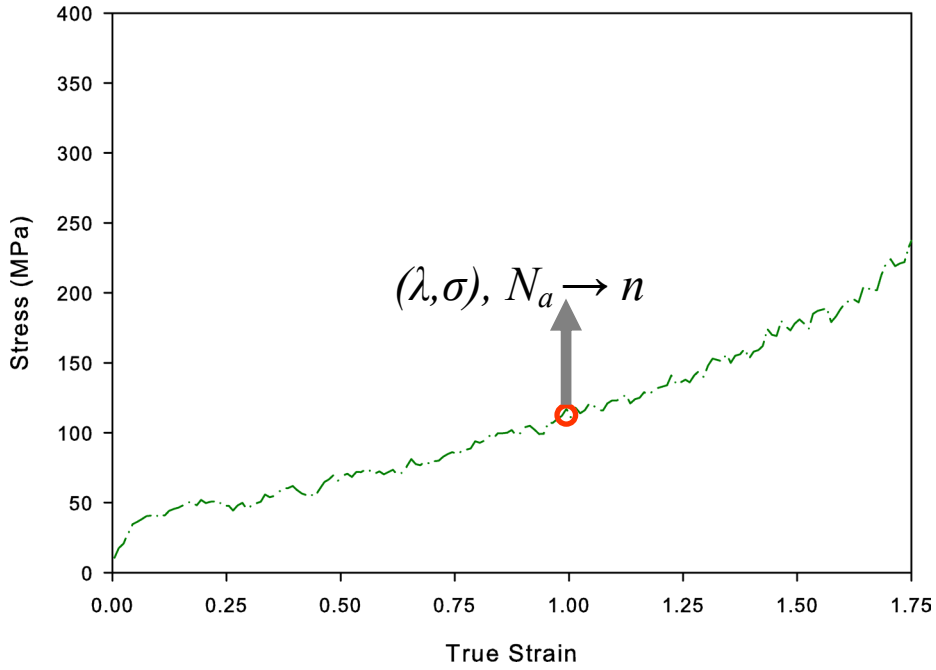

Figure 6.5 The number of entanglements can be determined at any point of a stress-strain curve.

This method provides the means to determine the continuum network model parameters entirely from molecular dynamics simulations. Evolution equations and their respective parameters can be determined from the number density of entanglements data collected from MD simulations at various rates, temperatures, molecular weights, and any other pertinent dependency.

Results

This method was used to determine the number density of entanglements throughout the deformation of a non-cross-linked polymer system. An uncross-linked polymer system consisting of 50 molecules with 1,000 atoms each was generated using the method described in Chapter 3. The entanglement evolution was determined for

various true strain rates (Figure 6.6), temperatures (Figure 6.7), and molecular weights (Figure 6.8). The strain rate entanglement results demonstrate how little variation on the number of entanglements is required to yield substantial stress differences (Figure 6.9).

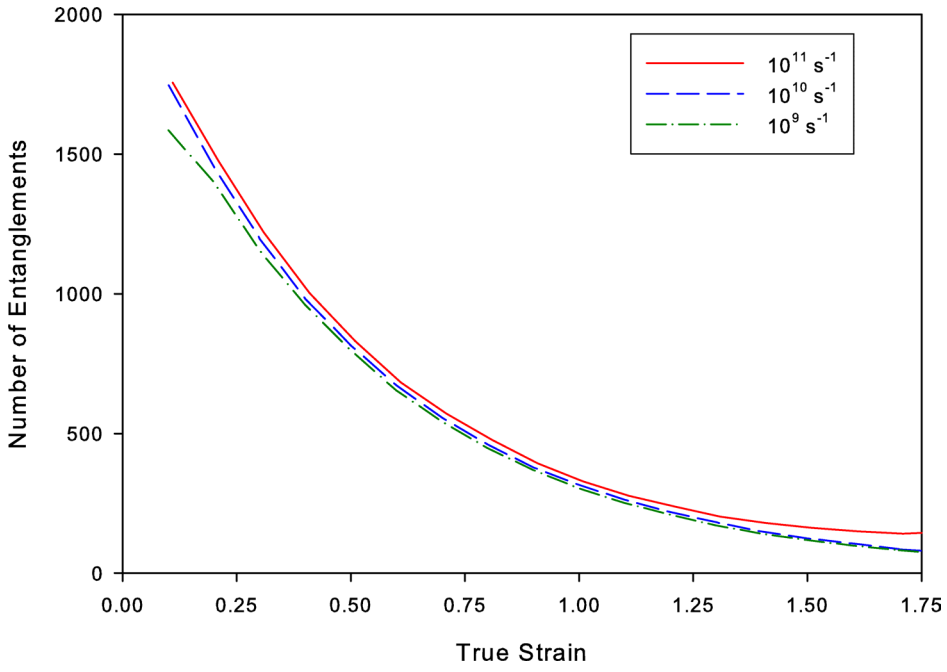

Figure 6.6 Evolution of the number of entanglements in the simulation cell resulting from uniaxial deformation of 50 molecules with 1,000 atoms each at a temperature of 300 K and different true strain rates.

The temperature results show a measurable dependence on temperature at low strains that diminishes at higher strains. As expected higher temperatures lead to a reduction in the number of entanglements. The molecular weight results do not show significant differences within the ranges evaluated.

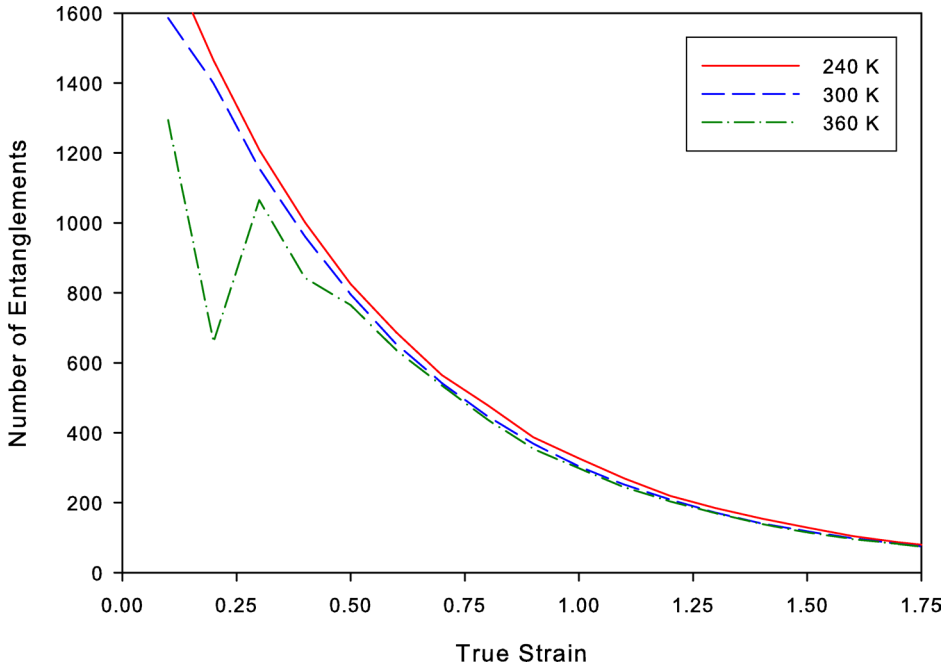

Figure 6.7 Evolution of the number of entanglements in the simulation cell resulting from uniaxial deformation of 50 molecules with 1,000 atoms each at a true strain rate of 10^9 and different temperatures.

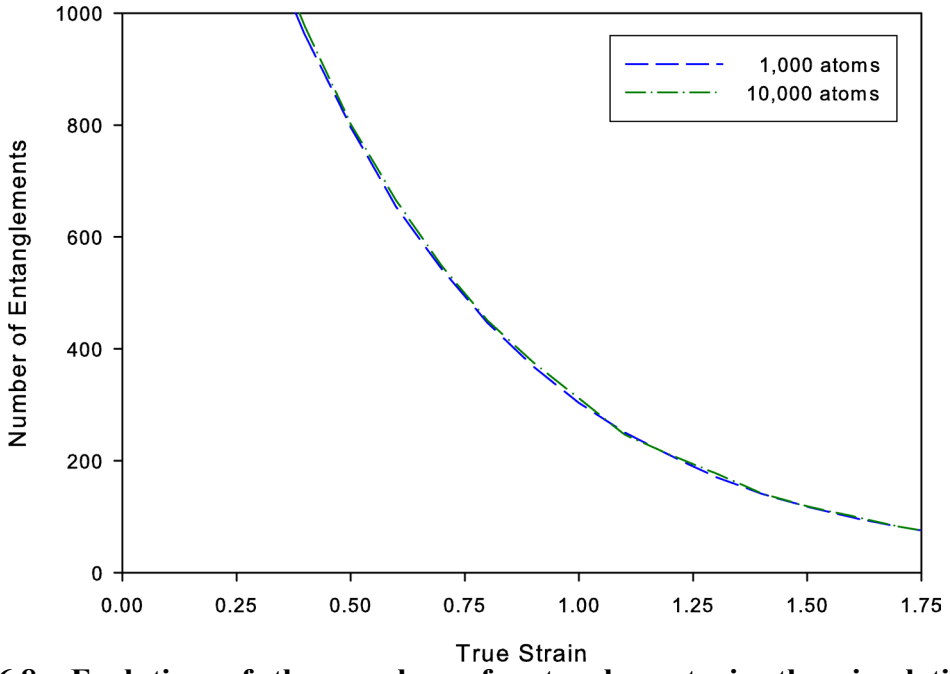

Figure 6.8 Evolution of the number of entanglements in the simulation cell resulting from uniaxial deformation of a 50,000 atom system at a true strain rate of 10^9, a temperature of 300 K, and different molecular weights.

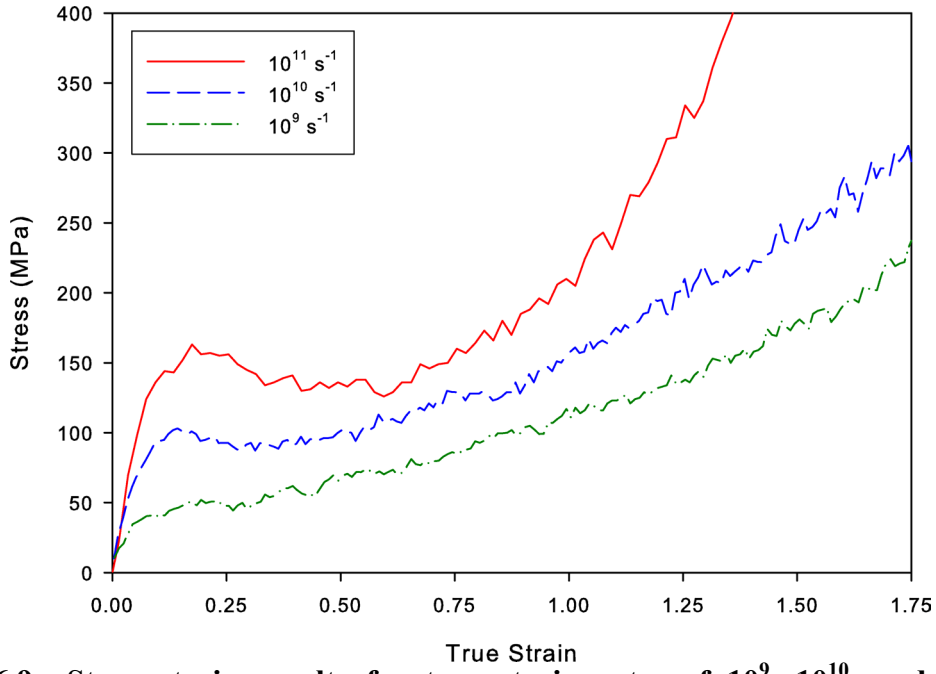

Figure 6.9 Stress-strain results for true strain rates of 10^9, 10^{10}, and 10^{11} s^{-1} resulting from uniaxial deformation of 50 molecules with 1,000 atoms each at a temperature of 300 K.

The results at different strain-rates show a significant reduction in the number of entanglements as deformation initially progresses at low strains. The rate of this decrease in the number of entanglements increases with a reduction in strain rates. This portion of the deformation includes the initial linear elastic and subsequent flow effects. Lower strain rates result in a lower number of entanglements at the end of this initial section. At high strains, there is an increase in the number of entanglements that is more prominent at the higher strain rates. These results, along with the results from the bond-force method (Chapter 5), indicate that two processes may be occurring: a rate dependent process and a strain dependent process. Since the number of entanglements varies with the deformation attributes and with strain, a constant parameter cannot be used to relate the number density of chains in the model with the number density of entanglements, as originally sought using a parameter similar to C_{inf}.

Through a trial-and-error process, relationships were found to model the two proposed processes. The rate independent process is considered to be dependent on the overall deformation of the material, i.e.,

$$n_{e_{base}} = n_{e_{init}} \exp\left(S(V-1)\right), \tag{6.8}$$

where $n_{e_{init}}$ is the initial number density of entanglements, S is a parameter that accounts for the magnitude of the dependency on deformation, and V is the overall normed stretch given by

$$V = \sqrt{\frac{1}{3}\sum_{i=1}^{3}\lambda_i^2}\,. \tag{6.9}$$

Here, λ_i are the principal stretches of the network.

The rate-dependent reduction in the number density of entanglements is assumed to have a power law dependence on the stress and an Arrhenius dependence on the temperature, i.e.,

$$\dot{n}_{e_{slip}} = \dot{n}_{e0} \exp\left(-\frac{\Delta F_e}{k_B T}\right)\tau^q \left(\frac{n_{e_{base}} - n_{e_{slip}}}{n_{e_{base}}}\right), \tag{6.10}$$

where $\dot{n}_{e0}$ is an entanglement slippage pre-exponential constant, ΔF_e is the thermal activation energy, q is the stress related power factor, and τ is the equivalent shear stress. The last term accounts for the reduced number of entanglements available for slippage as deformation progresses. The equivalent shear stress is defined by

$$\tau = \sqrt{\tfrac{1}{2}\boldsymbol{\sigma}' \cdot \boldsymbol{\sigma}'}\,, \tag{6.11}$$

where $\boldsymbol{\sigma}'$ is the deviatoric stress tensor.

The entanglement results from Figure 6.6 where used to fit the parameters which are given in Table 6.1.

Table 6.1 Entanglement evolution parameters for fitting the MD-based entanglement results.

$n_{e_{init}}$	4.998×10^{21} cm^{-3}
S	0.607
$\dot{n}_{e0}$	2.186×10^{51} cm^{-3}s^{-1}
ΔF_e	2.000×10^{-19} J
Q	1.336

These equations were implemented into the network model so that the evolution of the number density of entanglements and stress could be evaluated over the full course of deformation. The modified network model fit the entanglement data well (Figure 6.10).

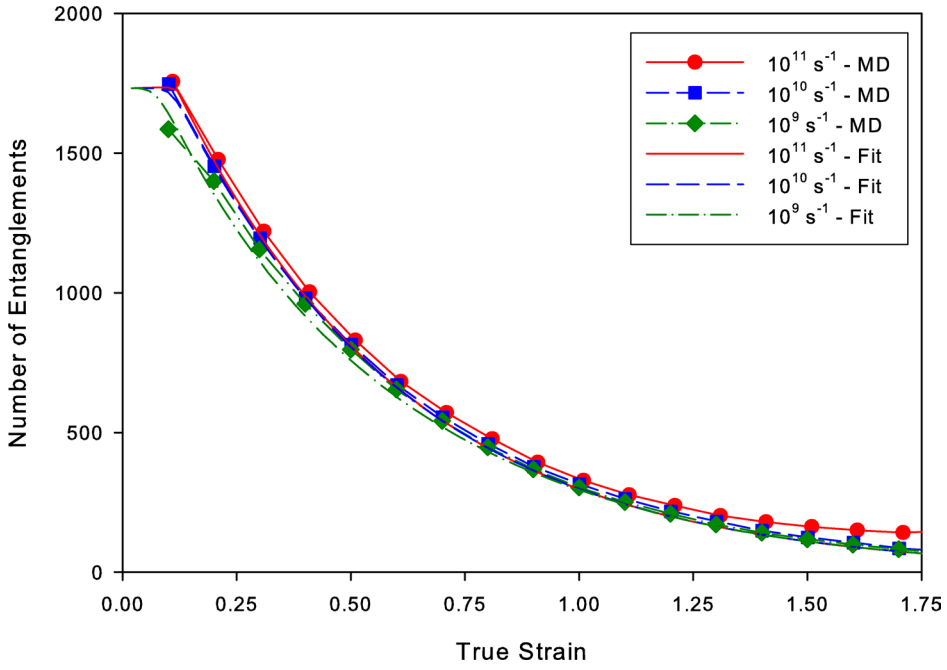

Figure 6.10 Comparison of the MD results and the fitted evolution equations for the number of entanglements resulting from uniaxial deformation of 50 molecules with 1,000 atoms each at a temperature of 300 K and different strain rates.

The stress determined by the modified network model also compares reasonably well with the MD results (Figure 6.11).

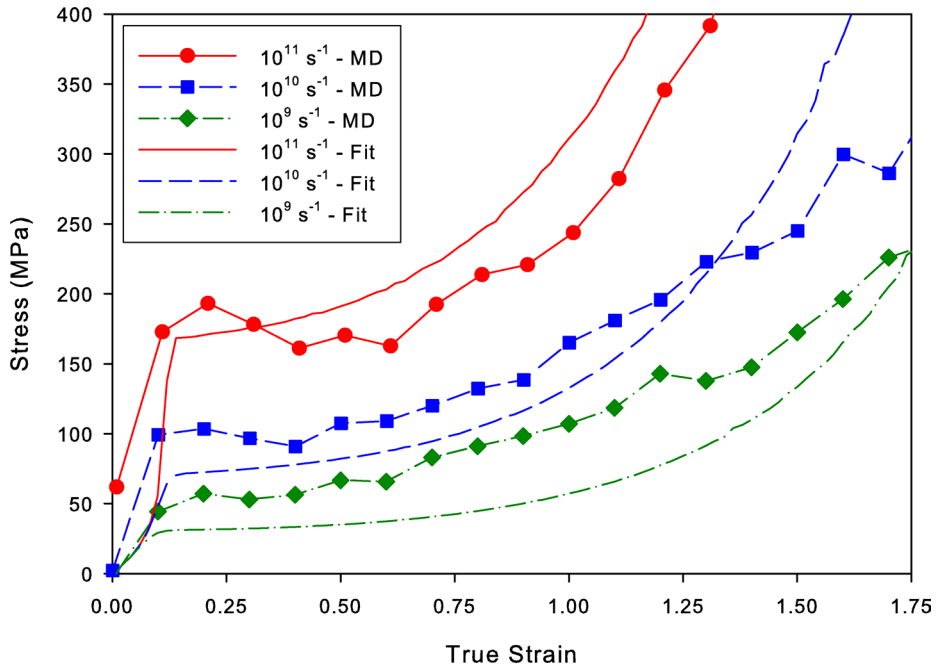

Figure 6.11 Comparison of the MD results and the fitted evolution equations for the stress resulting from uniaxial deformation of 50 molecules with 1,000 atoms each at a temperature of 300 K and different strain rates.

The hardening behavior is modeled well across the strain rates investigated. However, the yield strength is consistently under-predicted and the post-yield softening is not captured for the higher strain rates.

Conclusions

The method of defining entanglement evolution proposed here permits the quantitative determination of entanglements as related to a network model. There are several key assumptions that have been made in the development of this method. First

and foremost, the mechanical behavior of polymers is assumed to be able to be represented accurately by the statistical mechanics derived theories of rubber elasticity network models. Since the structure of the network models correlate well to the structures of polymers and network models with constant parameters have been shown to accurately represent the behavior of highly cross-linked polymers <insert Trealor reference>, this first assumption can be argued to be reasonable. The second assumption is that the effects of the polymer structure and segmental interactions can be separated and described separately by the two network model parameters, n and N. While seemly a questionable assumption, there are two aspects to the network model that make this assumption reasonable. First, the two model parameters are not independent, but related through the total number density of segments in the system, i.e., $N_a = n\,N$. In fact, while the effects of the structure and interactions of the polymer are separated into the parameters N and n, respectively, dependencies between these parameters are captured through N_a. Second, by eliminating all segmental interactions by excluding the non-bonded pair interactions in the MD simulation, this modified MD simulation represents the structure of the network model very well. The only discrepancy between the two methods is the dynamics which are included with MD. But the dynamics can be considered insignificant as long as the MD simulation converges on the correct locking strain, which is the measure used to fit the network model to the MD simulation. The third assumption is that all non-structural effects on mechanical behavior can be categorized as the result of entanglements. Since entanglements are defined here as the effect of segmental interactions and not solely by the traditional definition of looping chains, this assumption is reasonable.

This method is difficult to test experimentally since entanglements, especially with the broad definition of entanglements used in this research, are impossible to quantify. The most useful validation procedure is to implement the network model and entanglement evolution equations into a continuum model and test the model over a range of polymer systems and deformations. This validation is shown in part with the continuum model proposed in Chapter 7.

While this method has been solely applied to MD results here, it can also be used with a combination of MD simulations and experimental results. The MD simulations are required to determine the polymer structure property, N_a. However, once this parameter is defined through the use of MD simulations, any stress-strain results can be used to fit the entanglement evolution equations. This flexibility yields another approach to bridging the time scales of atomistic simulations and continuum experiments. An interesting future research topic would entail the use of a more complex polymer system that can also be evaluated both with MD models and experiments. The simple polymer system chosen in this research for the MD simulations is not well characterized experimentally as a purely non-crystalline material due to its low glass transition temperature, so this research direction cannot be carried out within the scope of the current research.

In constitutive models, the yielding behavior is typically modeled with a visco-elastic component that is distinct from the network model, e.g. Shepherd et al. (2006), Boyce et al. (2000), and Buckley and Jones (1995). The linear elastic and yielding behaviors demonstrated by many polymers can be considered to be caused by physical interactions of neighboring atoms. Since these physical interactions fall into the broad

definition of entanglements used here, the entanglement evolution equations could be used to simulate the visco-elastic behavior as well as the more traditional hardening behavior. While the relatively simple equations presented here do not accurately describe the correct yielding behavior, they may be close enough at the much slower strain rates typically modeled at the continuum level to be useful or more sophisticated evolution equations can be derived. Additionally, the fit is much better at lower strain rates that are more likely to be simulated with continuum models. Replacing the visco-elastic components would remove several model parameters and permit more direct linking between atomistic results and the continuum model. The effectiveness of these equations at simulating the visco-elastic behavior will be investigated with the constitutive model presented in Chapter 7.

CHAPTER 7

CONTINUUM MODEL

The continuum model serves as the framework that integrates the atomistic modeling results and links together all of the nano-structrual details into a macroscopic response. In this application, a continuum model must address the effects of distinct attributes of microstructure on the macroscopic behavior, and must reflect the statistical mechanics of thermally activated processes. The evolution of these microstructure attributes in effect are represented by internal state variables (ISVs, cf. McDowell (2005)) that enter into equations that directly relate to the physical properties of these structures.

Background

Constitutive models by Adams et al. (2000), Bergstrom et al. (2002), Boyce et al. (2000), and Wu and van der Giessen (1993) are typical of the state-of-the-art in that they synthesize the cumulative effects of orientation, crystallization, and entanglement slippage with phenomenological relationships to correlate mechanical behavior. These existing continuum models do not sufficiently consider the evolution and interdependencies of these major morphological attributes that occur in polymers during thermo-mechanical deformation, and the effect of these attributes on the polymer's mechanical behavior and other properties. Additionally, these primarily phenomenological models require the determination of many material constants based on mechanical testing.

A model has been presented (Shepherd 2002) that overcomes these deficiencies by defining ISVs that are directly related to the underlying morphological attributes. Evolution equations are implemented to simulate the interactions between these morphological attributes and the nonequilibrium evolution of these attributes with deformation. However, this model contains several deficiencies. The evolution equations for entanglement slippage were developed with no basis of actual entanglement evolution mechanisms. At high strains, the entanglement slippage equations were unable to reduce the number of entanglements at high strain rates enough to prevent premature strain locking; moreover, they did not reduce the number of entanglements as much at low strain rates to prevent any hardening. The crystallization kinetics were based solely on the orientation distribution of the overall chain end-to-end vectors and not on the distribution of the monomer or statistical segment orientations. As a result, the crystallization behavior conflicted to some extent with experimental data. Particularly, the model predicted an increase in overall crystallinity as the strain rate is increased, while experiments generally show the opposite behavior. The model assumed that entanglement evolution directly effects the orientation distribution of the end-to-end chains. While changes in the number density of entanglements does have an indirect effect on the orientation distribution of the segments within the chain by changing the number of segments per chain, the actual end-to-end orientation of the overall chain is not affected. This model was significantly enhanced in both theory and implementation to overcome these deficiencies and to improve the computational efficiency.

Model Development

As described in more detail in Chapter 6, statistical mechanics rubber elasticity models represent the mechanical behavior of polymers by determining the change in entropy of a network of chains composed of freely rotating rigid segments, with the chain ends joined together at interconnects. While in the theory, these interconnects represent cross-links, in practice they can represent any constraint of a polymer molecule at a particular point or on average, including crystallites, entanglements, and intermolecular barriers to free motion. This proposed model is unique in that all of the network model parameters are represented by history dependent parameters that evolve according to morphological changes. While previous models have linked network model parameters to the deformation state of the material, they have only addressed a single parameter at a time in a history independent manner and have not included the effects of a full network model (Arruda and Boyce 1993a; Sweeney and Ward 1996; Matthews et al. 1997; Tomita 2000).

The present model, which has been outlined in Shepherd et al. (2006) and further extended in this thesis, implements the ISVs into the network model proposed by Wu and Van der Giessen (1993), which uses the exact treatment of an affine network model consisting of an orientation distribution of chains of freely rotating segments. While this method requires more computational resources than more common models based on a small number of chains connected in geometrically simplified forms, such as the three, four, and eight chain models (Flory and Rehner 1943; James and Guth 1943; Arruda and Boyce 1993b), the inclusion of an orientation distribution permits orientation dependent processes to be more fully addressed.

The ISVs are based on evolving microstructure attributes that have a direct effect on the mechanical properties of polymer systems. These ISVs include the amorphous chain orientation distribution (COD), $C_a(\theta,\phi)$; the crystalline segment orientation distribution (SOD), $S_c(\theta,\phi)$; the number density of statistical segments in the amorphous phase, N_a; the number density of statistical segments in the crystalline phase, N_c; the number density of crystal nuclei, $n_c(\theta,\phi)$; and the number density of entanglements, n_e. The CODs and SODs give the relative number density of statistical chain end-to-end vectors and the relative number density of chain segments, respectively, that are oriented relative to the polar, θ, and azimuthal, ϕ, coordinates of the global spherical coordinate system and are normalized such that the integration over all directions is equal to unity.

The amorphous COD, along with the stretch of the continuum, $\lambda(\theta,\phi)$, define the distribution of stretches for all of the chains in the system which affects the entropic response of the network model giving the orientation dependence of the stress. Since crystals and entanglements serve as constraints to intermolecular motions, the number densities of crystals and entanglements account for the number density of interconnects in the network model and also define the effective average number of segments in a chain. This implementation assumes that only the amorphous phase affects the network model. Therefore, an increase in crystallization, represented by the ratio of the number density of segments in the crystalline phase to the number density of segments in the amorphous phase, results in a reduction of the number density of amorphous segments between interconnects in a chain, thereby decreasing the entropy in the system.

It is noted that adoption of CODs and SODs, along with number densities of amorphous and crystalline segments, as ISVs does not imply fully dissipative processes;

in fact, entropic changes associated with orientation may occur in an equilibrium fashion if there is no evolution in the network interconnects (entanglement evolution or crystallization), and viscoelastic effects (time dependent bond rotations) are neglected.

The CODs and SODs need to evolve with network stretch, crystallization, and entanglement slippage in a manner that depends on the history of deformation. The CODs and SODs are implemented as two-dimensional matrices that represent a grid in the discretized θ and ϕ coordinates of a spherical coordinate system. Each cell of the matrix contains a value that represents the number density of statistical chains or segments that are oriented within that particular discrete range of directions.

The amorphous SOD, $S_a(\theta,\phi)$, which represents the orientation distribution of all of the amorphous segments in the system, is required for the crystallization calculations. The amorphous SOD is not an independent ISV as it is explicitly determined by the current state of the polymer network, i.e.,

$$S_a(\theta,\phi) = \frac{1}{4\pi}\sum_{\theta=0}^{\pi}\sum_{\phi=0}^{2\pi}\sum_{\theta'=0}^{\pi}\sum_{\phi'=0}^{2\pi} p_{seg}(\theta,\phi,\theta',\phi')C_a(\theta',\phi')\sin\theta'\,\Delta\theta'\,\Delta\phi', \tag{7.1}$$

where $\sin\theta'\,\Delta\theta'\,\Delta\phi'$ is the area represented by a cell in the discrete COD and $p_{seg}(\theta,\phi,\theta',\phi')$ is the probability of a segment having an orientation of (θ,ϕ) in a chain consisting of N segments with an end-to-end orientation of (θ',ϕ') and a stretch of $\lambda(\theta',\phi')$, given by (Kuhn and Grun 1942)

$$p_{seg}(\theta,\phi,\theta',\phi') = \frac{\mathcal{L}^{-1}\left(\dfrac{\lambda(\theta',\phi')}{\sqrt{N}}\right)\exp\left(\mathcal{L}^{-1}\left(\dfrac{\lambda(\theta',\phi')}{\sqrt{N}}\right)\beta(\theta,\phi,\theta',\phi')\right)}{\sinh\left(\mathcal{L}^{-1}\left(\dfrac{\lambda(\theta',\phi')}{\sqrt{N}}\right)\right)}. \tag{7.2}$$

Here, $\mathcal{L}^{-1}$ is the inverse of the Langevin function,

$$\mathcal{L}(x) = \coth(x) - \frac{1}{x} \tag{7.3}$$

and $\beta(\theta,\phi,\theta',\phi')$ is the cosine of the angle between a segment having an orientation of (θ,ϕ) and a chain with an end-to-end orientation of (θ',ϕ'), given by

$$\beta(\theta,\phi,\theta',\phi') = \sin\theta\sin\theta'\cos(\phi'-\phi) + \cos(\theta)\cos(\theta'). \tag{7.4}$$

Details of the morphological parameters, the nature of their evolution, and the manner in which they are incorporated into the model are provided in the following sections.

Crystal Nucleation

As the polymer system is deformed, the amorphous segments become more oriented towards the directions of deformation. This preferential alignment of the amorphous segments enhances the probability of thermally activated crystal nucleation. The orientation-dependent rate of nucleation is addressed through the thermodynamic nucleation model presented by Ziabicki and Jarecki (1985). This model is based on the Turnbull and Fisher (1949) rate of homogeneous nucleation which assumes that the segments are added to the forming nucleus in a stepwise manner. The Turnbull and Fisher expression was modified by Ziabicki and Jarecki to include the dependence of the number density nucleation rate on the orientation of the developing nucleus through the free energy parameter. The virtual number density nucleation rate, $\dot{n}_{cv}(\theta,\phi)$, which assumes that nucleation is not impeded by the reduction in the amount of amorphous segments available to be added to a forming nucleus as crystallization progresses or volume impingement, is given as

$$\dot{n}_{cv}(\theta,\phi) = \dot{n}_{c0} \exp\left(\frac{-\Delta F_n^*(\theta,\phi)}{k_B T}\right) \exp\left(\frac{-\Delta H^*}{k_B T}\right). \tag{7.5}$$

Here, $\Delta F_n^*(\theta,\phi)$ is the free energy change required to form a critically sized nucleus, ΔH^* is the heat of activation of the jump process at the nucleus interface, $\dot{n}_{c0}$ is the number density nucleation rate factor in the undeformed state, k_B is the Boltzmann's constant, and T is the absolute temperature. The actual number density nucleation rate, $\dot{n}_c(\theta,\phi)$, is dependent upon the ratio of virtual number density of crystalline segments to the total number density of segments in a particular orientation (Avrami 1941), i.e.,

$$\dot{n}_c(\theta,\phi) = \dot{n}_{cv}(\theta,\phi) \exp\left(\frac{-N_{cv}(\theta,\phi)}{N_a S_a(\theta,\phi) + N_c S_c(\theta,\phi)}\right), \tag{7.6}$$

where $N_{cv}(\theta,\phi)$ is the orientation dependent virtual number of segments in the crystalline phase; this is the number density of crystalline segments if volume exclusion is ignored and an inexhaustible source of non-crystalline segments were available. The total number density of crystal nuclei is simply the sum over the entire orientation space,

$$n_{c_{tot}} = \sum_{\theta=0}^{\pi} \sum_{\phi=0}^{2\pi} n_c(\theta,\phi) \sin\theta \Delta\theta \Delta\phi. \tag{7.7}$$

Deformation-induced orientation of the polymer chains, and hence the segments, decreases the entropy of the system and therefore reduces the amount of free energy required to form a nucleus of critical size. Ziabicki and Jarecki (1985) related the critical nucleation free energy, $\Delta F_n^*(\theta,\phi)$, to the orientation of polymer molecule segments within the vicinity of a nucleus via the change of configurational entropy induced by the change of the segmental distribution. The critical nucleation free energy of an oriented

polymer, assuming the nucleus is a rectangular parallelpiped, is given by (Hoffman and Lauritzen 1961)

$$\Delta F_n^*(\theta,\phi) = \frac{32\sigma_s^2\sigma_e}{\Delta f(\theta,\phi)^2}\ , \tag{7.8}$$

where σ_s is the side surface free energy of a crystal, σ_e is the end surface free energy of a crystal, and $\Delta f(\theta,\phi)$ is the bulk free energy in the deformed state. For the case of a single chain, the deformed bulk free energy is defined by Ziabicki and Jarecki (1985) to include the loss of a segment from its chain to a developing nucleus and the probability that a chain segment is at the same orientation as the developing nucleus, i.e.,

$$\Delta f(\theta,\phi) = \Delta f_0 + \frac{N_a kT}{N}\ln\left(p_{chain}\left(\lambda(\theta',\phi'),N\right)\right) - N_a k_B T \ln\left(p_{seg}(\theta,\phi,\theta',\phi')\right). \tag{7.9}$$

Here, $p_{chain}\left(\lambda(\theta',\phi'),N\right)$ is the probability that a chain with N segments has a stretch of $\lambda(\theta',\phi')$, and Δf_0 is the undeformed, randomly oriented bulk free energy (Hoffman and Lauritzen 1961), i.e.,

$$\Delta f_0 = \Delta h\frac{T\left(T_m - T\right)}{T_m^2}. \tag{7.10}$$

In this equation, Δh is the equilibrium enthalpy of crystallization and T_m is the melting temperature of the polymer. The probability of a chain having a specific end-to-end length is defined as (Wang and Guth 1952)

$$p_{chain}\left(\lambda(\theta,\phi),N\right)=C\left(\frac{\sinh\left(\mathcal{L}^{-1}\left(\frac{\lambda(\theta,\phi)}{\sqrt{N}}\right)\right)}{\mathcal{L}^{-1}\left(\frac{\lambda(\theta,\phi)}{\sqrt{N}}\right)\exp\left(\frac{\lambda(\theta,\phi)}{\sqrt{N}}\mathcal{L}^{-1}\left(\frac{\lambda(\theta,\phi)}{\sqrt{N}}\right)\right)}\right)^{N}\times\frac{\mathcal{L}^{-1}\left(\frac{\lambda(\theta,\phi)}{\sqrt{N}}\right)}{\frac{\lambda(\theta,\phi)}{\sqrt{N}}\sqrt{1-\frac{\lambda(\theta,\phi)^2}{N}-\frac{2\lambda(\theta,\phi)}{\sqrt{N}\mathcal{L}^{-1}\left(\frac{\lambda(\theta,\phi)}{\sqrt{N}}\right)}}},\qquad(7.11)$$

where C is a normalizing constant set equal to the inverse of $p_{chain}\left(1,N\right)$. The first term of Equation 7.11 is sufficient for large values of N, but the second term is also required for improved accuracy for the relatively low values of N that are often encountered in the application of this model for typical polymer systems.

The deformed bulk free energy averaged over all of the chains in the unit volume is defined as

$$\Delta f(\theta,\phi)=\Delta f_0 -N_a kT\ln\sum_{\theta=0}^{\pi}\sum_{\phi=0}^{2\pi}\sum_{\theta'=0}^{\pi}\sum_{\phi'=0}^{2\pi}p_{seg}(\theta,\phi,\theta',\phi')p_{chain}\left(\lambda(\theta',\phi'),N\right)^{-\frac{1}{N}}C_a(\theta',\phi')\sin\theta\Delta\theta\Delta\phi'.\qquad(7.12)$$

As crystal nucleation occurs, segments convert from the amorphous to the crystalline phase. The initial size of a crystallite is assumed to be equal to the critical size of a nucleus and will only increase in size due to growth, to be described later. The number density of amorphous segments that form nuclei is calculated from the number density of nuclei formed multiplied by the number of segments required to form a nucleus of critical size. The rate of change of the virtual number density of segments forming nuclei, where virtual represents the ideal growth without consideration of volume impingement or exhaustion of the supply of amorphous segments, is given by

$$\dot{N}_{nv}(\theta,\phi) = G(\theta,\phi)\dot{n}_{cv}(\theta,\phi)\,, \tag{7.13}$$

where $G(\theta,\phi)$ is the number of segments required to form a stable nucleus of critical size (George 1985), i.e.,

$$G(\theta,\phi) = -\frac{64\sigma_s^2\sigma_e N_{tot}}{\Delta f(\theta,\phi)^3}\,. \tag{7.14}$$

In (7.14), N_{tot} is given as the total number of segments per unit volume, i.e. $N_{tot} = N_a+N_c$.

The orientation dependence of the nucleation rates results in an orientation-dependent distribution of the number density of crystallites and the orientation dependence of the size of a stable nucleus results in an orientation-dependent distribution of the crystallite sizes. This nucleation model has the advantage that all of its parameters, except the pre-exponential nucleation rate constant, are based on measurable thermodynamic properties of the polymer.

Crystal Growth

Segments in the amorphous phase that are preferentially oriented with segments in the crystalline phase are more likely to be added to the crystals. As with nucleation, crystal growth entails a transfer of segments from the amorphous phase to the crystalline phase, leading to evolution of the amorphous and crystalline SODs. The kinetics of crystal growth are assumed to be similar to crystal nucleation, i.e.,

$$\dot{n}_g(\theta,\phi) = K_0 \exp\left(\frac{-\Delta F_g^*(\theta,\phi)}{k_B T}\right)\exp\left(\frac{-\Delta H^*}{k_B T}\right), \tag{7.15}$$

where $\dot{n}_g(\theta,\phi)$ is the rate of segments being added to a crystallite during growth, K_0 is the pre-exponential growth rate factor, and $\Delta F_g^*(\theta,\phi)$ is the critical free energy of stable growth on the surface of an established rectangular parallelepiped-shaped crystallite with a unit cell width *b*, i.e.,

$$\Delta F_g^*(\theta,\phi) = -\frac{4\sigma_s\sigma_e b}{\Delta f(\theta,\phi)}. \tag{7.16}$$

The time rate of change of the virtual number density of segments that attach to previously formed crystals depends upon the number density of crystallites aligned in the same orientation, i.e.,

$$\dot{N}_{gv}(\theta,\phi) = \dot{n}_g(\theta,\phi) n_{cv}(\theta,\phi). \tag{7.17}$$

The total rate of change of the number density of segments that enter the crystalline phase is then expressed as

$$\dot{N}_{cv}(\theta,\phi) = \dot{N}_{nv}(\theta,\phi) + \dot{N}_{gv}(\theta,\phi). \tag{7.18}$$

The quantity $N_{cv}(\theta,\phi)$ does not account for volume impingement or availability of amorphous segments, which become significant factors at the crystallinity levels that can be encountered with this model. The actual oriented crystallinity accounting for the limitations on crystal growth is given by

$$N_c S_c(\theta,\phi) = X_{max}\left(N_a S_a(\theta,\phi) + N_c S_c(\theta,\phi)\right)\left(1-\exp\left(\frac{-N_{cv}(\theta,\phi)}{N_a S_a(\theta,\phi) + N_c S_c(\theta,\phi)}\right)\right), \tag{7.19}$$

where X_{max} is the maximum allowable level of crystallinity. The rate of transfer of segments between the amorphous and crystalline phases is determined by

$$\dot{N}_c = \sum_{\theta=0}^{\pi}\sum_{\phi=0}^{2\pi}\frac{d}{dt}\left(N_c S_c(\theta,\phi)\right)\sin\theta\,\Delta\theta\,\Delta\phi, \tag{7.20}$$

with conservation of segments being maintained by

$$\dot{N}_a = -\dot{N}_c . \tag{7.21}$$

Since the amount of crystallization is determined quantitatively, the heat of crystallization can be calculated to determine the temperature increase in the material. The rate of temperature increase is determined by the rate of crystallization, i.e.,

$$\dot{T} = \frac{\dot{N}_c \Delta H_f}{N_{tot} c}, \tag{7.22}$$

where ΔH_f is the heat of fusion and c is the specific heat of the polymer. The effects of heat conduction also needs to be considered in the energy equation in the implementation of the model, of course, as (7.22) assumes adiabatic conditions.

The amorphous COD is assumed to not be affected directly by the phase change of segments, although the increase of the number density of crystallites and the decrease in the number of segments of the amorphous phase will have a measurable effect on the amorphous SOD by changing the number of segments per chain.

Entanglement Slippage

The evolution of entanglements is defined using the same relationships derived from molecular dynamics simulations as detailed in Chapter 6. This aspect represents an extension of the recently published work (Shepherd et al. 2006). Two processes were assumed, a rate dependent and a rate independent process. The rate independent process is considered to be solely dependent on the overall deformation of the material, i.e.,

$$n_{e_{base}} = n_{e_{init}} \exp\left(S(V-1)\right), \tag{7.23}$$

where $n_{e_{init}}$ is the initial number density of entanglements, S is a parameter that accounts for the magnitude of the dependency on deformation, and V is the overall stretch given by

$$V = \sqrt{\frac{1}{3}\sum_{i=1}^{3}\lambda_i^2}\,. \tag{7.24}$$

Here, λ_i are the principal stretches.

The rate-dependent reduction in the number density of entanglements is assumed to have a power law dependence on the stress and an Arrhenius dependence on the temperature, i.e.,

$$\dot{n}_{e_{slip}} = \dot{n}_{e0}\exp\left(-\frac{\Delta F_e}{k_B T}\right)\tau^q\left(\frac{n_{e_{base}} - n_{e_{slip}}}{n_{e_{base}}}\right), \tag{7.25}$$

where $\dot{n}_{e0}$ is an entanglement slippage pre-exponential constant, ΔF_e is the thermal activation energy, q is the stress power factor, and τ is the equivalent shear stress. The last term accounts for the reduced number of entanglements available for slippage as deformation progresses. The equivalent shear stress is defined by

$$\tau = \sqrt{\tfrac{1}{2}\boldsymbol{\sigma}' \cdot \boldsymbol{\sigma}'}\,, \tag{7.26}$$

where $\boldsymbol{\sigma}'$ is the deviatoric stress tensor.

The entanglement density is simply the difference between these two processes, i.e.,

$$n_e = n_{e_{base}} - n_{e_{slip}}\,. \tag{7.27}$$

The number density of chains in the system, n, is related to the number density of interconnects, which are represented by entanglements and crystals, and given by

$$n = 2\left(n_e + n_{c_{tot}}\right). \tag{7.28}$$

Framework of the Model

The framework presented by Boyce et al. (2000) is a thermodynamically admissible implementation that is valid for finite deformation and permits the inclusion of both intermolecular and network resistances, along with a viscous component to capture yielding associated with the intermolecular resistance. The overall deformation is assumed to consist of the effects of the entropic resistance of the network of polymer chains and the resistance between neighboring molecules. The deformation gradients associated with the network and intermolecular resistances, $\mathbf{F}_n$, and $\mathbf{F}_i$, respectively, are both set equal to the continuum deformation gradient, i.e.,

$$\mathbf{F} = \mathbf{F}_i = \mathbf{F}_n . \tag{7.29}$$

The deformation gradient associated with the intermolecular resistance is decomposed into an elastic component, $\mathbf{F}_i^e$, which accounts primarily for bond stretching and reversible change in bond angle, and an inelastic component, $\mathbf{F}_i^p$, which includes the remaining deformation as

$$\mathbf{F}_i = \mathbf{F}_i^e \mathbf{F}_i^p . \tag{7.30}$$

The left Cauchy Green tensor is determined from the deformation gradient associated with the network resistance, i.e.,

$$\mathbf{B} = \mathbf{F}_n \mathbf{F}_n^T . \tag{7.31}$$

The eigenvalues of the left Cauchy Green tensor give the square of the associated principal stretches. The corresponding eigenvectors are used to transform the principal network stress components back to the global system.

The stretches in any orientation are determined by (Wu and van der Giessen 1993)

$$\lambda(\theta,\phi)=\left(\frac{m_1^2}{\lambda_1^2}+\frac{m_2^2}{\lambda_2^2}+\frac{m_3^2}{\lambda_3^2}\right)^{-\frac{1}{2}}, \tag{7.32}$$

where λ_i are the principal stretches and the direction components are defined as

$$\begin{aligned} m_1 &= \sin(\theta)\cos(\phi) \\ m_2 &= \sin(\theta)\sin(\phi) \\ m_3 &= \cos(\theta) \end{aligned} . \tag{7.33}$$

The amorphous COD is defined by Wu and van der Giessen (1993) to be directly related the stretch in an affine manner, i.e.,

$$C_a(\theta,\phi)=\frac{\lambda(\theta,\phi)^3}{4\pi}. \tag{7.34}$$

In order to maintain the history dependence of the model on the deformation state, this relationship is implemented in its rate form, i.e.,

$$\dot{C}_a(\theta,\phi)=\frac{3\lambda(\theta,\phi)^2\dot{\lambda}(\theta,\phi)}{4\pi}. \tag{7.35}$$

It is likely that the crystalline phase included in this model would affect the deformation-induced change in the amorphous COD, and therefore this equation is approximate. After the amorphous COD is updated, the ISVs are then modified as described previously.

The network response is assumed to depend only on the number density and orientation of the amorphous statistical segments and not explicitly on the crystalline statistical segments, which are assumed to be locked within the crystals and therefore unable to directly contribute to the deformation of the network model. Since the ISV evolution equations involve the transition of statistical segments from the amorphous to the crystalline phase, the number of statistical segments between interconnects, N, must be updated prior to the network resistance calculation and is determined from the number

density of amorphous statistical segments in the model, N_a, and the number density of chains assuming a monodispersed molecular weight distribution, n, i.e.,

$$N = \frac{N_a}{n}. \tag{7.36}$$

The resulting modified version of the Wu and Van der Giessen (1993) network model is used to determine the stress arising from the resistance of the network to stretching, i.e.,

$$\hat{\sigma}_{n_i} = \frac{nk_BT}{4\pi}\sqrt{N}\sum_{\theta=0}^{\pi}\sum_{\phi=0}^{2\pi} C_a(\theta,\phi)\mathcal{L}^{-1}\left(\frac{\lambda(\theta,\phi)}{\sqrt{N}}\right)\lambda(\theta,\phi)m_i^2 \sin\theta\,\Delta\theta\,\Delta\phi - p\,, \tag{7.37}$$

where $\hat{\sigma}_{n_i}$ are the principal stress components and p is a hydrostatic stress parameter that is determined from the boundary conditions. The network stress components are rotated back to the global system and into tensor form, $\boldsymbol{\sigma}_n$.

As with the Boyce model, the total Cauchy stress is the sum of the stress due to network resistance and the stress due to intermolecular resistance, i.e.,

$$\boldsymbol{\sigma} = \boldsymbol{\sigma}_n + \boldsymbol{\sigma}_i\,. \tag{7.38}$$

The Cauchy stress due to intermolecular resistance is determined in the current configuration from the elastic Hencky strain as

$$\boldsymbol{\sigma}_i = \frac{1}{J}\mathbf{C}\cdot\left(\ln \mathbf{V}_i^e\right), \tag{7.39}$$

where $J = \det \mathbf{F}_i^e$, $\mathbf{C}$ is the rotated fourth rank elasticity tensor, and $\mathbf{V}_i^e$ is the left Cauchy Green tensor of the elastic deformation gradient, defined as

$$\mathbf{V}_i^e = \left(\mathbf{F}_i^e\mathbf{F}_i^{eT}\right)^{\frac{1}{2}}. \tag{7.40}$$

Following along the lines of the Boyce model, the flow rule is given as

$$\mathbf{D}_i^p = \dot{\gamma}^p \mathbf{N}, \tag{7.41}$$

where $\mathbf{D}_i^p$ is the rate of inelastic stretching, $\dot{\gamma}^p$ is the inelastic shearing rate and $\mathbf{N}$ is the direction defined in the current configuration by

$$\mathbf{N} = \frac{\mathbf{1}}{\sqrt{2}\tau_i}\boldsymbol{\sigma}_i'. \tag{7.42}$$

Here, $\boldsymbol{\sigma}_i'$ is the deviatoric portion of the Cauchy stress due to intermolecular resistance and τ_i is the equivalent shear stress due to the intermolecular resistance defined as

$$\tau_i = \left(\tfrac{1}{2}\boldsymbol{\sigma}_i' \cdot \boldsymbol{\sigma}_i'\right)^{\frac{1}{2}}. \tag{7.43}$$

For the inelastic shear strain rate, the double-kink Argon relaxation model (Argon 1973) was employed with a single relaxation time as in the Boyce et al. (2000) model, i.e.,

$$\dot{\gamma}^p = \dot{\gamma}_0^p \exp\left[-\frac{A}{k_B T}\left(1-\frac{\tau_i}{s}\right)\right], \tag{7.44}$$

where $\dot{\gamma}_0^p$ is a pre-exponential factor, A is the energy barrier to flow, and s is the athermal shear stress.

The velocity gradient associated with the intermolecular resistance is given in the current configuration by

$$\mathbf{L}_i^p = \mathbf{F}_i^e \dot{\mathbf{F}}_i^p \mathbf{F}_i^{p^{-1}} \mathbf{F}_i^{e^{-1}} = \mathbf{D}_i^p + \mathbf{W}_i^p, \tag{7.45}$$

where $\mathbf{L}_i^p$ is the inelastic velocity gradient which is separated into a symmetric part, $\mathbf{D}_i^p$, representing the inelastic rate of deformation and an anti-symmetric part, $\mathbf{W}_i^p$, that represents the inelastic spin tensor.

In order to complete the framework, the inelastic spin tensor must be specified. Pereda et al. (1993) define the inelastic spin tensor in the isoclinic intermediate configuration as a function of the principal stretch components, i.e.,

$$\left(\tilde{\mathbf{W}}_i^p\right)_{kl} = \frac{\lambda_k^2 + \lambda_l^2}{\lambda_k^2 - \lambda_l^2}\left(\tilde{\mathbf{D}}_i^p\right)_{kl}, \quad \lambda_k \neq \lambda_l, \quad k \neq l, \quad \left(\text{no sum on } k,l\right), \tag{7.46}$$

where

$$\mathbf{D}_i^p = \mathbf{F}_i^e \tilde{\mathbf{D}}_i^p \mathbf{F}_i^{e^{-1}}. \tag{7.47}$$

The rate of inelastic spin in the intermediate configuration is transformed into the current configuration according to

$$\mathbf{W}_i^p = \mathbf{F}_i^e \tilde{\mathbf{W}}_i^p \mathbf{F}_i^{e^{-1}}. \tag{7.48}$$

Implementation

The constitutive framework must be implemented using a numerical integration scheme. For purposes of numerical integration, the model only requires four external variables to be specified by the parent finite element analysis routine that calls the constitutive update subroutine: the continuum deformation gradient at the beginning of the time step, continuum deformation gradient at the end of the time step, temperature at the beginning of the time step, and time increment. Due to the boundary condition-dependent hydrostatic stress parameter, p, in the network stress equation (Eq. 7.36), this constitutive model cannot be directly implemented in many commercial codes, e.g. ABAQUS (2003), solely as a user defined constitutive model. As a result, a wrapper program was created to determine the evolution of the deformation gradient during the simulations and store the state variables. One method to generalize the model in order to

incorporate it into a general finite element analysis package is to assume that only the deviatoric component of the network stress should be accepted from (7.36) (Boyce et al. 2000).

The most significant disadvantage of the Wu and van der Geissen network model is the computational expense due to the numerical integration over the orientation distribution functions. As a result, reducing the size of the ODFs can have a dramatic effect on the overall computational time required. For the simulations performed in this research, two methods were implemented to reduce the size of the ODFs. First, the symmetry of uniaxial deformation, given random initial orientation distribution, permits only one eighth of the entire orientation space to actually be calculated. Second, the cells of the ODFs were defined such that the cells over which large changes in the density of the segments or chains cover a smaller area of the orientation space compared to the cells in the remaining orientation space. As a result, the cells are nonuniform in the amount of area of the orientation space that they cover. Large uniaxial deformation, in both compression and tension, results in large gradients of orientation density to occur in predictable small regions of the ODFs, assuming that the initial orientation distribution is uniform. The combination of these methods permits ODFs with only 12 divisions in each of the two spherical directions for a total of only 144 cells, while maintaining an integration accuracy of less than 1% of the network stress. In the case of uniaxial deformation, the ODFs can be further reduced to one dimension since gradients only occur over the θ-direction if the uniaxial deformation is applied in the z-direction.

Due to several interdependencies of the rate functions, the solution of the entire model requires the implementation of methods to solve the ordinary differential equations

(ODEs) and systems of nonlinear equations. Figure 7.1 shows a schematic of the implementation of the model for each time step.

F_0, F_1, Δt	**Provided by parent displacement-based FE code.**
F, $\mathbf{F}_i^p$, $\boldsymbol{C_a(\theta,\phi)}$, $\boldsymbol{T}$, $n_{e_{slip}}$ $\boldsymbol{n_{cv}(\theta,\phi)}$, $\boldsymbol{N_{cv}(\theta,\phi)}$,$\boldsymbol{N_c S_c(\theta,\phi)}$	**Extrapolated from previous step.**
$\boldsymbol{\lambda(\theta,\phi) = f(C_a(\theta,\phi))}$ $n_{e_{base}} = \boldsymbol{f}(\lambda(\theta,\phi))$ $\sigma_i = \boldsymbol{f}(\mathbf{F}_i^p, F)$ $\boldsymbol{N_a, N_c, S_c(\theta,\phi) = f(N_c S_c(\theta,\phi))}$	
$\boldsymbol{n_c = f(S_a(\theta,\phi), N_a)}$ $\boldsymbol{N = f}(n_{e_{slip}}, n_{e_{base}}, \boldsymbol{n_c, N_a})$ $\boldsymbol{S_a(\theta,\phi) = f(C_a(\theta,\phi), N, \lambda(\theta,\phi))}$ $\sigma_n = \boldsymbol{f}(n_{e_{slip}}, n_{e_{base}}, \boldsymbol{n_c, N, C_a(\theta,\phi)},\sigma_i)$	**Solve for $\boldsymbol{S_a(\theta,\phi)}$, N, $\boldsymbol{n_c}$ using Newton's method.**
$\dot{\mathbf{F}} = \boldsymbol{f}(F_0, F_1, \Delta t)$ $\dot{\mathbf{F}}_i^p = \boldsymbol{f}(\mathbf{F}_i^p, F)$ $\dot{C}_a(\theta,\phi) = \boldsymbol{f}(\dot{\mathbf{F}}, F)$ $\dot{n}_{e_{slip}} = \boldsymbol{f}(\sigma_i, \sigma_n, n_{e_{slip}}, n_{e_{base}})$ $\dot{n}_{cv}(\theta,\phi) = \boldsymbol{f(N_a, C_a(\theta,\phi), N, \lambda(\theta,\phi))}$ $\dot{N}_{cv}(\theta,\phi) = \boldsymbol{f(N_a, C_a(\theta,\phi), N, \lambda(\theta,\phi))}$	**Determine rates to find values for the next time step.**
$\boldsymbol{d(N_c S_c(\theta,\phi))/dt = f(N_a, N_c, S_a(\theta,\phi)}, \dot{S}_a(\theta,\phi))$ $\dot{S}_a(\theta,\phi) = \boldsymbol{f}(\dot{C}_a(\theta,\phi), \boldsymbol{C_a(\theta,\phi), \lambda(\theta,\phi), N}, \dot{N})$ $\dot{N} = \boldsymbol{f}(d(\boldsymbol{N_c S_c(\theta,\phi)/dt}, \dot{S}_a(\theta,\phi), n_{e_{slip}}, n_{e_{base}}, \boldsymbol{n_c},$ $\dot{n}_{e_{slip}}, \dot{n}_c, \dot{C}_a(\theta,\phi), \boldsymbol{N_a})$ $\dot{n}_c = \boldsymbol{f}(d(\boldsymbol{N_c S_c(\theta,\phi)/dt}, \dot{S}_a(\theta,\phi), \boldsymbol{S_a(\theta,\phi), N_a})$	**Solve for $\boldsymbol{d(N_c S_c(\theta,\phi)/dt}$, $\dot{S}_a(\theta,\phi)$, $\dot{N}$, $\dot{n}_c$ using Newton's method.**

Figure 7.1 Schematic of the numerical implementation for each time step.

Two groups of equations form nonlinear systems of equations. These systems are solved at each time step using a globally convergent Broyden's method algorithm with line searches (Press et al. 1996). The model is integrated using the fifth-order Cash-Karp Runge-Kutta method with adaptive step sizes (Press et al. 1996). This method proved to be superior to lower order methods in both computational resource requirements and the ability to converge at high strains.

Results

To demonstrate the effectiveness of the model to simulate actual polymer deformation, the model was compared to experimental results at several strain rates and temperatures just above the glass transition temperature. The polyethylene homopolymer modeled with the molecular dynamics simulations was not used to validate the constitutive model because of the lack of useful amorphous experimental data to validate the model results. The low glass transition temperature of the ideal polyethylene homopolymer precluded availability of sufficient low crystallization experimental data in the literature necessary to fully test the constitutive model. Instead, a common semi-crystalline polymer was considered, polyethylene terephthalate (PET).

Comprehensive experiments covering all of the capabilities of this model, i.e., temperature- and rate-dependent stress, orientation, and crystallinity versus strain, were not found in a single publication. Therefore, two sets of experimental results were used to evaluate the model. Clauss and Salem (1992) measured stress-strain, orientation, and crystallinity of PET at a single temperature just above the glass transition temperature, 90°C. This uniaxial tension experiment included measurements at two nominal strain

rates, $0.56s^{-1}$, and $0.01s^{-1}$. Llana and Boyce (1999) provided uniaxial compression stress-strain data at multiple true strain rates and temperatures. Also included were relative final crystallinity measurements. The model was implemented as discussed previously. Boundary conditions were set up to simulate the experiments. Heat generation and transfer were not included as the experimental details pertaining to heat conduction were not specified in the literature.

Many of the model parameters were taken from the literature. The remaining parameters were fit to all of the experimental data using the covariance matrix adaptation (CMA) evolutionary algorithm scheme (Hansen and Ostermeier 2001) as implemented in the OpenBeagle framework (Gagne and Parizeau 2002). The values for all of the parameters are included in Table 7.1.

Table 7.1 Model parameters for both experiments (Clauss and Salem 1992; Llana and Boyce 1999).

Parameter	Llana and Boyce	Clauss and Salem	Source
E	40 MPa - 1.2 MPa K^{-1}(T - 353 K)		(Boyce et al. 2000)
N	0.49		(Boyce et al. 2000)
S	0.15 E/(2(1+ν))		(Boyce et al. 2000)
A	3.98×10^{-20} J		Fit
$\dot{\gamma}_0$	7.21 s^{-1}		Fit
N_a	8.05×10^{20} cm^{-3}		(Aharoni 1983)
N	6.0	5.6	Fit
S	04.42	0.023	Fit
$\dot{n}_{e0}$	3.81×10^{64} $cm^{-3}s^{-1}$	3.87×10^{36} $cm^{-3}s^{-1}$	Fit
ΔF_e	5.41×10^{-19} J	2.00×10^{-19} J	Fit
Q	2.71		Fit
Δh	-180 J/cm^3		(Palys and Phillips 1980)
T_m	553 K		(Palys and Phillips 1980)
ΔH^*	9.39×10^{-20} J		(Gregory and Watson 1970)
B	5.0×10^{-8} cm		(George 1985)
σ_s	10.2×10^{-7} J/cm^2		(Palys and Phillips 1980)
σ_e	190×10^{-7} J/cm^2		(Palys and Phillips 1980)
$\dot{n}_{c0}$	2.59×10^{50} $cm^{-3}s^{-1}$	6.78×10^{49} $cm^{-3}s^{-1}$	Fit
K_0	2.08×10^{20} s^{-1}	9.53×10^{18} s^{-1}	Fit
X_{max}	0.25		Fit

The crystallisation kinetics only require three parameters to be fit to the experimental data, $\dot{n}_{c0}$, K_0, and X_{max}. The remaining parameters (Δh, T_m, ΔH^*, b, σ_s, σ_e) are thermodynamic properties that can be found in the literature or possibly through the use of atomistic modeling methods.

The amorphous PET used in the experiments had a density of 1.339 g/cm^3, which is equivalent to 4.2×10^{21} monomers per cm^3. The number density of statistical segments, N_a, is determined by scaling the number density of monomers by the ratio of the Kuhn length, 11.1Å (Aharoni 1983), to the average monomer length, 2.135 Å (Aharoni 1983).

The model correlates well to the experimental uniaxial stress-strain data reported by Clauss and Salem (Figure 7.2). The model becomes unstable at the high strains where the data terminate. This instability is due to reaching the locking strain at this point. When the square root of the number of segments per chain approaches the stretch of the material, the rubber elasticity portion of the model approaches an infinite stress. As shown in Figure 7.3, this condition is met at the point at which the model stops. Normally, as the locking strain is approached, the stress becomes high enough to substantially increase the rate of entanglement slippage due to its power law dependence on stress. The loss of entanglements increases the number of segments per chain which increases the strain at which the locking behaviour occurs. This interplay between entanglement slippage and the locking strain indicates an interesting mechanism of intermolecular interactions at high strains where sufficient strain energy is required to overcome these barriers to molecular motion.

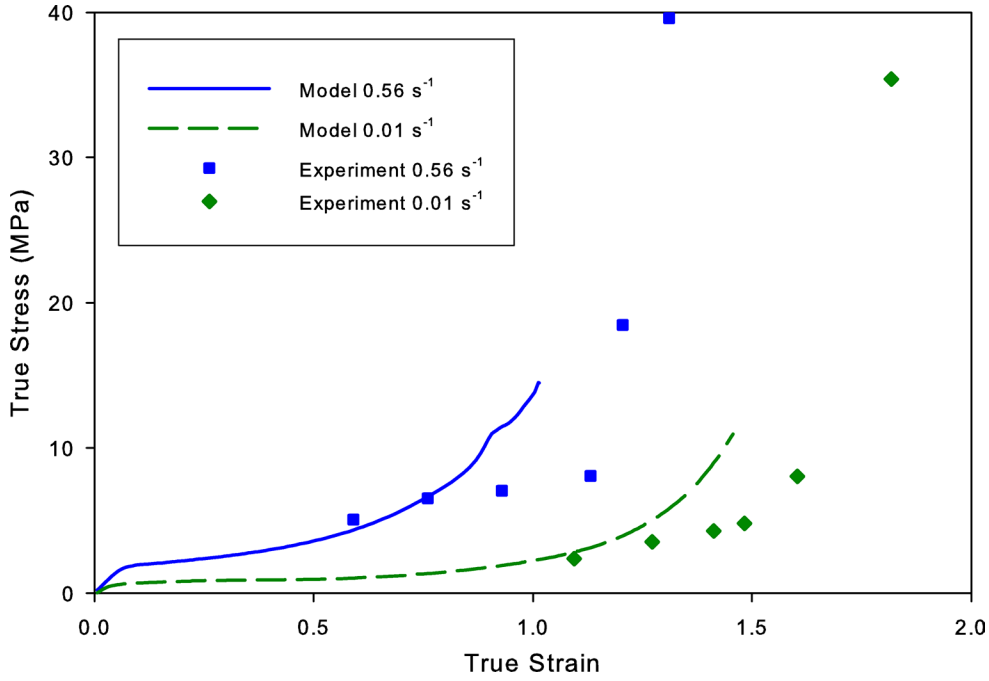

Figure 7.2 Stress-strain curves for the continuum model and experimental data at 90°C.

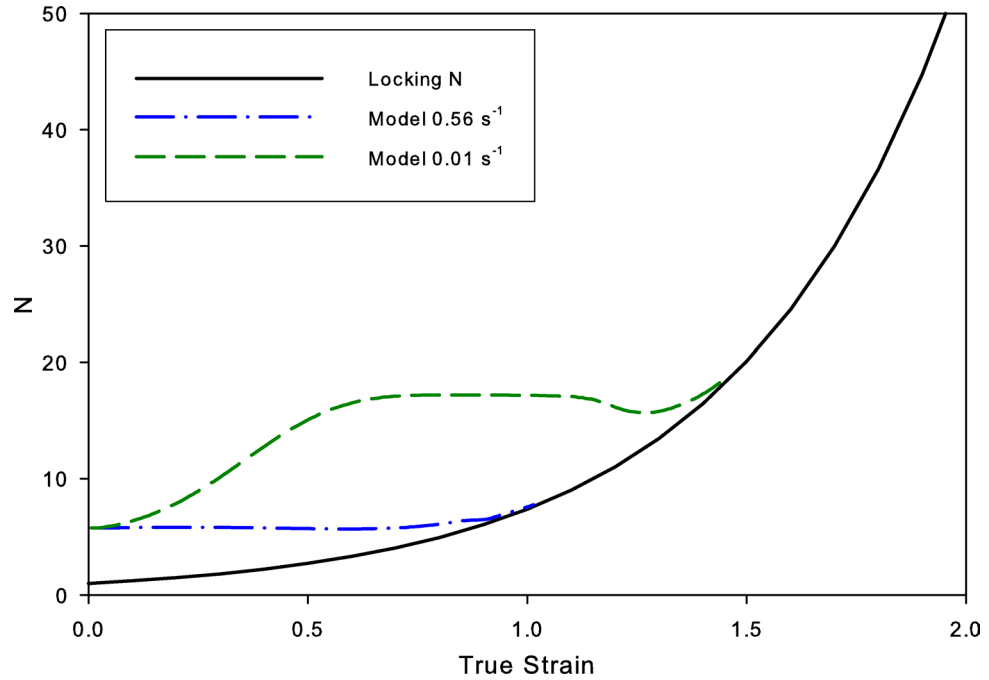

Figure 7.3 The number of segments per chain as a function of strain for the continuum model and the number of segments per chain that result in locking behavior at 90°C.

The predicted overall crystallinity as a function of strain (Figure 7.4) demonstrates several characteristics of the model. The lack of model data at high strains is a result of the previously covered strain-locking behaviour. The model is able to correctly reproduce the relative shapes of the crystallisation curves and points at which crystallisation commences. However, the model gives high rates of crystallization than the experiments. This discrepancy is likely due to a shortcoming in the crystallization kinetics. While the model does account for the overall maximum percentage of crystallization, it only does so at each orientation, independently. The model assumes that all of the amorphous segments oriented in the direction of crystal growth are available for addition to the crystal. In an actual polymer, amorphous segments oriented in different directions and crystals forming and growing in different directions will hinder or completely separate the aligned amorphous segments.

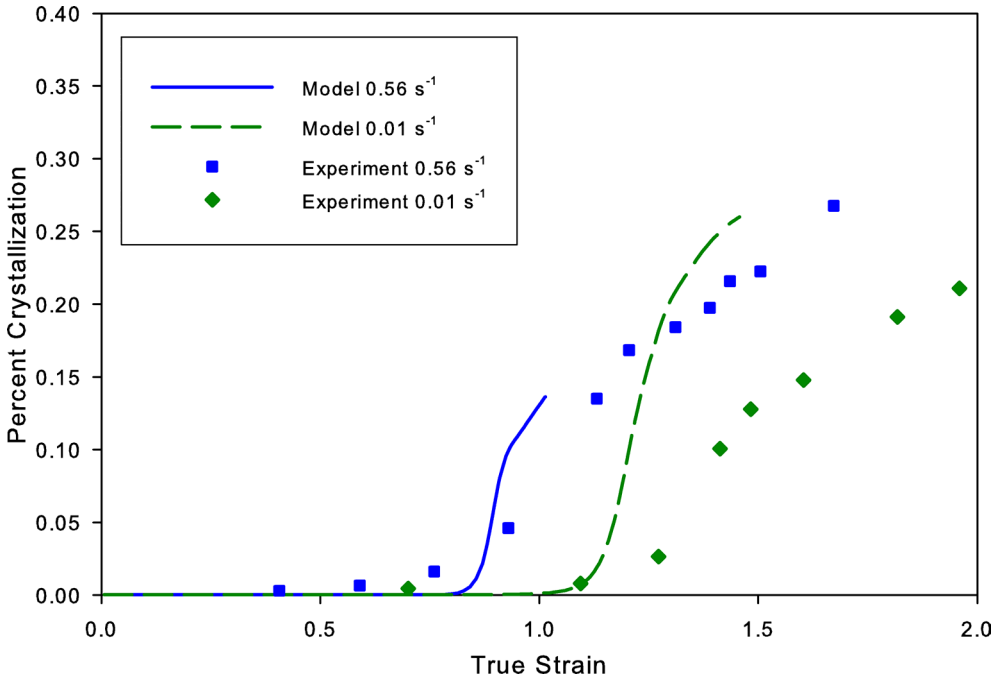

Figure 7.4 Overall crystallinity as a function of strain for the continuum model and experimental data at 90°C.

The average size of the crystals increases with deformation and strain rate (Figure 7.5). These results indicate that the growth of a crystal is not as dependent on orientation as is the nucleation process. Since nucleation requires a critical number of segments to be aligned in the same direction, while crystal growth can be performed in much smaller increments, it is likely that these results simulate actual behavior. The reduction in the rate of crystal growth at the slower strain rate near a strain of 0.75 is a result of the amorphous segments in the direction of orientation becoming consumed to the point that an insufficient number density of amorphous segments exists to maintain the previous growth rate. The subsequent increase in growth rate coincides with the strain hardening of the polymer. This significant hardening increases the number of amorphous segments aligned in the direction of deformation, allowing more segments to be available for growth.

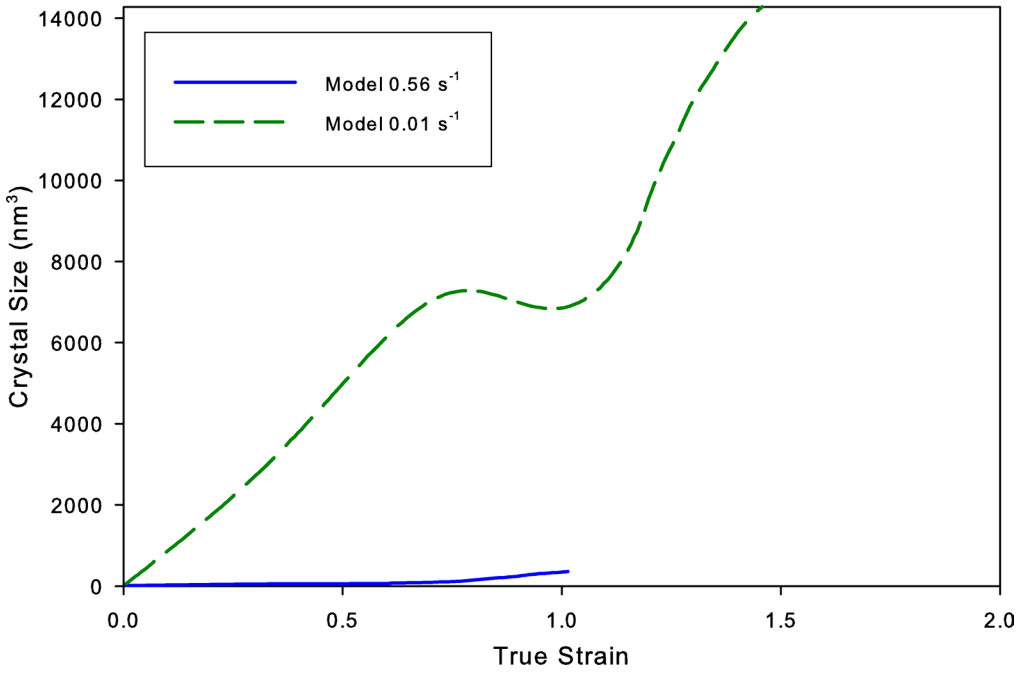

Figure 7.5 Average crystal size as a function of strain for the continuum model and experimental data at 90°C.

The primary driver for the increase in nucleation rate is the increase in orientation. The slowest nominal strain rate, $0.01s^{-1}$, permits over an order of magnitude more time for nucleation to occur than at the faster rate, $0.56s^{-1}$. As would be expected, the slower rate results in a much higher nucleation rate at low strains than the faster rates (Figure 7.6). This trend is reversed as deformation continues and the orientation dependence overcomes the difference in time. Also of interest is that the number density of nuclei is always orders of magnitude less than the number density of entanglements. This observation indicates that the entanglements have a greater effect on constraining the network of chains than the nuclei. Recent experimental evidence comparing the mechanical behavior of PET and a non-crystallizing copolymer PETG (Dupaix and Boyce 2005) indicates that strain induced crystallization is not significantly responsible for the strong hardening behavior of PET as also demonstrated with this model.

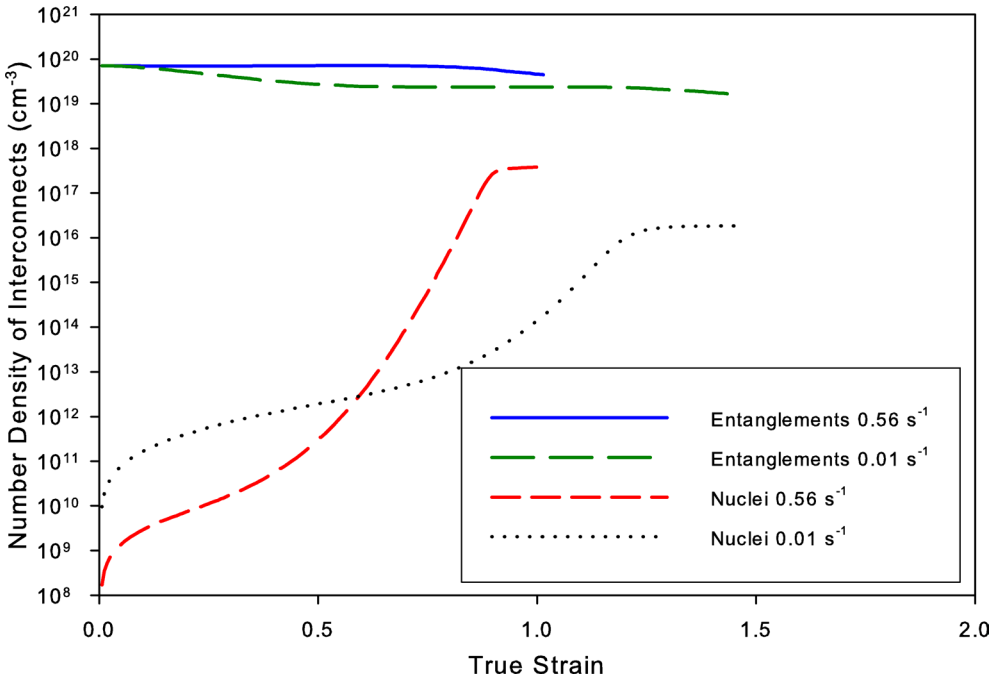

Figure 7.6 Number densities of crystals and entanglements as a function of strain for the continuum model and experimental data at 90°C.

The model accurately represents the experimentally measured amorphous segment orientation distribution (Figure 7.7). The Herman's orientation, P_2, is determined over the entire orientation space, i.e.,

$$P_2 = \frac{3\left(\sum_{\theta=0}^{\pi}\sum_{\phi=0}^{2\pi} S_a(\theta,\phi)\cos^2\theta\sin\theta\Delta\theta\Delta\phi\right)-1}{2}. \tag{7.49}$$

The combination of the orientation and crystallization results indicate that the highly orientation dependent crystallization kinetics employed in the model are valid.

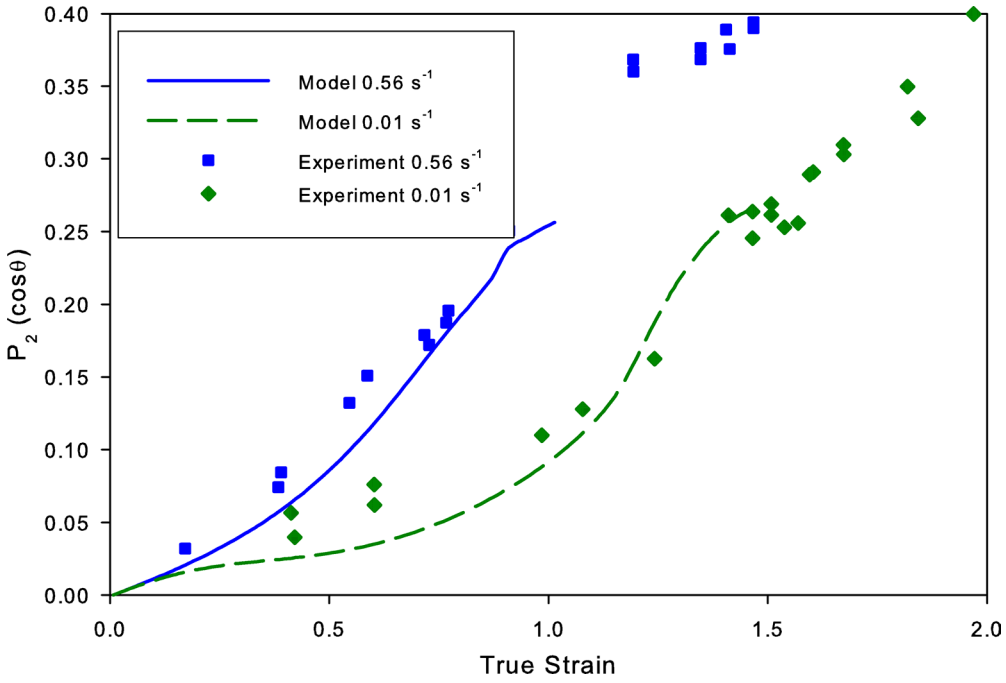

Figure 7.7 Orientation development of the amorphous segments as a function of strain for the continuum model and experimental data at 90°C.

To determine the accuracy of the model over a wider range of strain rates and temperatures, the model was fit to the experimental data provided by Llana and Boyce. True stress-strain curves from the model and experiments for temperatures of 90°C, 100°C, and 105°C at a strain rate of $-0.1s^{-1}$ are provided in Figure 7.8. As the temperature is increased, the rate of entanglement slippage becomes greater, reducing the hardening rate. Stress-strain results from the model and experiments for strain rates of $-0.005\ s^{-1}$, $-0.1\ s^{-1}$, and $-1.0\ s^{-1}$ at 100°C are provided in Figure 7.9. As the strain rate is increased, the hardening rate is likewise increased due primarily to the lack of time for entanglement slippage to become significant and the increase in stress induced crystallization. The model is able to capture the experimental data exceptionally well. The stress at which yielding occurs and the shape of the yielding behaviour shows a

discrepancy between the model and experiment. The single relaxation time model is the likely culprit. Implementing a multi-relaxation time model similar to Hasan and Boyce (1995) or Dooling et al. (2002) could correct this deficiency. However, these relaxation models require more parameters to be fit and increase the computational cost of solving the model. If large strain behaviour is of interest, then the discrepancies at the very low strain will not have a significant effect on the results.

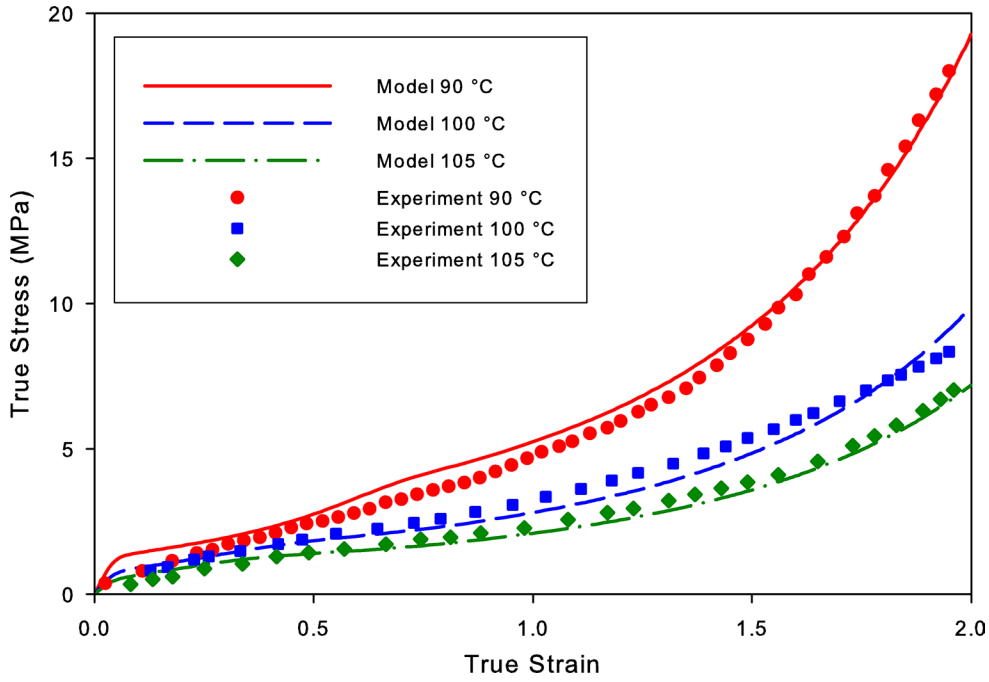

Figure 7.8 Temperature dependence of true stress-strain behavior at a true strain rate of -0.1s^{-1} for the continuum model and experimental data.

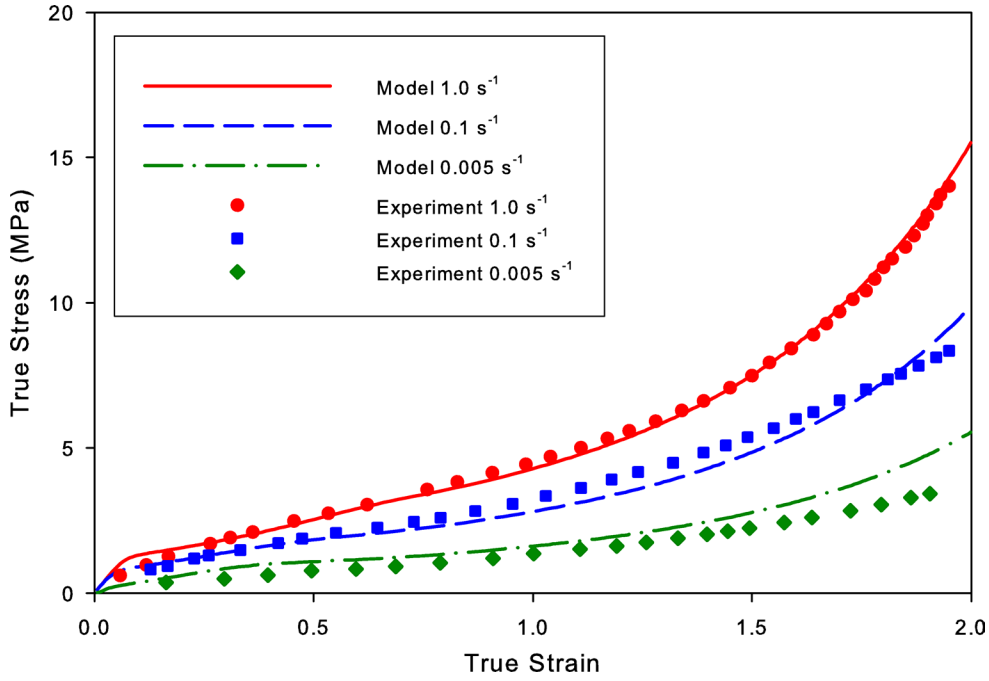

Figure 7.9 Rate dependence of true stress behavior at a temperature of 100°C for the continuum model and experimental data.

The results of the network model evaluation performed in Chapter 6 indicated that the entanglement evolution equations might be capable of simulating the visco-elastic portion of the deformation behavior. To determine the ability of the entanglement evolution equations to simulate the visco-elastic behavior, the intermolecular resistance portion of the model was disabled, i.e., the calculations related to $\mathbf{F}_i$ and $\boldsymbol{\sigma}_i$ were skipped. The model was then fit to the Llana et al. experimental data as before. The Llana et al. experimental data was chosen since it captures the yielding behavior at lower strains. The stress-strain behavior is modeled well for different temperatures (Figure 7.10) and true strain rates (Figure 7.11). The results from the model show the yielding occurring at slightly higher strains than the experimental data. Additionally, the yielding predicted by this model is not as rate- or temperature-dependent as the experimental data. However,

the post-yield behaviors are modeled nearly as well as with the model including the visco-elastic component.

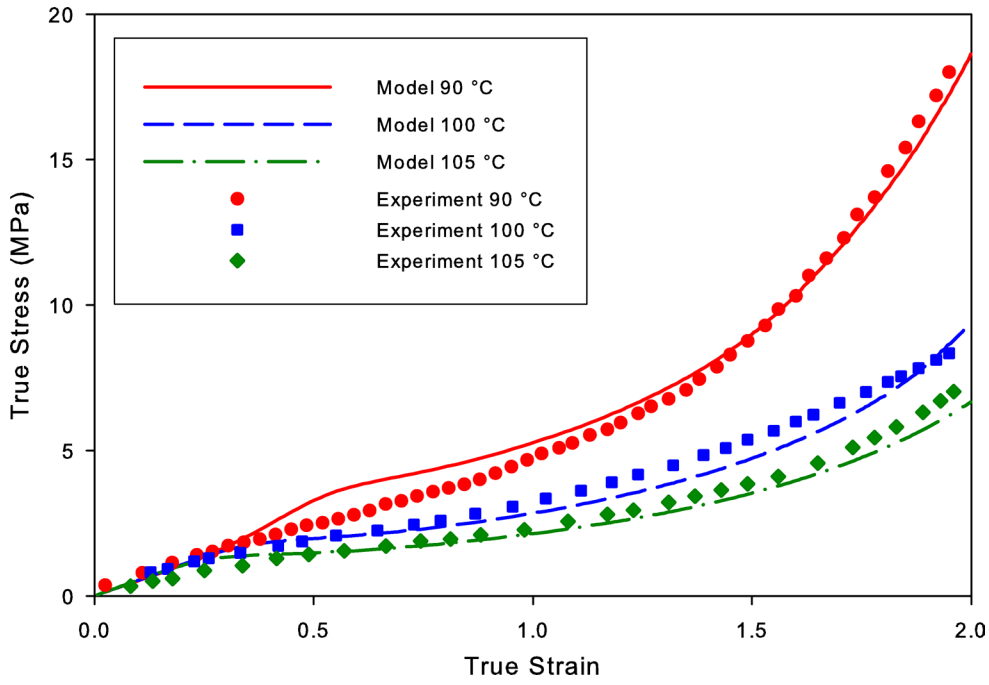

Figure 7.10 Temperature dependence of true stress-strain behavior at a true strain rate of -0.1s^{-1} for the continuum model and experimental data.

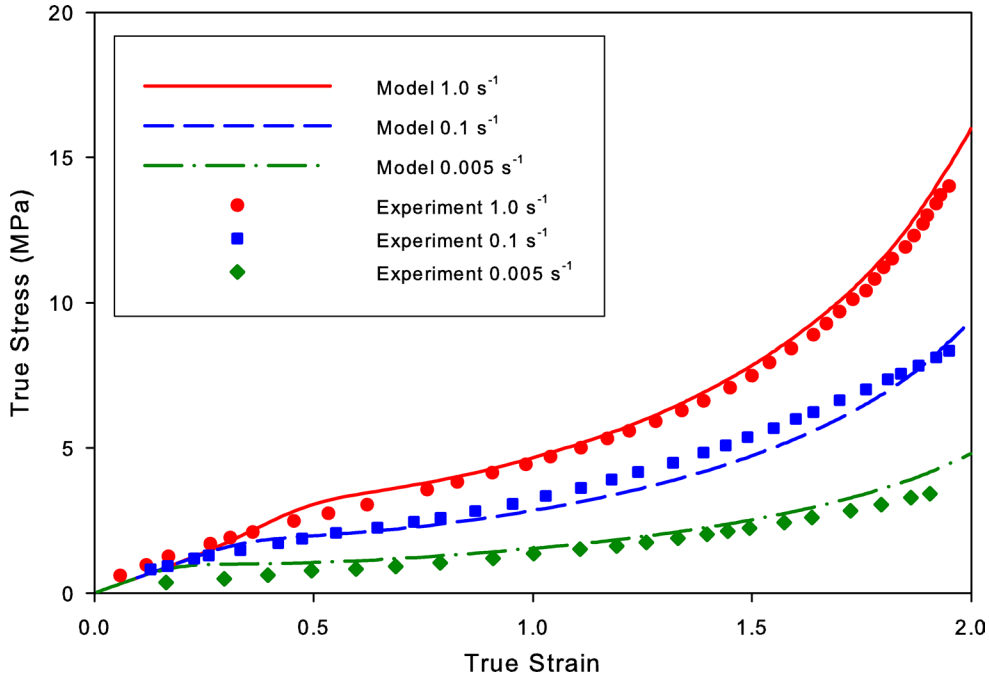

Figure 7.11 Rate dependence of true stress-strain behavior at a temperature of 100°C for the continuum model and experimental data.

A significant advantage of the model without the visco-elastic component is that five fewer model parameters are required, particularly parameters that must be fit to experimental data (Table 7.2). Furthermore, if a non-crystallizing polymer is to be modeled, the crystallization related parameters would no longer be needed leaving only six parameters for the entire model. It is also possible that the entanglement models could be enhanced to better model the yielding behavior. While this enhancement will likely require the use of additional parameters, the actual material mechanisms may be better modeled.

Table 7.2 Model parameters for both experiments (Clauss and Salem 1992; Llana and Boyce 1999) for the case without the intermolecular resistance component.

Parameter	Llana and Boyce	Source
N_a	8.05×10^{20} cm^{-3}	(Aharoni 1983)
N	3.00	Fit
S	3.98	Fit
$\dot{n}_{e0}$	3.42×10^{61} cm^{-3}s^{-1}	Fit
ΔF_e	4.98×10^{-19} J	Fit
Q	2.39	Fit
Δh	-180 J/cm^3	(Palys and Phillips 1980)
T_m	553 K	(Palys and Phillips 1980)
ΔH^*	9.39×10^{-20} J	(Gregory and Watson 1970)
B	5.0×10^{-8} cm	(George 1985)
σ_s	10.2×10^{-7} J/cm^2	(Palys and Phillips 1980)
σ_e	190×10^{-7} J/cm^2	(Palys and Phillips 1980)
$\dot{n}_{c0}$	1.73×10^{47} cm^{-3}s^{-1}	Fit
K_0	1.06×10^{21} s^{-1}	Fit
X_{max}	0.48	Fit

Conclusions

A constitutive model has been presented to characterize the mechanical behavior of semi-crystalline polymers as well as major morphological mechanisms in polymers during deformation. The mechanisms include entanglement slippage, orientation, and strain-induced crystallization, comprising both crystal nucleation and crystal growth. The combination of these separate mechanisms has been shown to correctly simulate the trends of observed complex experimental mechanical behavior. The simulated mechanical behavior agrees very well with experimental evidence (Clauss and Salem 1992; Llana and Boyce 1999) over the temperatures and strain rates evaluated. Unlike other models that simulate the mechanical behavior of semi-crystalline polymers (Buckley and Jones 1995; Adams et al. 2000; Boyce et al. 2000), the model presented

here also tracks the development of morphology. The evolution of the ISVs during deformation agree reasonably well with experimental evidence, with the relaxation resulting from entanglement slippage dominating the effects of strain-induced crystallization, as suggested from experimental evidence (Salem 1992a).

The model is shown to perform well at simultaneously fitting transient crystallization, orientation, and stress-strain data. This performance indicates that this particular implementation of thermodynamically derived crystallization models and entanglement evolution equations into a rubber elasticity model can represent actual material behavior well. The ISVs implemented in the model have a direct relation to quantitative morphological attributes and can be queried to determine the morphological state of the material at any point during deformation. This aspect of the model makes it a very powerful tool to not only determine the mechanical behavior of the material but also to investigate and predict the evolution of morphology during deformation, permitting the optimization of manufacturing processes for desired morphologies. In many commercial applications the resulting morphology of the polymer is as important as its mechanical behavior. Some of these applications include beverage bottles and films where the permeation of gases through the polymer is dependent upon the amount of crystallization and orientation, which can be characterized by this model. The direct correlation of the ISVs with morphological entities could facilitate the design of new polymer systems, where the material designer can specify molecular characteristics that would have specific effects on certain ISVs.

The ISVs evolve in a history dependent manner and have the capability of describing complete anisotropy of the polymer system. These attributes allow the model

to predict complex deformation modes and histories. In this research, only the monotonic initial uniaxial deformation was studied. Further work should investigate the model's ability to simulate more complex deformation modes such as biaxial, relaxation behavior after deformation, and complex deformation histories that include combinations of loading and unloading. To further evaluate the abilities of the model, additional orientation and crystallization data taken at different temperatures as well as rates would be useful.

Though a large number of model parameters must be defined, many of these are fundamental properties of the polymer and can be found in the literature for most common polymers. However, the remaining parameters are mostly very interdependent and it could be difficult to determine accurate values for these constants without performing a significant number of experiments, especially for polymers for which thermodynamic properties have not been previously characterized. It is also difficult to validate the material constants and the evolution of the ISVs due to the lack of experimental data regarding the evolution of crystal nuclei, crystal size, and entanglement slippage during strain-induced crystallization. As shown in this research, another approach is to use molecular models to derive these parameters. The derivation of the entanglement evolution equations from atomistic simulations and implementation into the continuum model shows how this length scale bridging can be performed. The correspondence of the ISVs with morphological entities makes it feasible to completely determine all of the model parameters from molecular modeling. This capability would permit the determination of mechanical behavior of the polymer at the continuum scale

without even physically constructing the polymer, which represents an ultimate goal of this research.

CHAPTER 8

CONCLUSIONS

The objective of this research was to develop models and methods to bridge atomistic and continuum models of deformation processes in polymer systems. Of particular interest was the identification and tracking of morphological entities at the atomistic level and the extrapolation of these results into the continuum level. The research presented here has met this goal by providing a foundation for multi-scale modeling of deformation processes in semi-crystalline polymers. Atomistic tools and methods have been developed that integrate with a continuum model resulting in a multi-scale model framework. The successful bridging of entanglement evolution from atomistic to continuum models is a specific application of this process that serves as a direction for similar bridging of other morphological entities.

Significance

This research has yielded a much clearer understanding of the influence of the underlying structures on mechanical behavior through the development of significantly more accurate material models based on the nanoscale attributes of polymers, particularly the evolution of entanglements. The ultimate goal of the research was to develop methods to determine macroscale model parameters largely from molecular level models, reducing the need for experimental derivation of these parameters while providing additional capability for material design. Significant steps toward this goal have been completed. Specifically, the following contributions have been made:

- A thorough investigation of the application of molecular dynamics methods to simulating the deformation of polymers has been completed. The sensitivity of the molecular dynamics method to the various method parameters and polymer system initial configurations has been determined. The optimal parameters in regards to accuracy and computational efficiency were selected as well as the number of trials required for consistency of results. The confirmation of the molecular dynamics method was essential in ensuring that the remaining atomistic simulations can be trusted.
- An initial configuration algorithm has been developed which generates more realistic configurations and requires less computational resources than current methods. This method permits fine control over the properties of the polymer system such as end-to-end lengths and overall orientations of the chains, distribution of RIS states, and polydispersity. Additionally, this method can ensure a low energy configuration with relatively even density. Complete control over the topology of cross-linked networks is possible along with the creation of ring molecules and other formations. Development of this algorithm was instrumental in creating the initial configurations near equilibrium as required for this research and particularly the completely cross-linked systems at high densities used in the network model comparisons.
- A thorough investigation of the application of time acceleration methods to large polymer systems has been completed. A successful method was not found that would permit the investigation of long time scale events due to the large number of nearly simultaneous transitions violating the assumptions that the acceleration

methods were based on. However, the results from this investigation show the potential of this method to enhance the computational efficiency of molecular dynamics simulations. Additionally, directions for further research to try and overcome the limitations in the accelerated dynamics methods have been proposed.

- An original method of computationally defining entanglements by their mechanical function instead of their geometry has been presented. This method of evaluating the bond forces yields consistent qualitative results that give some insight into the evolution of entanglements.
- The ability of rubber elasticity models to correlate with the behavior of actual polymers through atomistic studies has been confirmed. The correlation between an ideal rubber elasticity model and an atomistically modeled polymer was found by linking the parameters of the network model to the molecular structure and interactions of the polymer system. From this correlation, the evolution of entanglements was determined from which equations were derived to model this behavior.
- A constitutive model for semi-crystalline polymers for which the internal state variables directly relate to the underlying structures of the material was enhanced to much more accurately simulate experimental evidence. Most significantly, the evolution of entanglements is guided by molecular dynamics investigations. Additionally, the oriented crystallization kinetics provided by Ziabicki and Jarecki (1985) for the history independent, uniaxial case was enhanced to a general implementation in three dimensions with history dependence.

These contributions will have a significant impact in the field of polymer mechanics by shedding light on the relationship between nanoscale structures and macroscopic behavior as well as providing methods to quantitatively link these scales.

For purposes of materials design, the relationships obtained between nanoscale morphology and the resulting behavior of polymers can support optimization and robust design methods to determine the morphological compositions for specific end uses. Furthermore, the determination of ISV model structures and parameter values based on atomistic models would facilitate prediction of mechanical behavior and morphology evolution of novel polymers without the need to synthesize them. Additionally, these methods, in conjunction with parametric studies, will permit the robust design of novel polymers that will meet desired mechanical behavior. Thus, the main thrust of this proposal is to advance the utilization of current atomistic models to incorporate information into molecular-based ISV models.

Suggested Future Work

The research presented here has cumulated in the development of methods and models to link atomistic and continuum models. The next steps in this research should focus on further implementation of these methods to other morphological entities and a more thorough validation of these methods with experimental evidence. The primary focus of this research was on the evolution and effect of entanglements and the interaction of polymer chains across the length scales. The next morphological entities that should be studied are crystals.

Through experiments, it is very difficult to separate the nucleation and growth from the overall development of crystallization due to the difficulty of measuring the transient development of these nanoscale structures. As a result of this experimental limitation, molecular models could be used to study the initiation and development of crystallization. The rate, temperature, and orientation dependence of both nucleation and growth could be compared to existing thermodynamics-based crystallization models for compatibility. By investigating the correlation between the molecular model results and existing macroscopic material behavior models, the fitness of the macroscopic model to capture the molecular behavior can be determined. If the fit is good, then appropriate macroscopic model parameters can possibly be obtained directly from the atomistic models. Otherwise, modifications to these macroscopic models or development of a novel model may be required.

Because of the time required for nucleation events to occur in the dense polymer systems of interest here, time accelerating methods will need to be implemented in the crystallization studies. Completely amorphous configurations will be modeled without any applied deformation to determine the unoriented nucleation rate. Replicas of the initial configuration of the amorphous system could be uniaxially deformed to various stretches and hence various levels of orientation. Fast deformation rates could be used to limit the amount of crystallization during stretching. The system would then be held at the final stretch while crystallization occurs.

To determine both nucleation and growth rates, the number and size of the crystallites could be measured using the orientation order parameter method of Ko et al. (2004). The orientation distribution of the monomers would also be determined during

the crystallization measurements. The data from these measurements could then be used to evaluate the fitness of the crystallization model (Ziabicki and Jarecki 1985) implemented in the continuum model.

Due to practical limitations with experiments on non-crystalline polyethylene homopolymers, there is not sufficient data to determine the accuracy of linking entanglement evolution across the length scales. A next step would include the simulation of more complex polymer structures that do not crystallize so easily. For example, linear-low density polyethylene copolymer is relatively simple in structure and adequate experimental data is available to validate the methods proposed in this research. The initial configuration generation software would only need minor modifications to generate the necessary structures. Potentials for the different monomers of this polymer and their parameters would need to be determined and validated for the molecular dynamics simulations. Another material that has a substantial amount of macroscale experimental data and reasonable atomistic model development is polyethylene terephthalate (PET). The structure of PET is much more complex than linear-low density polyethylene and would be a good candidate for further validation of the multiscale methods proposed in this research.

The bridging of the morphological processes over the many orders of magnitude of time scales needs to be evaluated further. While the accelerated dynamics methods do not seem to be able to bridge significant time scales, other methods should be investigated such as coarse graining. Time dependent processes should also be validated with experimental evidence.

REFERENCES

ABAQUS, I. (2003). ABAQUS/Standard.

Adams, A. M., C. P. Buckley and D. P. Jones (2000). "Biaxial hot drawing of poly(ethylene terephthalate): Measurements and modelling of strain-stiffening." Polymer **41**(2): 771-786.

Aharoni, S. M. (1983). "On Entanglements of Flexible and Rodlike Polymers." Macromolecules **16**(11): 1722-1728.

Argon, A. S. (1973). "A theory for the low temperature plastic deformation of glassy polymers." Phil. Mag. **28**: 39.

Argon, A. S., V. V. Bulatov, P. H. Mott and U. W. Suter (1995). "Plastic deformation in glassy polymers by atomistic and mesoscopic simulations." J. Rheol. **39**(2): 377-399.

Arruda, E. M. and M. C. Boyce (1993a). "Strain rate and temperature dependence in amorphous polymers at finite strain." ASME MD **46**: 23-41.

Arruda, E. M. and M. C. Boyce (1993b). "A three-dimensional constitutive model for the large stretch behavior of rubber elastic materials." Journal of the Mechanics and Physics of Solids **41**(2): 389-412.

Avrami, M. (1941). "Granulation, Phase Change, and Microstructure Kinetics of Phase Change. III." The Journal of Chemical Physics **9**(2): 177-184.

Berendsen, H. J. C., J. P. M. Postma, W. F. van Gunsteren, A. DiNola and J. R. Haak (1984). "Molecular dynamics with coupling to an external bath." Journal of Chemical Physics **81**(8): 3684-90.

Bergstrom, J. S. and M. C. Boyce (2001). "Deformation of elastomeric networks: Relation between molecular level deformation and classical statistical mechanics models of rubber elasticity." Macromolecules **34**(3): 614-626.

Bergstrom, J. S., S. M. Kurtz, C. M. Rimnac and A. A. Edidin (2002). "Constitutive modeling of ultra-high molecular weight polyethylene under large-deformation and cyclic loading conditions." Biomaterials **23**(11): 2329-2343.

Bolton, K., S. B. M. Bosio, W. L. Hase, W. F. Schneider and K. C. Hass (1999). "Comparison of explicit and united atom models for alkane chains physisorbed on α-Al₂O₃ (0001)." Journal of Physical Chemistry B **103**(19): 3885-3895.

Boyce, M. C., S. Socrate and P. G. Llana (2000). "Constitutive model for the finite deformation stress-strain behavior of poly(ethylene terephthalate) above the glass transition." Polymer **41**(6): 2183-2201.

Buckley, C. P. and D. C. Jones (1995). "Glass-rubber constitutive model for amorphous polymers near the glass transition." Polymer **36**(17): 3301-3312.

Capaldi, F. M., M. C. Boyce and G. C. Rutledge (2004). "Molecular response of a glassy polymer to active deformation." Polymer **45**(4): 1391-1399.

Clauss, B. and D. R. Salem (1992). "Characterization of the non-crystalline phase of oriented poly(ethylene terephthalate) by chain-intrinsic fluorescence." Polymer **33**(15): 3193-3202.

Clauss, B. and D. R. Salem (1995). "A chain-intrinsic fluorescence study of orientation-strain behavior in uniaxially drawn poly(ehtylene terephthalate) film." Macromolecules **28**(24): 8328-8333.

Dooling, P. J., C. P. Buckley, S. Rostami and N. Zahlan (2002). "Hot-drawing of poly(methyl methacrylate) and simulation using a glass - Rubber constitutive model." Polymer **43**(8): 2451-2465.

Duan, X. M. and X. G. Gong (2003). "Local bias potential in hyper molecular dynamics method." Computational Materials Science **27**(3): 375-380.

Duering, E. R., K. Kremer and G. S. Grest (1994). "Structure and relaxation of end-linked polymer networks." Journal of Chemical Physics **101**(9): 8169.

Dupaix, R. B. and M. C. Boyce (2005). "Finite strain behavior of poly(ethylene terephthalate) (PET) and poly(ethylene terephthalate)-glycol (PETG)." Polymer **46**(13): 4827.

Everaers, R. (1999). "Entanglement effects in defect-free model polymer networks." New Journal of Physics **1**: 12.1-12.54.

Faulon, J.-L. (2001). "Stochastic generator of chemical structure. 4. Building polymeric systems with specified properties." Journal of Computational Chemistry **22**(6): 580-590.

Faulon, J. L., J. D. Hobbs, D. M. Ford and R. T. Wilcox (1997). "Massively Parallel Simulations of Diffusion in Dense Polymeric Structures." Proceedings of the IEEE/ACM SC97 Conference: 1-12.

Flory, P. J. (1974). "Foundations of Rotational Isomeric State Theory and General Methods for Generating Configurational Averages." Macromolecules **7**(3): 381-392.

Flory, P. J. and J. Rehner (1943). "Statistical mechanics of cross-linked polymer networks." The Journal of Chemical Physics **11**(11): 512-520.

Gagne, C. and M. Parizeau (2002). Open BEAGLE: A New Versatile C++ Framework for Evolutionary Computations. Late Breaking Papers, Genetic and Evolutionary Computing Conference (GECCO), New York, NY.

George, H. H. (1985). Spinline crystallization of polyethylene terephthalate. High-Speed Fiber Spinning. New York, Wiley**:** 271-294.

Glotzer, S. C. and W. Paul (2002). "Molecular and Mesoscale Simulation Methods for Polymer Materials." Annu. Rev. Mater. Res. **32**: 401-436.

Goddard III, W. A., C. Tahir, M. Blanco, N. Vaidehi, S. Dasgupta, W. Floriano, M. Belmares, J. Kua, G. Zamanakos, S. Kashihara, M. Iotov and G. Gao (2001). "Strategies for multiscale modeling and simulations of organic materials: Polymers and biopolymers." Computational and Theoretical Polymer Science **11**(5): 329-343.

Gong, X. G. and J. W. Wilkins (1999). "Hyper molecular dynamics with a local bias potential." Physical Review B: Condensed Matter **59**(1): 54-57.

Gregory, D. R. and M. T. Watson (1970). "Steady-state flow properties of poly(ethylene terephthalate) melts." J. Polymer Sci., Part C **30**: 399-406.

Grest, G. S., M. Putz, R. Everaers and K. Kremer (2000). "Stress-strain relation of entangled polymer networks." Journal of Non-Crystalline Solids **274**(1): 139-146.

Grimmelmann, E. K., J. C. Tully and E. Helfand (1981). "Molecular dynamics of infrequent events: thermal desorption of xenon from a platinum surface." Journal of Chemical Physics **74**(9): 5300.

Grubmuller, H. (1995). "Predicting slow structural transitions in macromolecular systems: conformational flooding." Physical Review E (Statistical Physics, Plasmas, Fluids, and Related Interdisciplinary Topics) **52**(3, pt.A): 2893.

Halley, J. W. and Y. Duan (2002). "Role of atomic level simulation in development of batteries." Journal of Power Sources **110**(2): 383-388.

Hansen, N. and A. Ostermeier (2001). "Completely derandomized self-adaptation in evolution strategies." Evolutionary Computation **9**(2): 159-95.

Hasan, O. A. and M. C. Boyce (1995). "Constitutive model for the nonlinear viscoelastic viscoplastic behavior of glassy polymers." Polymer Engineering and Science **35**(4): 331-344.

Henkelman, G. and H. Jonsson (1999). "A dimer method for finding saddle points on high dimensional potential surfaces using only first derivatives." Journal of Chemical Physics **111**(15): 7010-7022.

Henkelman, G. and H. Jonsson (2000). "Improved tangent estimate in the nudged elastic band method for finding minimum energy paths and saddle points." Journal of Chemical Physics **113**(22): 9978-9985.

Henkelman, G. and H. Jonsson (2001). "Long time scale kinetic Monte Carlo simulations without lattice approximation and predefined event table." Journal of Chemical Physics **115**(21): 9657-9666.

Hoffman, J. D. and J. I. Lauritzen (1961). "Crystallization of bulk polymers with chain folding: Theory of growth of lamellar spherulites." J. Res. Nat. Bur. Stand. A. Phys. Chem. **65A**(4): 297-336.

Hoover, W. G. (1985). "Canonical dynamics: equilibrium phase-space distributions." Physical Review A (General Physics) **31**(3): 1695-7.

Hukushima, K. and K. Nemoto (1996). "Exchange Monte Carlo method and application to spin glass simulations." Journal of the Physical Society of Japan **65**(6): 1604-8.

Humphrey, W., A. Dalke and K. Schulten (1996). "VMD: Visual molecular dynamics." Journal of Molecular Graphics **14**(1): 33.

James, H. M. and E. Guth (1943). "Theory of the elastic properties of rubber." The Journal of Chemical Physics **11**(10): 455-481.

Ko, M. J., N. Waheed, M. S. Lavine and G. C. Rutledge (2004). "Characterization of polyethylene crystallization from an oriented melt by molecular dynamics simulation." Journal of Chemical Physics **121**(6): 2823-32.

Kuhn, W. and F. Grun (1942). "Relationships between elastic constants and stretching double refraction of highly elastic substances." Kolloid Z. **101**: 248.

Lavine, M. S., N. Waheed and G. C. Rutledge (2003). "Molecular dynamics simulation of orientation and crystallization of polyethylene during uniaxial extension." Polymer **44**(5): 1771-1779.

Le Bourvellec, G., L. Monnerie and J. P. Jarry (1986). "Amorphous orientation and induced crystallization in uniaxially stretched poly(ethylene terephthalate glycol)." Polymer **27**(6): 856-860.

Leach, A. R. (2001). Molecular Modeling: Principles and Applications. Harlow, England, Pearson Education Limited.

Llana, P. G. and M. C. Boyce (1999). "Finite strain behavior of poly(ethylene terephthalate) above the glass transition temperature." Polymer **40**(24): 6729-6751.

Matthews, R. G., R. A. Duckett, I. M. Ward and D. P. Jones (1997). "The biaxial drawing behaviour of poly(ethylene terephthalate)." Polymer **38**(19): 4795-4802.

Mattice, W. L. and U. Suter (1935). Conformational Theory of Large Molecules: The Rotational Isomeric State Model in Macromolecular Systems. New York, J. Wiley.

McDowell, D. L. (2005). Internal state variable theory. Handbook of Materials Modeling, Part A: Methods. S. Yip and M. F. Horstemeyer. the Netherlands, Springer**:** 1151-1170.

McKechnie, J. I., D. Brown and J. H. R. Clarke (1992). "Methods of generating dense relaxed amorphous polymer samples for use in dynamic simulations." Macromolecules **25**(5): 1562-1567.

McKechnie, J. I., R. N. Haward, D. Brown and J. H. R. Clarke (1993). "Effects of chain configurational properties on the stress-strain behavior of glassy linear polymers." Macromolecules **26**(1): 198-202.

Melchionna, S., G. Ciccotti and B. L. Holian (1993). "Hoover NPT dynamics for systems varying in shape and size." Molecular Physics **78**(3): 533-44.

Meyer, P. (1999, 2000). "Lattice Geometries." from http://www.hermetic.ch/compsci/lattgeom.htm.

Meyer, P. (2000). Computational Studies of Pure and Dilute Spin Models. School of Mathematics and Computing, University of Derby.

Miron, R. A. and K. A. Fichthorn (2003). "Accelerated molecular dynamics with the bond-boost method." Journal of Chemical Physics **119**(12): 6210.

Miron, R. A. and K. A. Fichthorn (2004). "Multiple-time scale accelerated molecular dynamics: Addressing the small-barrier problem." Physical Review Letters **93**(12): 128301-1.

Nose, S. (1984). "A molecular dynamics method for simulations in the canonical ensemble." Molecular Physics **52**(2): 255-68.

Pal, S. and K. A. Fichthorn (1999). "Accelerated molecular dynamics of infrequent events." Chemical Engineering Journal **74**(1-2): 77.

Palys, L. H. and P. J. Phillips (1980). "Microkinetics of crystallization in poly(ehtylene terephthalate)." Journal of Polymer Science (Physics) **18**(4): 829-852.

Paul, W., D. Y. Yoon and G. D. Smith (1995). "Optimized united atom model for simulations of polymethylene melts." Journal of Chemical Physics **103**(4): 1702.

Pereda, J. J., N. Aravas and J. L. Bassani (1993). "Finite deformations of anisotropic polymers." Mechanics of Materials **15**(1): 3-20.

Plimpton, S. (1995). "Fast Parallel Algorithms for Short-Range Molecular Dynamics." Journal of Computational Physics **117**(1): 1-19.

Press, W. H., S. A. Teukolsky, W. T. Vetterling and B. P. Flannery (1996). Numerical Recipes in Fortran 77: The Art of Scientific Computing. Cambridge, Cambridge University Press.

Raha, S. and P. B. Bowden (1978). "Birefringence of Plastically Deformed Poly(Methyl Methacylate)." Polymer **13**: 174-183.

Rapaport, D. C. (2004). The Art of Molecular Dynamics Simulation. Cambridge, United Kingdom, Cambridge University Press.

Rigby, D. and R.-J. Roe (1987). "Molecular dynamics simulation of polymer liquid and glass. I. Glass transition." The Journal of Chemical Physics **87**(12): 7285-7292.

Rottach, D. R., J. G. Curro, G. S. Grest and A. P. Thompson (2004). "Effect of strain history on stress and permanent set in cross-linking networks: A molecular dynamics study." Macromolecules **37**(14): 5468-5473.

Salem, D. R. (1992a). "Crystallization kinetics during hot-drawing of poly(ethylene terephthalate) film: Strain-rate/draw-time superposition." Polymer **33**(15): 3189-3192.

Salem, D. R. (1992b). "Development of crystalline order during drawing of PET." Polymer **33**(15): 3182-3188.

Salem, D. R. (1998). "Microstructure development during constant-force drawing of poly(ethylene terephthalate) film." Polymer **39**(26): 7067-7077.

Sharaf, M. A., A. Kloczkowski and J. E. Mark (2001). "Monte Carlo simulations or reinforcement of an elastomer by oriented prolate particles." Computational and Theoretical Polymer Science **11**(4): 251-262.

Shepherd, J. E. (2002). An internal state variable based constitutive model for semi-crystalline polymers. Woodruff School of Mechanical Engineering. Atlanta, Georgia Institute of Technology**:** 115.

Shepherd, J. E., D. L. McDowell and K. I. Jacob (2006). "Modeling morphology evolution and mechanical behavior during thermo-mechanical processing of semi-crystalline polymers." Journal of the Mechanics and Physics of Solids **54**: 467-489.

Sok, R. M., H. J. C. Berendsen and W. F. van Gunsteren (1992). "Molecular dynamics simulation of the transport of small molecules across a polymer membrane." The Journal of Chemical Physics **96**(6): 4699-4704.

Sorensen, M. R. and A. F. Voter (2000). "Temperature-accelerated dynamics for simulation of infrequent events." Journal of Chemical Physics **112**(21): 9599-9606.

Steiner, M. M., P.-A. Genilloud and J. W. Wilkins (1998). "Simple bias potential for boosting molecular dynamics with the hyperdynamics scheme." Physical Review B: Condensed Matter **57**(17): 10-236.

Sweeney, J. and I. M. Ward (1996). "A constitutive law for large deformations of polymers at high temperatures." Journal of the Mechanics and Physics of Solids **44**(7): 1033-1049.

Swendsen, R. H. and J.-S. Wang (1986). "Replica Monte Carlo Simulation of Spin-Glasses." Physical Review Letters **57**(21): 2607-2609.

Tanaka, M., K. Iwata and N. Kuzuu (2000). "High-precision computer simulations of entangled polymer chains: 1. Determination of entanglement parameters of bond-fluctuation model." Computational and Theoretical Polymer Science **10**(3-4): 299-308.

Theodorou, D. N. (2004). "Understanding and predicting structure-property relations in polymeric materials through molecular simulations." Molecular Physics Foundations of Molecular Modeling and Simulation FOMMS 2003 **102**(2 PART I): 147-166.

Theodorou, D. N. and U. W. Suter (1985). "Detailed Molecular Structure of a Vinyl Polymer Glass." Macromolecules **18**(7): 1467-1478.

Tomita, Y. (2000). "Constitutive modelling of deformation behavior of glassy polymers and applications." International Journal of Mechanical Sciences AEPA'98: The Asia-Pacific Symposium on Advances in Engineering Plasticity and its Applications, Jun 21-Jun 25 1998 **42**(8): 1455-1469.

Turnbull, D. and J. C. Fisher (1949). "Rate of nucleation in condensed systems." J. Chem. Phys. **17**(1): 71-73.

Uhlherr, A. and D. N. Theodorou (1998). "Hierarchical simulation approach to structure and dynamics of polymers." Current Opinion in Solid State and Materials Science **3**(6): 544-551.

van der Vegt, N. F. A., W. J. Briels, M. Wessling and H. Strathmann (1996). "Free energy calculations of small molecules in dense amorphous polymers. Effect of the initial guess configuration in molecular dynamics studies." Journal of Chemical Physics **105**(19): 8849.

Voter, A. F. (1997a). "Hyperdynamics: accelerated molecular dynamics of infrequent events." Physical Review Letters **78**(20): 3908-3911.

Voter, A. F. (1997b). "Method for accelerating the molecular dynamics simulation of infrequent events." Journal of Chemical Physics **106**(11): 4665.

Voter, A. F. (1998). "Parallel replica method for dynamics of infrequent events." Physical Review B: Condensed Matter **57**(22): R13986-57.

Voter, A. F., F. Montalenti and T. C. Germann (2002). "Extending the Time Scale in Atomistic Simulation of Materials." Annu. Rev. Mater. Res. **32**: 321-46.

Wang, J.-C., S. Pal and K. A. Fichthorn (2001). "Accelerated molecular dynamics of rare events using the local boost method." Physical Review B: Condensed Matter **63**: 085403-1:9.

Wang, M. C. and E. Guth (1952). "Statistical Theory of Networks of Non-Gaussian Flexible Chains." The Journal of Chemical Physics **20**(7): 1144-1157.

Wu, P. D. and E. van der Giessen (1993). "On improved network models for rubber elasticity and their applications to orientation hardening in glassy polymers." Journal of the Mechanics and Physics of Solids **41**(3): 427-456.

Yashiro, K., T. Ito and Y. Tomita (2003). "Molecular dynamics simulation of deformation behavior in amorphous polymer: Nucleation of chain entanglements and network structure under uniaxial tension." International Journal of Mechanical Sciences **45**(11): 1863-1876.

Ziabicki, A. (1988). "Mechanisms of 'neck-like' deformation in high-speed melt spinning. 2. Effects of polymer crystallization." Journal of Non-Newtonian Fluid Mechanics **30**(2-3): 157-168.

Ziabicki, A. and L. Jarecki (1985). The theory of molecular orientation and oriented crystalization in high-speed spinning. High-Speed Fiber Spinning. New York, Wiley**:** 225-269.